TROPICAL SEA SURFACE TEMPERATURE VARIABILITY AND ITS ROLE ON ARCTIC ATMOSPHERIC CIRCULATION AND SEA ICE

by

LORI J. WACHOWICZ

(Under the Direction of Thomas Mote)

ABSTRACT

The Arctic has undergone significant warming and rapid sea ice loss due to a series of positive feedbacks known as Arctic amplification. Climate forcing from the tropics contributes to Arctic amplification through multiple pathways, including the radiative and turbulent heat transfers during enhanced moisture transport. Moisture transport from anticyclonic circulation anomalies embedded within Rossby waves plays a substantial role in modulating seasonal sea ice, where this moisture is enhanced during Rossby wave breaking. Poleward moisture transport is projected to increase through the end of the century, concurrent with longitudinal shifts in tropical sea surface temperature (SST) anomalies, leads to uncertainty around long-term tropical contributions to Arctic amplification.

This dissertation ascertains the connections of tropical SSTs variability, atmospheric circulation-forced moisture fluxes, and Arctic sea ice by evaluating those relationships within global climate models (GCMs). First, to understand the linkages between tropical SST variability and Arctic atmospheric circulation, a novel potential vorticity-based approach is used to identify Rossby wave break-related blocking events, which are composited to quantify tropical variability impacts on moisture transport. Findings establish that summertime moisture transport in the

North Atlantic (NA) during cyclonic wave breaking is greatest when El Niño originates in the Central Pacific (CP). Second, fully coupled GCM large ensemble simulations are utilized to explore the connection between the ENSO variability and sea ice. Although observations confirm a negative correlation between summertime sea ice and CP ENSO in the Canadian Archipelago region, the large ensemble simulations do not adequately capture the extent of this correlation. The CP ENSO teleconnection as demonstrated through 500 hPa geopotential height and moisture anomalies appears to have limited representation in the model. Finally, using the large ensemble simulations, atmospheric blocking events are identified to assess blocking impacts on past and projected sea ice concentration. A novel finding here shows significant increases in the number of projected summer blocking days in the NA, which appears driven by blocking persistence. NA blocking activity leads to substantial spring and summer sea ice loss through increased surface turbulent heat anomalies, where projected increases in blocking may exacerbate sea ice loss through the end of the century.

INDEX WORDS: Arctic Sea Ice, Moisture Transport, ENSO, Blocking, Rossby Wave Breaking, Climate Models

TROPICAL SEA SURFACE TEMPERATURE VARIABILITY AND ITS ROLE ON ARCTIC ATMOSPHERIC CIRCULATION AND SEA ICE

by

LORI J. WACHOWICZ

B.S., Michigan State University, 2015

M.S., University of Georgia, 2017

A Dissertation Submitted to the Graduate Faculty of The University of Georgia in Partial Fulfillment of the Requirements for the Degree

DOCTOR OF PHILOSOPHY

ATHENS, GEORGIA

2022

TROPICAL SEA SURFACE TEMPERATURE VARIABILITY AND ITS ROLE ON ARCTIC ATMOSPHERIC CIRCULATION AND SEA ICE

by

LORI J. WACHOWICZ

Major Professor:	Thomas Mote
Committee:	Gabriel Kooperman
	J. Marshall Shepherd
	John Knox
	Gina Henderson

Electronic Version Approved:

Ron Walcott
Vice Provost for Graduate Education and Dean of the Graduate School
The University of Georgia
August 2022

ACKNOWLEDGMENTS

This entire dissertation involved the tremendous support of various agencies and persons, who collectively made this research happen. First, this work was partially funded by Strategic Environmental Research and Development Program (SERDP) project number RC18-1658 and NSF Arctic Systems Science award number 1900324. Part of this work was conducted during a visit to the National Center of Atmospheric Research during a Graduate Visitor Fellowship. As such, this material is also based upon work supported by the National Center for Atmospheric Research, which is a major facility sponsored by the National Science Foundation under Cooperative Agreement No. 1755088. Any opinions, findings and conclusions or recommendations expressed in this material do not necessarily reflect the views of the National Science Foundation.

Perhaps most importantly, the mentorship and guidance from my major professor, Thomas Mote, helped make not only my doctoral experience, but my entire graduate school experience, enjoyable. In addition to him challenging me to become a better researcher and scholar throughout the process, his leadership both inside and outside of the lab group has always inspired me to pursue interests and experiences outside of my research to develop me into the person I am today. I strive to be even just a fraction of the role model and mentor that he is to young professionals.

I am incredibly grateful to my doctoral committee, Professors John Knox, Gabe Kooperman, Marshall Shepherd at UGA and Professor Gina Henderson at the US Naval

Academy. I have learned so much from the classes I have taken at UGA from these scholars and through my collaborations with them, many lasting my entire graduate school experience. Their support, ideas, and enthusiasm throughout my doctoral research have been invaluable.

Various members of the UGA Geography community—faculty, staff, and students—have helped shaped my doctoral experience by motivating me when I needed it most. I am appreciative of our past and present Climate Lab cohort, who have provided much needed scientific discussions and inspiration as well as the greatest socializing outlet where needed. These individuals who I am most indebted to include (but is most certainly not limited to) Flavia Moraes, Kyle Mattingly, Jonathon Preece, and Haylie Mikulak, as well as the various others who I have had the greatest pleasure of working with at various points over the years.

Additionally, I am appreciative of Marika Holland at the National Center of Atmospheric Research, who oversaw and provided excellent feedback on my research, taught me about sea ice, and made my virtual visit to NCAR as welcoming as possible during a global pandemic.

All of this hard work required "behind the scenes" support from several individuals: my parents, Mary and Jayme, whose emotional support is unprecedented and unconditional; my wonderful pets, Radar and Newt, for the occasional comedic relief and the fluffy snuggles; my incredible friends outside of academia who grounded me at times when graduate school was too much; and Paul, who joined the party late in the game but has since provided all of the #insPaulration needed to finish my doctorate research.

TABLE OF CONTENTS

Page

LIST OF TABLES

Page

LIST OF FIGURES

Page

CHAPTER 1

INTRODUCTION AND LITERATURE REVIEW

1.1 Introduction

The Arctic cryosphere is a dynamic environment, closely coupled to both atmospheric and oceanic processes, and declining sea ice and snow cover has contributed to rapid warming during recent decades through a process known as Arctic amplification (e.g., Serreze and Francis, 2006; Cohen et al., 2014). This unprecedented warming has, in turn, contributed to losses in Arctic snow cover, increased runoff from the Greenland ice sheet, and rapid loss of sea ice (Arctic Report Card 2021). Furthermore, the melting of the Arctic cryosphere has environmental and socioeconomic implications, both locally and globally. For example, the melting of snow cover results in increases in runoff while melting of the permafrost releases additional methane into the climate system (Arctic Report Card 2021). Recently the Greenland ice sheet is the most significant contributor to global mean sea level rise since 2003, with an estimated contribution of 20% to sea level rise at the rate of 0.60 ± 0.04 mm yr^{-1} (Horwath et al., 2022). An ice-free Arctic further has socioeconomic implications – including increased shipping activity, changes in accessibility to renewable resources, and infrastructure failures— in which proper governance of this region requires sufficiently better forecasts and support for ensuring proper adaptation and mitigation for Arctic communities (Meredith et al., 2019).

Changes in Arctic sea ice strongly modulate the Arctic climate (Figure 1.1a). Sea ice extent usually reaches a maximum around March (Figure 1.1b) and is at a minimum in September (Figure 1.1c). Arctic sea ice has declined over the last few decades (Peng and Meier,

2018; Stroeve and Notz, 2018) with extreme variability in Arctic sea ice cover becoming more frequent (Mioduszewski et al., 2019; Holland et al., 2019; Landrum and Holland, 2020). This rate of decreasing sea ice extent is most prominent in summer with nearly a 10-15% decrease compared to the 1981-2010 average (Arctic Report Card 2021 and Figure 1.2). This sea ice loss includes significant thinning (Lindsay and Schweiger, 2015) and loss of multi-year ice (Stroeve and Notz, 2018).

As a result, the Arctic Ocean is projected to become "ice free" in summer by 2040 (DeRepentigny et al., 2020) partly due to a positive feedback within the Arctic climate system known as Arctic amplification (Serreze and Francis, 2006; Dai et al., 2019; Feldl et al., 2020). Recent losses in summer sea ice allow open water to absorb more incoming solar radiation, increasing ocean temperatures and retarding winter sea ice growth through latent heat release, thus enhancing regional warming (Inoue and Hori, 2011; Stroeve and Notz, 2018). At its core, Arctic amplification argues that the positive feedback from sea ice loss, such as that described above, increase air temperature, where the reduction in the meridional temperature gradient allows for higher geopotential heights and weaker westerly winds, causing an "wavier" jet stream and slower-moving eastward propagation of weather (e.g., Cohen et al., 2014; Vavrus et al., 2017). Together, these changes in the Arctic cryosphere further provide a physical basis for influencing the polar vortex and affecting mid-to-upper latitude weather and climate (Cohen et al., 2014; Sun et al., 2015; Vavrus et al., 2017; Screen et al., 2018; Kim and Kim, 2020; Cohen et al., 2020).

The feedback between sea ice and the atmosphere are a *response to* and also are a *driver of* Arctic amplification (Cohen et al., 2014). In addition to internal feedbacks between the cryosphere, ocean, and atmosphere, recent research posits an effect of tropical sea surface

temperatures on the poleward transfer of sensible and latent heat, thus affecting Arctic climate. A decline in September sea ice is thought to be attributed to a stronger anticyclonic circulation over Greenland and its associated increases in warmer, moister conditions in the Arctic after having originated in the tropical Pacific (Ding et al., 2014; Ding et al., 2017). Additionally, strong stationary anticyclonic circulation anomalies known as "blocking" over Greenland increase sea ice export out of the Greenland Sea, leading to sea ice decline in September (Kwok, 2009; Smedsrud et al., 2016) and are connected to anomalous surface melt over the Greenland ice sheet (e.g., Preece et al., 2022). Furthermore, continued Arctic amplification from sea ice decline in the Baffin Bay, Davis Strait, and Labrador Sea regions may result in increased west-moving Greenland blocking events due to a decrease in the westerlies (Chen and Luo, 2017) and associated potential vorticity gradient (Luo et al., 2018; Luo et al., 2019). Yet, sea ice-atmosphere feedbacks are not well simulated in climate models (Liptak and Strong, 2016; Ding et al., 2017; Mioduszewski et al., 2019; Dai et al., 2019), motivating the need to examine and evaluate tropical contributions to sea ice loss as it pertains to Arctic amplification.

1.2 Literature Review

1.2.1 Tropical Drivers of Arctic Atmospheric Circulation

Rossby wave activity in the Arctic has recently been shown to be influenced by the location of enhanced tropical sea surface temperatures (SSTs) in both the Pacific and Atlantic Oceans (Matsumura and Kosaka, 2019; Matsumura et al., 2021). Linkages between tropical SSTs and extratropical atmospheric circulation exist through the propagation of atmospheric Rossby waves, particularly originating from convection in the tropical Pacific and Indian Oceans (Hoskins and Woollings, 2015; Ding et al., 2017). Rossby wave trains originating in the tropics

can be associated with warming in the high latitude troposphere, particularly over Greenland, and enhances the North Atlantic Oscillation (NAO) negative phase (Ding et al., 2014; Lim et al., 2019). This tropical-to-Arctic teleconnection leads to Greenland blocking conditions (Hanna et al., 2015), and further shows strong connections to sea ice variability (Hu et al., 2016; Topál et al., 2020; Matsummura et al., 2021). More importantly, the breaking of these Rossby waves enhances heat and moisture flux toward the poles (Liu and Barnes, 2015), where the enhanced energy and moisture fluxes have profound impacts on Arctic sea ice (Woods and Caballero, 2016; Yang and Magnusdottir, 2017) and the Greenland ice sheet (Mattingly et al., 2018; Preece et al., 2022).

The El Niño-Southern Oscillation (ENSO) serves as the pacemaker of global climate, given its innate mid- and high latitude teleconnections (Trenberth, 1997; Capotondi et al., 2015; Yuan et al., 2018; Capotondi et al., 2020a). The variability in the location of SST anomalies in the Pacific Ocean during ENSO can alter surface air temperatures and moisture fluxes in the North Atlantic (Li et al., 2019). Significant warming and increased atmospheric moisture over Greenland coincide with a phenomenon known as “Modoki” El Niño, also known as a Central Pacific (CP) El Niño, which is associated with positive SST anomalies originating in the central Pacific (Ashok et al., 2007; Li et al., 2019; Lim et al., 2019).

Matsumura and Kosaka (2019) show that tropical Pacific SST anomalies following both El Niño and La Niña phases induce Rossby wave trains, which aid in vastly different regional Arctic responses in sea ice. Further evidence suggests that CP El Niño events may cool portions of the Arctic during summer, particularly near the North Atlantic, thus promoting sustained regional sea ice cover (Hu et al., 2016; Matsumura et al., 2021). Positive temperature anomalies over Greenland are most noticeable during CP El Niño compared to eastern “canonical” Pacific

(EP) El Niño teleconnected to 500 hPa anomalies over the North Atlantic (Feng et al., 2017; Li et al., 2019) (Figures 1.3, 1.4). Most interestingly, there have been observed and projected increases in CP El Niño intensity and frequency (Yeh et al., 2009; Lee and McPhaden, 2010; Cai et al., 2014), which coincide with increased warming in the Arctic and lead to considerable implications surrounding projected poleward energy transfer and climate impacts.

Within Rossby waves originating from the tropics, energy is propagated into the mid- and high latitudes (Wirth et al., 2018), where this energy transfer commonly occurs during the "wave breaking" process (Bowley et al., 2019a). A Rossby wave will break when the phase speed of the wave becomes slower, and the amplitude of the wave to increase until the phase speed is equivalent to the background flow (e.g., Wirth et al., 2018; Riboldi et al., 2020). This process is easily identified by overturning of isentropes (contours of potential temperature) on a constant potential vorticity surface (e.g., Liu and Barnes, 2015). This Rossby wave breaking (RWB) process results in a substantial transfer of energy through diabatic heating from moisture transport which can further play a pivotal role in rapidly enhancing upper-level ridges over the North Atlantic (Pfahl et al., 2015; Zhang and Wang, 2018; Steinfeld and Pfahl, 2019).

Wave breaking can be identified by the direction of the overturning of the wave in either a cyclonic or anticyclonic manner, to indicate either cyclonic wave breaking (CWB) or anticyclonic wave breaking (AWB), where the RWB direction has implications for regional weather (Michel and Rivière, 2011; Masato et al., 2012; Masato et al., 2013a). Increases in AWB activity produce more potential energy build up during the Northern Hemisphere winter, allowing for a poleward shift in the jet stream, which may be caused by moisture transport during the wave breaking (Bowley et al., 2019b). Swenson and Straus (2017) show that transient heat fluxes associated with AWB oppose a strengthening jet, which can act to either dampen or

push a ridge downstream and act to enhance existing Scandinavian blocking. In the North Pacific, AWB frequency decreases under El Niño conditions, where the decrease in frequency is greater under EP El Niño when compared to CP El Niño (Liu et al., 2014).

On the other hand, wintertime CWB in the North Atlantic may help weaken the jet stream due to transient heat fluxes at lower levels that reduce the vertical wind shear (Swenson and Straus, 2017). CWB frequency may be enhanced during negative NAO conditions, while AWB events may become more frequent during positive NAO, which corresponds to ridge strengthening over the Atlantic and blocking over Scandinavia (Swenson and Straus, 2017). Enhanced CWB activity likewise corresponds to increased anticyclonic circulation anomalies over Greenland (Michel et al., 2021; Drouard et al., 2021). Significant Greenland melt events have been observed and connected with blocking events associated with CWB in July 2012 and 2019 (Figure 1.5), due to the frequent coincidence of CWB with high moisture transport over Greenland (Liu and Barnes, 2015; Mattingly et al., 2016). El Niño conditions further act to increase CWB frequency in the North Pacific, where this frequency shifts somewhat eastward under CP El Niño conditions when compared to EP El Niño conditions (Liu et al., 2014), indicating that variability in ENSO itself can influence RWB climatology, though limited work has considered these connections in the North Atlantic, specifically. A more comprehensive climatology of ENSO diversity and its influences on high latitude atmospheric circulation is therefore pertinent to understand both seasonal and regional impacts on sea ice going forward.

1.2.2 Arctic Blocking-Sea Ice Interactions

Anticyclones play a pivotal role in the Arctic climate system by advecting warm, moist air along the periphery of the anticyclone or through increased subsidence within the anticyclone,

which alters the surface energy budget thus leading to sea ice decline (Woods et al., 2013; Woods and Caballero, 2016; Kim and Kim, 2017; Yang and Magnusdottir, 2017; You et al., 2022). Most Arctic anticyclones are formed through moist injections by lower latitude cyclones, which may be driven by tropical teleconnections (Ding et al., 2014; Woods et al., 2017). Warmer, humid air masses, when injected into the Arctic, will result in isentropic upglide, which contributes to low-level cloud formation, and latent heat release through condensation, which allows a parcel of air to continue to rise isentropically (Pfahl et al., 2015; Komatsu et al., 2018; Steinfeld and Pfahl, 2019). Diabatic airstreams associated with these Rossby waves then promote the strong ascent and latent heating needed to amplify ridges and form anticyclones, especially when in combination with strong negative potential vorticity anomalies aloft (Wernli and Papritz, 2018). The amplification of these ridges can enforce persistent blocking, especially under anomalous sea ice conditions, due to the displacement of the jet stream (Tachibana et al., 2019).

Once an Arctic anticyclone forms, environmental conditions change due to an increase in incoming shortwave radiative fluxes, where reduced cloudiness and adiabatic warming contribute to melting of the sea ice, particularly in the summer (Wernli and Papritz, 2018). For example, Arctic blocking patterns may increase surface temperatures under clear sky conditions by more than 5K in spring and as much as 2K in summer (Johansson et al., 2017). Persistent anticyclonic conditions during summer in the Arctic act to both enhance downwelling shortwave radiation through increased subsidence, which preconditions the sea ice for melting, while increased winds along the periphery of the anticyclone can act to transport ice in and out of a region (Kay et al., 2008; Zhang et al., 2008; Kapsch et al., 2013; Kapsch et al,. 2016; Wernli and Papritz, 2018; You et al., 2022). Strong high latitude blocking events occurred in summers of

2007 and 2012, for instance, and contributed to significantly low September sea ice concentration. In 2007, areas with the strongest below-normal sea ice cover coincided with a strong Omega blocking pattern in the North Pacific in August and September which drove sea ice loss in the Beaufort, Chukchi, and East Siberian seas primarily through increased surface radiative and wind anomalies (Kay et al., 2008; Zhang et al., 2008) (Figure 1.6a). Additionally, moisture transport along the warm conveyor belt located to the west of the anticyclone may act to enhance downwelling longwave radiation and latent heating over the sea ice and further contribute directly to summer melting (Kapsch et al., 2016; Wernli and Papritz, 2018; Komatsu et al., 2018) (Figure 1.6b).

Winter blocking episodes play a substantial role in driving sea ice loss through their interactions with cyclones and enhance planetary scale latent heat transport (Papritz and Dunn-Siguoin, 2020; Rydsaa et al., 2021; Murto et al., 2022). During the winter, several days with anomalous meridional moisture transport and high skin temperatures coincided with record low sea ice growth recently during the 2016–17 season (Hegyi and Taylor, 2018) (Figure 1.7). Moist intrusions can affect an area for 3–4 days prior to arrival, where warming will occur quickly near the surface and a reduction in the inversion strength becomes present thus promoting "bottom-amplified warming" in a warming Arctic (Woods and Caballero, 2016; Johansson et al., 2017). Spring negative water vapor anomalies and clear sky conditions associated with anticyclones result in late melt onset and below normal air temperatures, which occur about a month prior to melt onset (Kapsch et al., 2013; Woods and Caballero, 2016). Unsurprisingly, earlier melt onset is characterized by an increase of moisture transport convergence due to stronger circulation anomalies before and at onset (Mortin et al., 2016) and further precondition the sea ice ahead of the summer melting season (Yang and Magnusdottir, 2018).

Given projections of enhanced moisture transport into the Arctic (Lavers et al., 2015; Payne et al., 2020) and the impact of blocking-related moisture intrusions on sea ice to vary seasonally (Henderson et al., 2021 and references therein), increased effort is required to ensure the complexities of sea ice loss is represented in model simulations. Understanding future blocking impacts on sea ice therefore requires realistic representation of physical feedbacks between the atmosphere and sea ice in climate models, such as those feedbacks with cloud (e.g., Morrison et al., 2019), albedo (e.g., Thackeray and Hall, 2019), and temperature (e.g., Liptak and Strong, 2016), among others. Furthermore, a climatological assessment of observed and modeled blocking impacts on sea ice requires seasonal consideration, given the multitude of physical drivers of sea ice at play, as different studies have focused only on a single season (e.g., Yang and Magnusdottir, 2018; Topál et al., 2020).

1.2.3 Understanding Blocking in Climate Models

The role of Arctic amplification on blocking activity remains a substantial topic of interest, with several proposed mechanisms explaining observed and projected changes in seasonal blocking (Cohen et al., 2014; Coumou et al., 2018; Cohen et al., 2020). A prominent hypothesis posits that weakening of the zonal winds will produce a wavier, high-amplitude jet stream that will lead to slow Rossby wave propagation and more blocking (Francis and Vavrus, 2015; Vavrus et al., 2017). Another hypothesis suggests that, as the jet stream migrates poleward, the compression of Rossby waves may result in higher amplitudes and thus lead to more blocking (Wang and Kuang, 2019). A countering hypothesis instead suggests that blocking activity is (and will remain) a product of eddy-driven feedbacks from Rossby wave breaking, which alter the speed and position of the eddy-driven jet (Ronalds et al., 2018; Woollings et al.

2018a; Hwang et al., 2020). Given the competing hypotheses to explain how blocking will change in the future, it is then of utmost importance to have a thorough understanding of blocking representation in global climate models (GCMs).

The underestimation of blocking events in GCMs has been well documented throughout the climate model era (D'Andrea et al., 1998; Masato et al., 2013b; Davini and D'Andrea, 2020). In particular, GCMs used in Coupled Model Intercomparison Project versions 3 through 6 (CMIP3 and CMIP6, respectively) underestimate blocking, particularly over Greenland (Belleflamme et al., 2013; Davini and D'Andrea, 2016; Woods et al., 2017; Hanna et al., 2018a; Davini and D'Andrea, 2020; Schiemann et al., 2020). This underestimation is crucial to resolve given observed positive trends in summer blocking, especially near Greenland (Figure 1.8) (Peings et al., 2017; Hanna et al., 2018a; Wachowicz et al., 2021) and the seasonal impact that blocking has on increased poleward moisture and energy transport (Barrett et al., 2020; You et al., 2022) and impacts on the North Atlantic ice (Belleflamme et al., 2015; Stroeve et al., 2017; Preece et al., 2022). Projections of blocking suggest a decrease in winter blocking in this region (Dunn-Sigouin and Son, 2013; Peings et al., 2017; Woollings et al., 2018b), with little attention given both to other seasons and potential impacts.

Differences in blocking climatologies both in observations and in various GCMs may be partially attributed to the choice of blocking index used (Barnes et al., 2012; Woollings et al., 2018b; Wachowicz et al., 2020; Schiemann et al., 2020). However, other factors associated with individual models such as model resolution (Bauer et al., 2008; Schiemann et al., 2017), parameterization (Woollings et al., 2018b), and representation of the mean climatological state of the model (Scaife et al., 2010; Woollings et al., 2018b) may play a role in explaining why blocking is difficult to accurately represent within climate models. In particular, the biases in

mean flow, which are related to how the jet stream is represented within the climate models, is proposed to contribute to differences in blocking frequency (Scaife et al., 2010; Woollings et al., 2018a). The improvement of cyclone tracks and mean flow within CMIP5 models may be attributed to higher resolution within the models themselves (Zappa et al., 2013). The inability of CMIP GCMs to reproduce anticyclonic circulation over Greenland may be driven by biases in atmospheric temperature or induce dynamic biases within the mean climate state of 500 hPa heights itself (Belleflamme et al., 2013). Kay et al. (2015) demonstrate that the Community Earth Systems Model (CESM) large ensemble (LENS) project has an improved, yet realistic, blocking climatology when using a 1-dimensional blocking metric and suggest that model physics plays a role in differences in climatological-mean state and related variability in blocking. The updated version of CESM LENS (CESMv2 LENS) further improves upon CESM LENS in terms of its capability to accurately produce blocking patterns compared to other CMIP6 models (Simpson et al., 2020), though the CESMv2 LENS simulations were not publicly available at the time of this publication. Moreover, while there has been attention paid to blocking, its atmospheric conditions, and its representation within CESM LENS, and GCMs more broadly, there has been little focus on connecting high-latitude blocking back to historical and projected sea ice variability.

1.3 Research Objectives

Amid ongoing debate over Arctic amplification, its drivers, and its influence on regional weather and climate, this dissertation seeks to connect internal tropical variability to sea ice loss though understanding its effect on Arctic atmospheric circulation patterns, such as blocking. Moreover, the findings represent an initial attempt to identify the causal mechanisms and their

representation in a global climate model (GCM). This research is further organized into the following three key objectives.

1. *Tropical sea surface temperature (SST) variability and its connection to high-latitude atmospheric circulation and moisture transport:* What are the spatiotemporal characteristics of high-latitude blocking as it relates to Rossby wave breaking (RWB)? How do these characteristics change as a result of tropical Pacific SST variability, such as the El Niño-Southern Oscillation (ENSO)? What is the implication of tropical Pacific SST variability (i.e., ENSO) on high-latitude moisture transport as a result of RWB?
2. *Tropical SST variability and its impact on Arctic sea ice:* How does ENSO impact Arctic sea ice? How might ENSO's effect on specifically Arctic moisture transport play a role in sea ice variability? How well are these relationships exhibited within a GCM large ensemble?
3. *High-latitude blocking and its connection to Arctic sea ice:* How is high-latitude blocking expected to change by the end of the 21st Century? What is the expected impact of blocking on sea ice regarding sea ice concentration and surface energy fluxes? How might these impacts change under future climate projections?

Each research objective is contained within an individual chapter, which comprises a manuscript intended for publication in a scholarly journal. The results from the first objective are presented in Chapter 2, which is intended for submission to the journal *Climate Dynamics*. Results from the second objective form Chapter 3 and are to be submitted to the *Journal of Climate*. Lastly, Chapter 4 details the third objective, and is to be submitted to *Journal of Geophysical Research: Atmospheres*. A summary of all three manuscripts is included in Chapter 5.

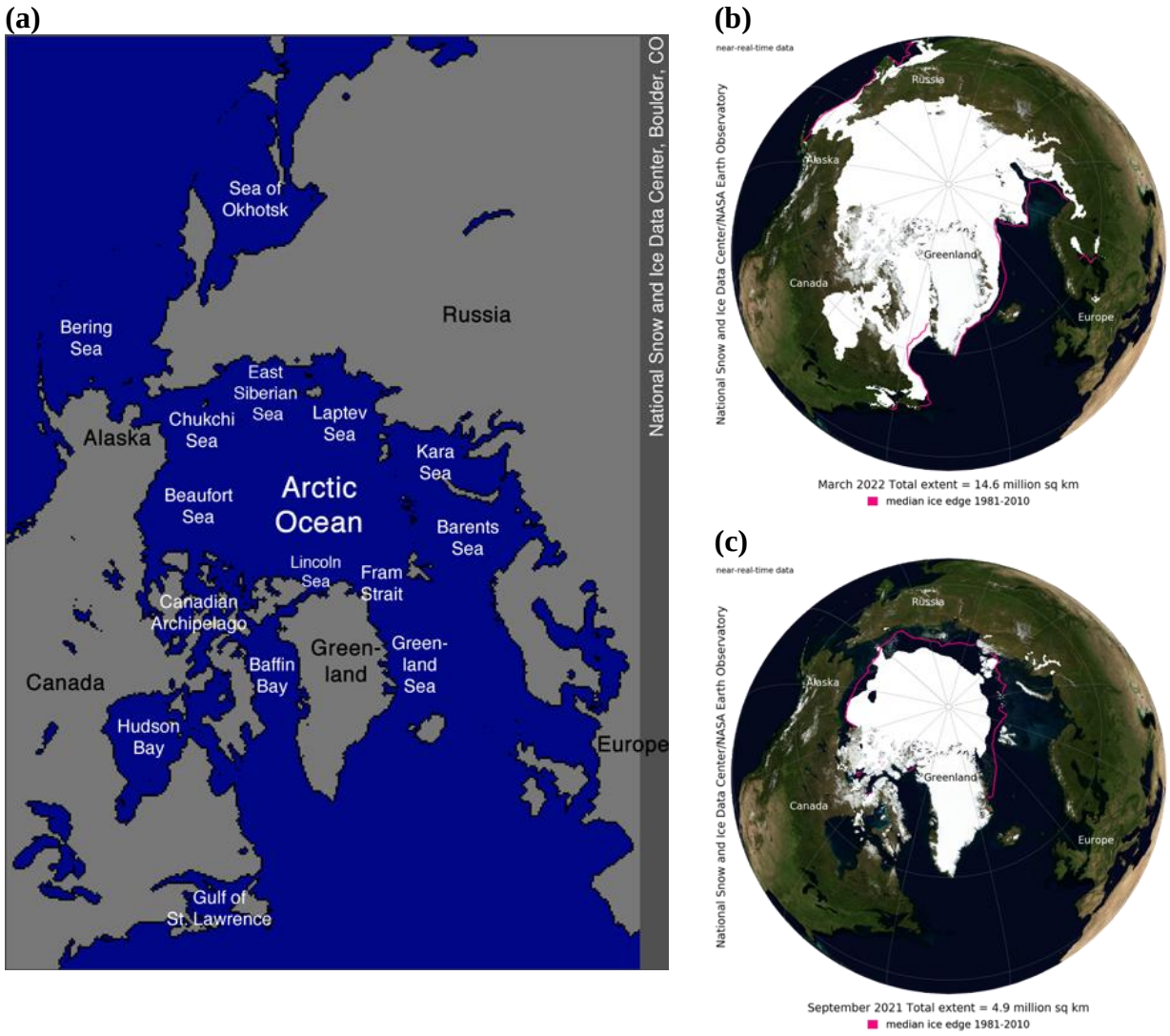

Figure 1.1. Map of the Arctic (a) with observed sea ice extent for March 2022 (b) and September 2021 (c). Median sea ice extent for both March and September from 1981–2010 is denoted by the pink line. Figures available from National Snow and Ice Data Center (https://nsidc.org/data/seaice_index/archives).

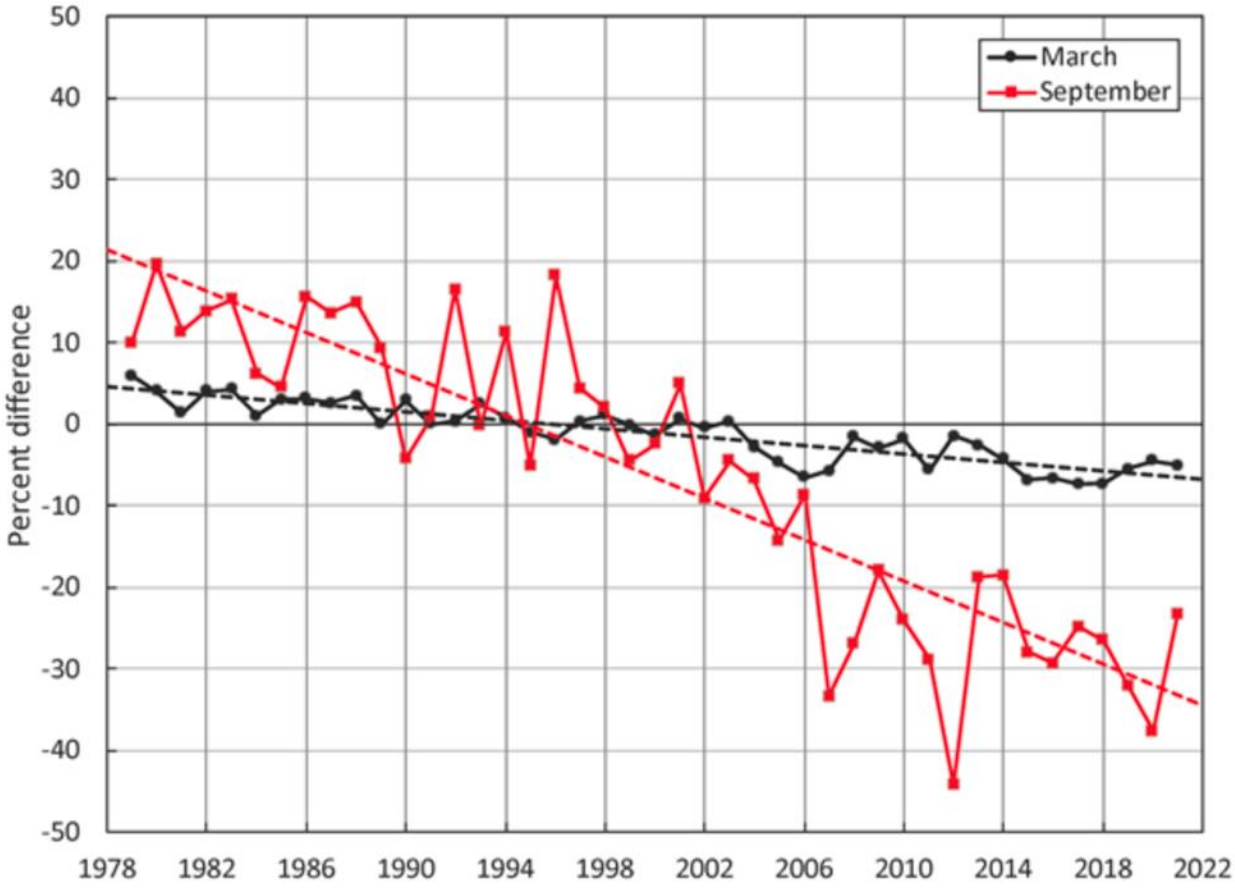

Figure 1.2. March (black) and September (red) sea ice extent anomalies (solid lines) and linear trend lines (dashed) for the period 1979-2021with respect to the 1981-2010 average for each month. Figure from Arctic Report Card 2021.

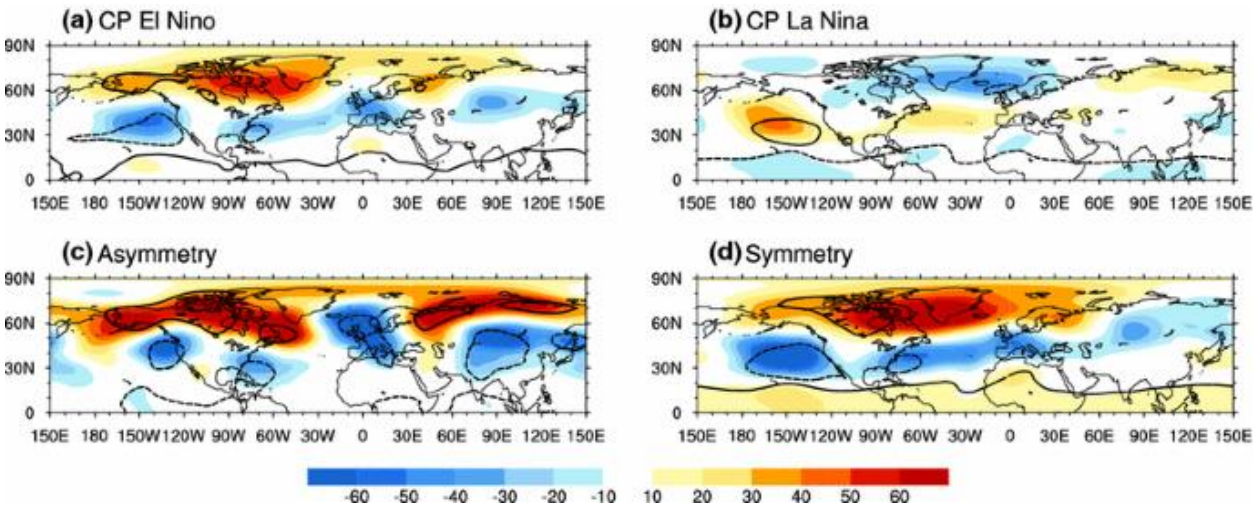

Figure 1.3. Composite DJF mean 500 hPa geopotential height anomalies (shading, gpm) for the (a) CP El Niño (left column) and (b) CP La Niña (right column), respectively. (c) The asymmetric component is estimated by the summation of (a) and (b). (d) The symmetric component is estimated as the difference of (a) and (b). Contours denote 95% confidence levels based on the two-tailed Student's t test. Figure used with permission from Feng et al. (2017).

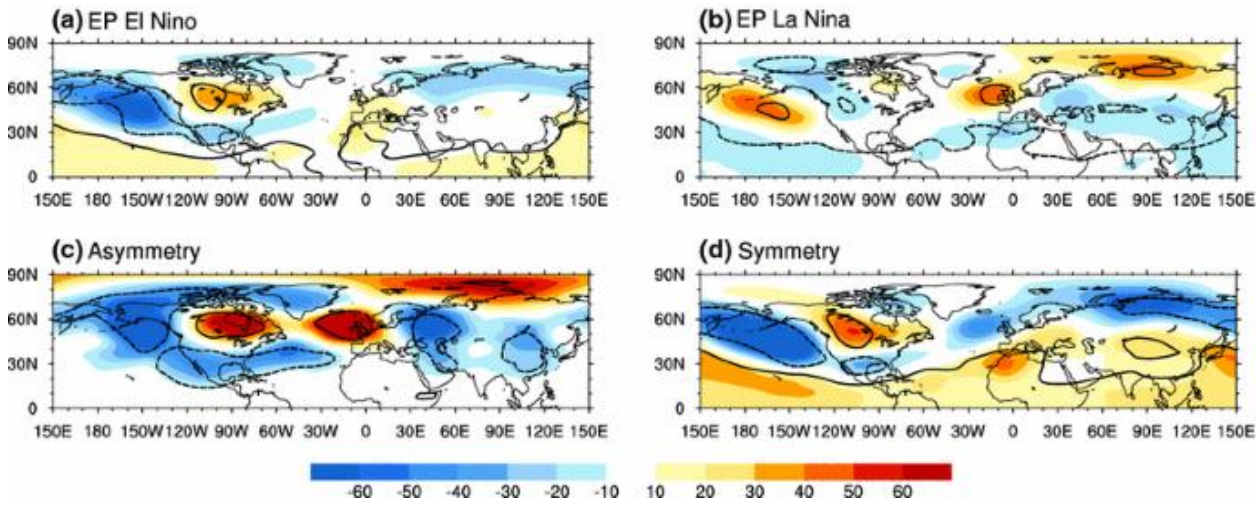

Figure 1.4. Same as Figure 1.3, but for the EP El Niño and EP La Niña cases. Figure used with permission from Feng et al. (2017).

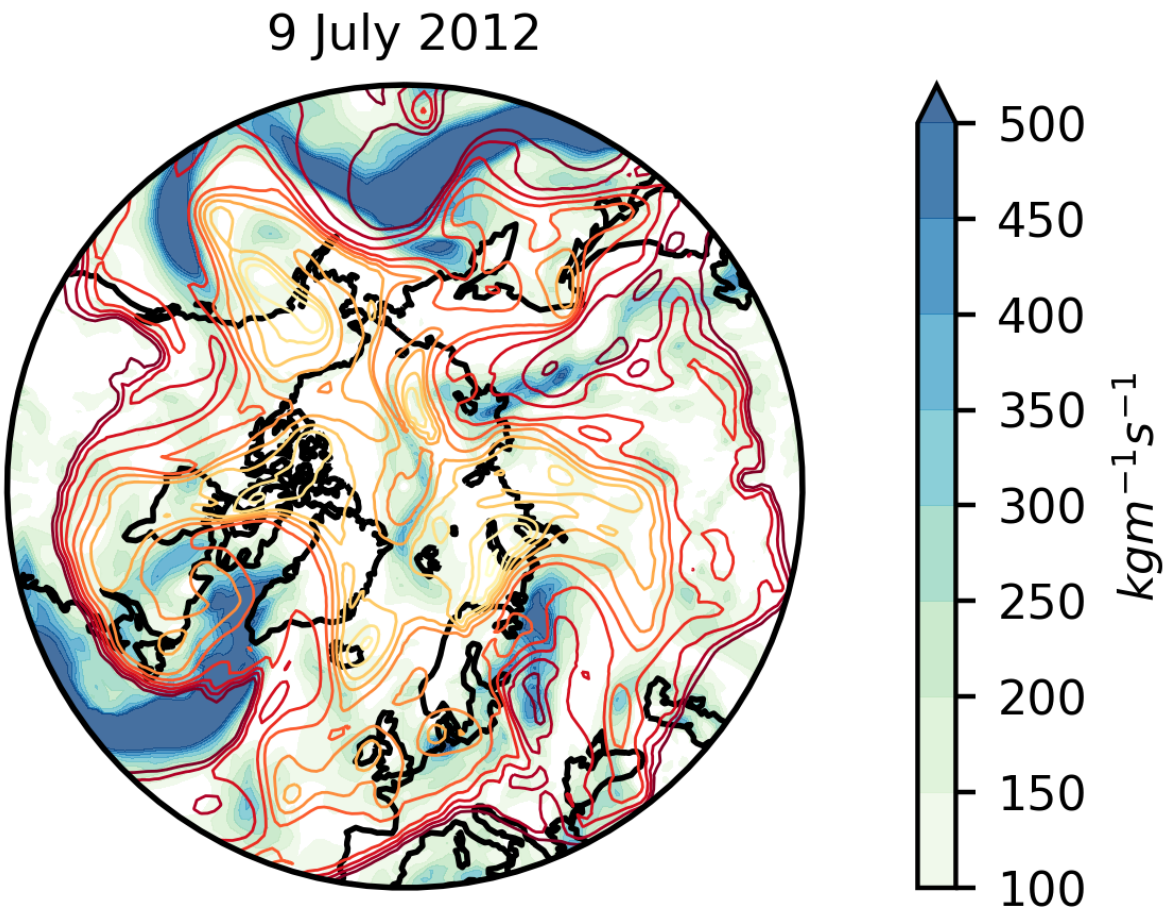

Figure 1.5. An example of a cyclonic wave breaking event associated with extreme moisture transport on 9 July 2012 over the North Atlantic, which later triggered a significant melt event over the Greenland ice sheet during 11–12 July 2012. Contours are potential temperatures (300–350K) at the 2PVU surface; filled contours are calculated integrated vapor transport. Data are from ERA5.

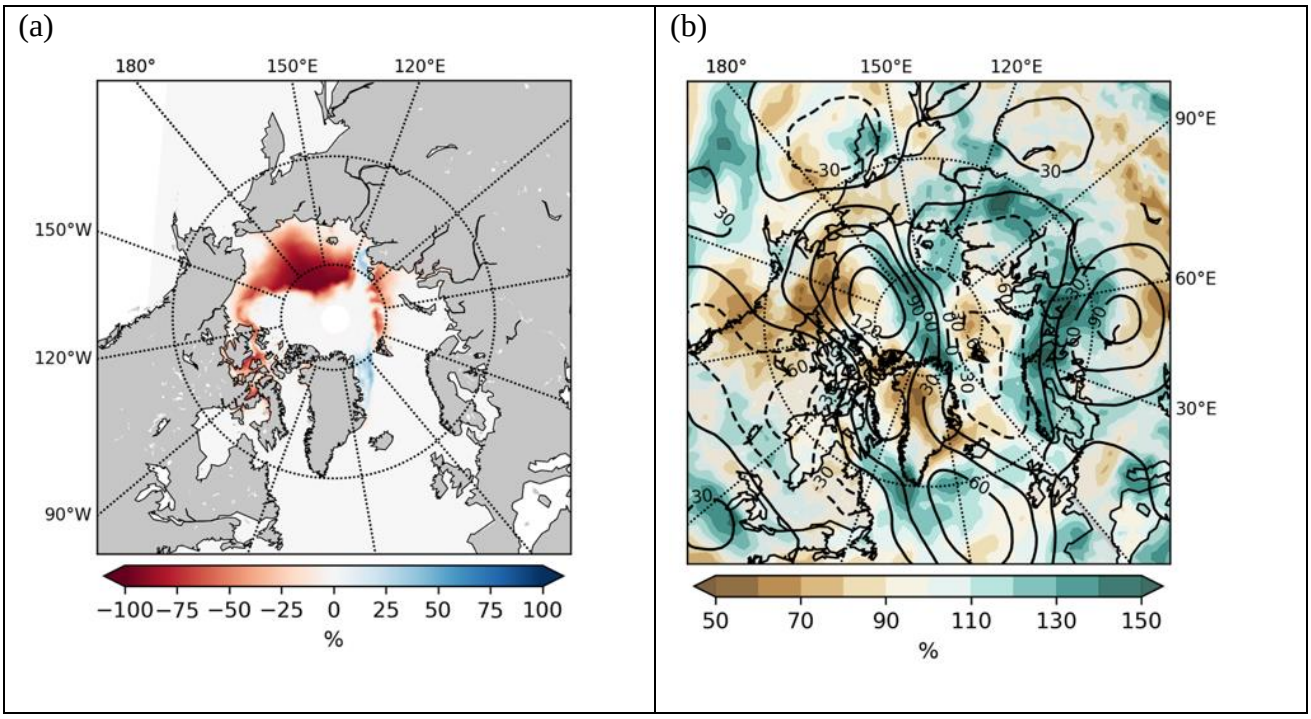

Figure 1.6. September 2007 sea ice concentration anomalies (a) and (b) August 2007 500hPa height with respect to climatology (gpm, 30hPa intervals, black contours) and integrated vapor transport (% relative to the 1981-2010 monthly mean). Sea ice data is from NOAA/NSIDC. Atmospheric anomalies are calculated composited using daily ERA5 data.

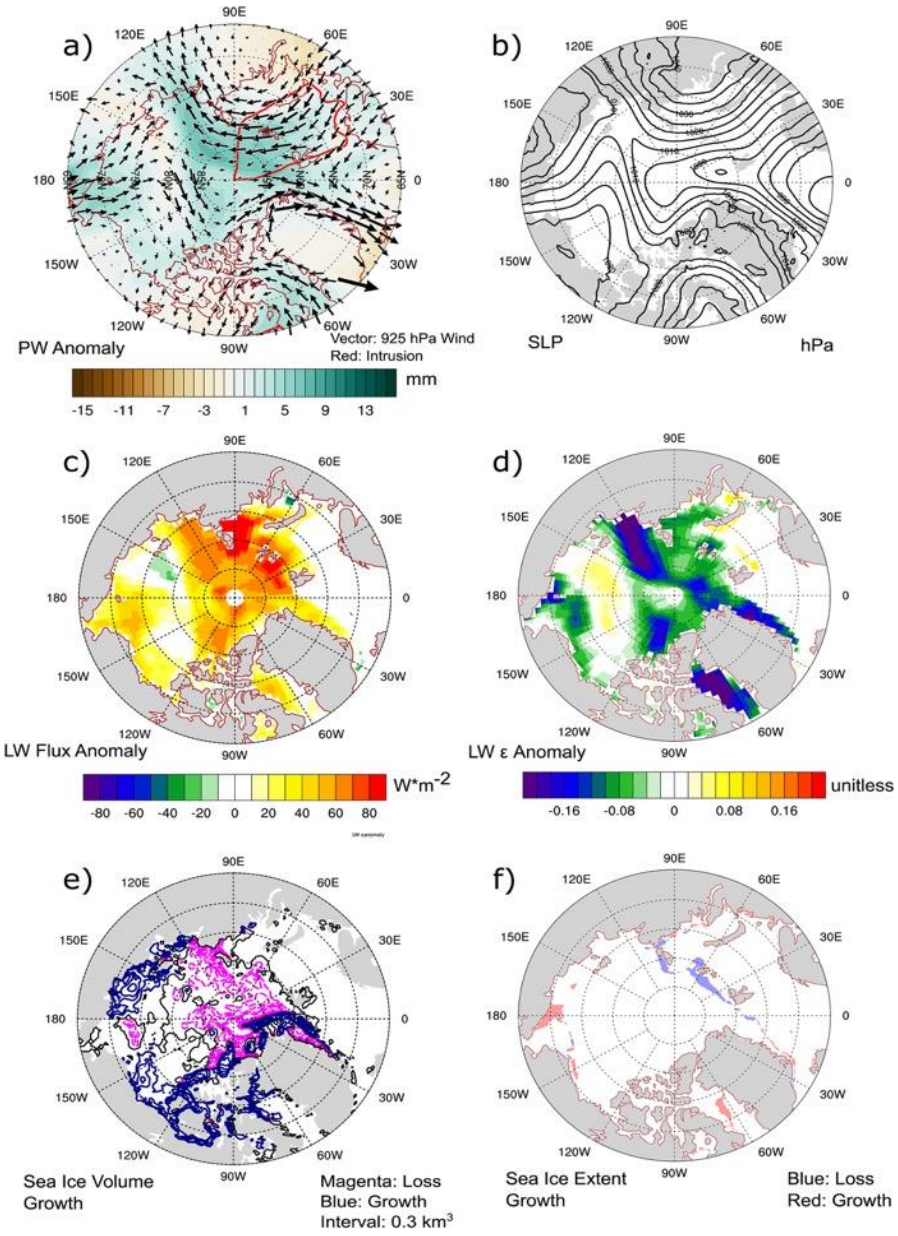

Figure 1.7. (a) Precipitable water anomalies (shading), 925 hPa winds (vectors), and the location of an atmospheric river (red contour) on 17 November 2016. For the same day, (b) Sea level pressure, (c) all-sky downwelling longwave surface flux anomalies, (d) anomalous cooling efficiency, (e) 5-day mean sea ice volume growth centered on 17 November 2016, and (f) changes in sea ice extent on 15-19 November 2016. Figure used with permission from Hegyi and Taylor (2018).

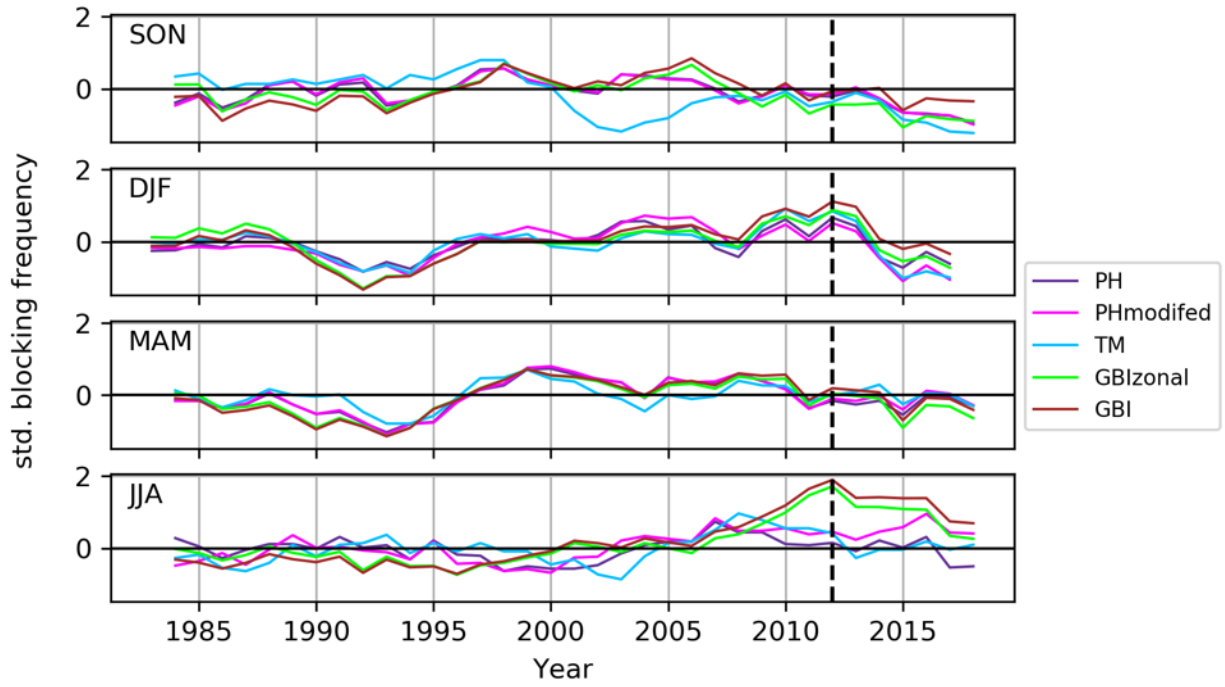

Figure 1.8. Comparison of standardized blocking frequency for Greenland blocks using different blocking detection methods for 1979–2018. The vertical dashed line indicates 2012, in which multiple blocking detection methods failed to identify the 2012 blocking over Greenland. Data are smoothed with a 3-year running mean. Figure used with permission from Wachowicz et al. (2021).

CHAPTER 2

QUANTIFYING TROPICAL CONTRIBUTIONS FROM EL NIÑO DIVERSITY TO ARCTIC MOISTURE TRANSPORT FROM ROSSBY WAVE BREAKING[1]

[1] Wachowicz, L.J. and T.L. Mote. To be submitted to *Climate Dynamics*.

Abstract

Recent losses in Arctic sea ice and increased melting of Greenland have been attributed to significant Arctic warming over the past several decades. While various feedbacks within the Arctic climate system have contributed to these losses, remote drivers of Arctic climate variability also play a role in the melting process through the increased advection of warm, moist air into the high latitudes. Stationary weather systems, such as blocking events, are connected with instances of enhanced moisture transport, where dynamic processes associated with Rossby wave breaking (RWB) can enhance these conditions. Mechanisms like RWB may be linked to variability in tropical Pacific sea surface temperatures (SSTs), such as El Niño-Southern Oscillation (ENSO), and its own variations broadly known as "ENSO diversity." To test if and how the variability of ENSO affects mid-to-high latitude RWB, RWB events are identified and classified according to their direction of breaking in two regions, the North Atlantic and North Pacific. Non-parametric statistics are used to assess trends in RWB activity and differences in moisture transport under different El Niño conditions (i.e., those originating from the Niño3 and Niño4 regions). Results show an increase in cyclonic RWB (CWB) in JJA and decrease in anticyclonic RWB (AWB) in SON in the North Atlantic. In the North Pacific AWB activity in MAM (JJA) appears to be increasing (decreasing). In both regions, CWB appears to result in greater moisture transport. The longitudinal position of positive SST anomalies appears to be most influential in the North Atlantic for AWB (CWB) in DJF (JJA), where positive SST anomalies in the Niño4 region appear to enhance moisture transport within the wave break. In the North Pacific, JJA moisture transport appears enhanced under positive Niño4 SST anomalies for AWB events.

2.1 Introduction

Recent Arctic warming has significantly impacted the Arctic cryosphere through its loss of sea ice (Onarheim et al., 2018), snow cover (Mudryk et al., 2018), permafrost (Biskaborn et al., 2019), and increased melt of the Greenland ice sheet (Van Den Broeke et al., 2016; Trusel et al., 2018). Ice and snow loss predominantly contribute to Arctic warming through the ice albedo feedback (Taylor et al., 2018; Thackeray and Hall, 2019; Duan et al., 2019). Other factors like increased warm, moist air advection in the lowest levels of the atmosphere are shown to enhance localized warming by affecting the lapse rate, water vapor, cloud albedo, and Planck feedbacks, among others (Kay et al., 2011; Pithan and Mauritsen, 2014; Feldl et al., 2020; Kay et al., 2016). In addition to high-latitude origins, contributions to boundary layer warming from feedbacks can be driven by lower-latitude processes (Yuan et al., 2018; Henderson et al., 2021), including those originating from tropical Pacific sea surface temperature (SST) variability (Hu et al., 2016; Kim and Kim, 2017; Matsumura and Kosaka, 2019).

The propagation of Rossby waves from the tropical Pacific can alter high-latitude atmospheric circulation (Ding et al., 2014; Feng et al., 2017), resulting in associated temperature and moisture anomalies (Li et al., 2019; Lim et al., 2019). Persistent anticyclonic anomalies, such as those from blocking, embedded within the Rossby waves can prevent the movement of cyclones, thus acting to increase heat and moisture transport into the high latitudes (Woods and Caballero, 2016; Kim and Kim, 2017; Yang and Magnusdottir, 2017; Wernli and Papritz, 2018). Previous research has noted that the strongest moisture transport into the Arctic occurs during Rossby wave breaking (RWB) (Liu and Barnes, 2015), a process which is closely connected to blocking (Masato et al., 2012; Masato et al., 2013a).

In addition to enhancing moist energy available for depleting the cryosphere, diabatic heating from latent heat release during RWB events plays a pivotal role in rapidly enhancing upper-level ridges (Franzke et al., 2011; Baggett et al., 2016; Zhang and Wang, 2018; Steinfeld and Pfahl, 2019), suggesting the connection between blocking anticyclones and RWB has implications for regional weather (Michel and Rivière, 2011; Ryoo et al., 2013; Moore et al., 2019;). Consequently, RWB activity, including its wave breaking properties (i.e., direction of breaking), has implications for seasonal forecasting through its influence on the Pacific-North American (PNA) and North Atlantic Oscillation (NAO) patterns (Woollings et al., 2008; Strong and Magnusdottir, 2008; Franzke et al., 2011). Both the PNA and NAO have strong connections to tropical SST variability associated with the El Niño-Southern Oscillation (ENSO) (Sheridan and Lee, 2012; Jiménez-Esteve and Domeisen, 2018; Zhang et al., 2019; Dai and Tan, 2019).

Understanding the unique ways in which ENSO variability ("diversity", Capotondi et al., 2015) has affected and will affect environmental change is of recent interest. Unlike a "canonical"-style El Niño, a westward shift in longitude of highest SST anomalies is expected during a "Modoki"-style El Niño (Ashok et al., 2007), which has been shown to have significantly different extratropical and Arctic responses when compared to the canonical El Niño (Hu et al., 2016; Feng et al., 2017; Li et al., 2019; Zhang et al., 2019). This longitudinal shift in El Niño has been observed as becoming more frequent (Yeh et al., 2009; Lee and McPhaden, 2010; Cai et al., 2014; Freund et al., 2019), leaving its impact on the Arctic cryosphere uncertain. In particular, the longitudinal variability of El Niño appears to affect both RWB frequencies and geography (e.g., Liu et al., 2014), leaving a comprehensive assessment of the connection of El Niño diversity, RWB activity, and moisture transport in the high latitudes to

be a first step at furthering our understanding of changes in the Arctic system. To accomplish this, this study looks to address three questions:

1) What are the spatio-temporal characteristics of high-latitude RWB?

2) How do these characteristics change as a result of tropical Pacific SST variability?

3) What is the implication of tropical Pacific SST variability on high-latitude moisture transport as a result of RWB?

2.2 Methods

2.2.1 One-Dimensional Rossby Wave Breaking Index

Mid- and high-latitude blocking commonly exhibits wave breaking characteristics (e.g., Masato et al., 2012). We first identify blocking events following methodology similar to that outlined in (Pelly and Hoskins, 2003), and build on that to categorize the block by its wave breaking direction (i.e., cyclonic or anticyclonic) (Masato et al., 2012; Masato et al., 2013a).

Blocking and its coincident wave breaking characteristics are identified using daily 1200 UTC potential temperature (θ) at the dynamic tropopause (2PVU) for January 1979 through December 2018 using 1° ERA5 reanalysis (Hersbach et al., 2020). On the 2PVU surface, instances of a reversal of the meridional potential gradient at a given latitude (ϕ_o) are identified if B > 0, where B is calculated by

$$B = \frac{2}{\Delta\phi}\int_{\phi_o}^{\phi_o+\frac{\Delta\phi}{2}} \theta d\phi - \frac{2}{\Delta\phi}\int_{\phi_o-\frac{\Delta\phi}{2}}^{\phi_o} \theta d\phi \qquad (1)$$

This calculation follows PH03 using a ϕ_o as a central blocking latitude and considers the gradient over a 30° window ($\Delta\phi$). The value of $\phi_o$varies longitudinally due to its value being determined from bandpass eddy kinetic energy (EKE) as the latitude of maximum EKE, to best account for climatological storm tracks. However, unlike PH03, we allow ϕ_o to vary seasonally

to better capture wave breaking (e.g., Masato et al., 2012; Masato et al., 2013b), and because of its ability to better capture Greenland blocking (Wachowicz et al., 2021).

Blocking is further categorized into cyclonic or anticyclonic wave breaking based on the direction of the wave break (DB), as described in (Masato et al., 2012). Starting from 0° to 359° longitude, the difference in average θ calculated from θ_N and θ_S (Figure 2.1), the difference in θ at each longitude (λ_f minus λ_o). Events are considered anticyclonic (cyclonic) wave breaking if DB > 0.4 (< -0.4) for no more than 40° longitude capture synoptic scale events (Bowley et al., 2019). The threshold of DB was selected somewhat subjectively and is more restrictive than as mentioned in (Masato et al., 2012), but does not appear to significantly change the number of events identified. Unless noted otherwise, wave breaking events persisting for 3 or more consecutive days are assessed. While this is a lower temporal threshold compared to the 5-day threshold used in Masato et al. (2012), the less restrictive criterion allows for a larger sample size for compositing.

2.2.2 Moisture Transport

Moisture transport is commonly quantified in high latitudes using integrated vapor transport (IVT) which is calculated using u- and v-winds and specific humidity (q). We calculate daily IVT following (Mattingly et al., 2018) for the 1000 to 200 hPa pressure layer (dp), such that

$$IVT = \frac{1}{g}\int_{1000\ hPa}^{200\ hPa} qv\ dp \qquad (2)$$

In this calculation, g is the gravitational constant (9.81 m s^{-2}) and v is the vector wind (calculated from u- and v-winds). In addition to raw IVT values, IVT is composited with respect to a seasonal climatology or a predetermined subset to produce respective values of the percentage of

IVT compared to all events, which is useful in high-latitude regions with climatologically low temperatures and low moisture content.

2.2.3 ENSO Variability

There exists a diverse array of ENSO indices that are used to identify El Niño events. For this study, we use the 3-month running mean of detrended sea surface temperature (SST) anomalies from ERSST v5 data available from 1920-2018 (Figure 2.2). To explore variability in ENSO diversity, we use area weighted average SST anomalies above/below the ± 0.5°C threshold in both the Niño-3 (-5° to 5°N, 210° to 270°E) and Niño-4 (-5° to 5° N, 160° to 210° E) regions, as defined by the Climate Prediction Center, similar to methodology used by (Li et al., 2019). While we do not aim to identify specific El Niño events, we do refer to seasons with positive SST anomalies from each region as "El Niño3" or "El Niño4" for simplicity.

2.3 RWB and Moisture Transport

2.3.1 Climatology

Blocking with wave breaking is a relatively infrequent phenomenon, with typically fewer than 30 separate events per year, regardless of the type of wave break (Figure 2.3, top). Throughout most of the Northern Hemisphere, anticyclonic wave breaking (AWB) is the most common type, except for cyclonic wave breaking (CWB) appearing more frequently over the North Atlantic region regardless of season. Likewise, AWB is the most dominant type roughly over Europe and Eurasia during SON and DJF and the Pacific and North America in JJA (Figure 2.3, middle). CWB, on the other hand, occurs most frequently in the North Atlantic, particularly

in the westernmost portion of the region, in MAM and JJA (Figure 2.3, bottom). Likewise, CWB in JJA appears to occur frequently in the eastern Siberia and the North Pacific.

Figure 2.4 shows the persistence of wave breaking characteristics associated with the blocking for North Atlantic (Figure 2.4a) and North Pacific (Figure 2.4b) when considering events lasting 2 or more days. In the North Atlantic (Figure 2.4a), AWB and CWB generally show no difference in persistence when considering all wave break events. When classified by season, however, relatively fatter tails on the distributions for MAM and JJA show up for CWB compared to AWB suggesting more persistent events in warmer months (i.e., exceeding 5-6 days). Conversely, the distributions for SON and DJF are fatter for CWB before the 5- to 6-day persistence bin, suggesting most cold season events are shorter lived.

In terms of the total number of events in the North Pacific, we find little difference between the frequency of AWB and CWB (Figure 2.4b). We appear to capture CWB more frequently than AWB in the North Pacific during DJF and MAM. For both AWB and CWB in JJA, the frequency of more persistent events is greater than for the other seasons, as shown by the extended, fatter tails in the distributions exceeding 5 days.

To assess whether there are trends in the number of RWB days in both basins, the total number of days meeting wave breaking criteria for events lasting two or more days are computed each season as standardized anomalies (Figure 2.5). In the North Atlantic (Figure 2.5a), although the raw frequencies do not suggest any prevalent trends in the occurrence of RWB, the 3-year running mean of the seasonal RWB anomalies indicates an increase in AWB days in SON and CWB days in JJA, based on the results of a Mann-Kendall test ($p < 0.05$). These trends complement findings from Wachowicz et al. (2021), who noted potential decreases in SON

Greenland blocking activity and increases in JJA Greenland blocking, though the identification of these trends is sensitive to how Greenland blocking is identified.

A similar analysis for the North Pacific suggests changes in RWB frequency are also dependent on season (Figure 2.5b). AWB activity in MAM and JJA show positive and negative trends in frequency, respectively, and appear qualitatively consistent with findings from (Bowley et al., 2019). The number of days with CWB is significantly decreasing in SON, which is contradictory to findings from Bowley et al. (2019b).

2.3.2 Moisture Transport from RWB

Figures 2.6 and 2.7 show the temporal progression of moisture transport during wave breaking for DJF (Figure 2.6) and JJA (Figure 2.7). Notable for DJF events are high IVT exceeding 200 kg $m^{-1}s^{-1}$ within the warm tongue approximately 1 day prior to the start of the wave break for both AWB and CWB (Figure 2.6). The IVT values appear strongest during CWB (exceeding 250 kg $m^{-1}s^{-1}$) compared to those occurring during AWB (exceeding 200 kg $m^{-1}s^{-1}$). A similar relationship between wave breaking and IVT appears for JJA events, with IVT values exceeding 150 kg $m^{-1}s^{-1}$ for AWB compared to 200 kg $m^{-1}s^{-1}$ for CWB events (Figure 2.7), with maximum values occurring the day of the start of the wave break, consistent with Liu and Barnes (2015).

Figure 2.8 shows comparable wintertime IVT values in the North Pacific compared to the North Atlantic (Figure 2.6), with values exceeding 200 kg $m^{-1}s^{-1}$ for both AWB and CWB. However, IVT appears strongest approximately the day prior to the start of AWB, with values of 250 kg $m^{-1}s^{-1}$ or greater. The initial day of the CWB event, on the other hand, shows strongest moisture transport with IVT values exceeding 275 kg $m^{-1}s^{-1}$ within the warm sector of the cyclone. While DJF wave breaking indicated strong moisture transport, JJA IVT values appear to

be strongest on the day of the start of the wave break with values exceeding 225 kg $m^{-1}s^{-1}$ within the warm tongue (Figure 2.9).

2.4 Connections to ENSO

2.4.1 North Atlantic

We composite RWB events under seasons of positive SST anomalies in the Niño-3 and Niño-4 regions to assess whether the location of tropical SST anomalies influences the amount of moisture transported during the wave break. For the North Atlantic in DJF (Figure 2.10), under El Niño3 and El Niño4 SST anomalies, there are prominent above average IVT anomalies to the north of the AWB, where this positive anomaly is significantly greater for events occurring associated with El Niño4 anomalies. For El Niño4 AWB events, there is significantly less IVT associated with the cyclone to the east of the centroid, suggesting that in the winter, the region within the AWB may transport more moisture under El Niño4 conditions. For CWB, the moisture transport within the region of the wave break appears to be significantly less under El Niño4 conditions compared to El Niño3.

In JJA with positive SST anomalies, the IVT within the North Atlantic AWB region is less than 75% of all documented AWB events (Figure 2.11). IVT is significantly reduced in this region for the Niño4 events compared to Niño3, suggesting that JJA AWB under El Niño4 conditions results in less moisture transport compared to AWB under El Niño3 conditions. On the other hand, CWB events show increased moisture transport within the wave breaking region that exceeds 150% compared to all CWB for El Niño4 events. This enhanced IVT near the centroid of the CWB events is significantly higher than the El Niño3 events. These findings

suggest that El Niño4 SST anomalies may result in increased moisture transport during CWB events in the North Atlantic during the summer.

2.4.2 North Pacific

When considering the effect of positive SST anomalies on moisture transport from RWB in the North Pacific (Figure 2.12), there is greater moisture transport for AWB in JJA under El Niño4 conditions compared to El Niño3. This significant increase in IVT to the north of the centroid under El Niño4 conditions is countered with significantly less IVT to the south of the wave break. Under CWB conditions occurring associated with El Niño3 anomalies, there is greater moisture transport (1.5 times the mean) within the wave break area. Despite lower IVT in this region for events occurring under El Niño4 conditions, the composite difference between the two do not indicate El Niño4 CWB is significantly drier. In summary for JJA, positive SST anomalies in the Niño-4 region may yield higher poleward moisture transport during AWB events compared to those associated with anomalies in the Niño-3 region. Given the small sample size of DJF events in the North Pacific more broadly, we opt to exclude DJF in the North Pacific, as a similar analysis shows so few AWB events that we cannot discern a signal in IVT.

2.5 Discussion and Summary

Moisture transport into the high latitudes is instrumental in driving regional climate variability, particularly through its impact on land and sea ice. The connection of Rossby wave breaking (RWB) to dynamic weather systems, such as atmospheric blocking which are associated linked to extreme moisture transport into the high latitudes, leads to surface hydroclimatological implications. Understanding the mechanisms by which moisture reaches the Arctic (i.e., RWB) and how these mechanisms have varied and will vary over time allows us to

better understand their role in high-latitude hydroclimate in both past and future climates. Therefore, this study attempts to further assess the role of RWB in high-latitude moisture transport and its relationship to tropical Pacific SSTs (i.e., ENSO).

After characterizing blocking events over the North Atlantic and Pacific oceans as exhibiting CWB and AWB, results suggest a particular influence of CWB in the North Atlantic, with both wave break types of relatively equal importance in the North Pacific. While most studies focused on RWB have typically focused on the winter season (DJF) (e.g., Strong and Magnusdottir, 2008; Masato et al., 2012), we have expanded our analysis to include all seasons. By doing so, we show in the North Atlantic the number of days exhibiting CWB characteristics in JJA have significantly increased, which corresponds to observed changes in the negative phase of the NAO, increased Greenland blocking conditions, and increased moisture transport (e.g., Mattingly et al., 2016; Hanna et al., 2018; Barrett et al., 2020; Wachowicz et al., 2021). This increase in JJA CWB frequency in the North Atlantic is important considering our findings suggest higher IVT under CWB conditions, especially in JJA. While this may be due to shifts in the jet stream (e.g., Liu and Barnes 2015), it does suggest large-scale dynamical linkages may vary seasonally and ultimately act to drive more moisture into the North Atlantic in warmer months. Likewise, decreases in observed AWB days have occurred in SON, appear to be qualitatively consistent with findings from Bowley et al. (2019b). This trend is particularly interesting, as changes in zonal and meridional wind, as discussed in Bowley et al. (2019b), do not appear to fully explain its existence.

While the significant North Pacific AWB trends in this paper appear to complement findings of previous climatologies (e.g., Bowley et al. 2019b), we note that our analysis for this region does not appear to replicate similar findings for trends in both CWB, more generally, and

in particular the DJF season for AWB. We believe this may be explained through the methodology used. The RWB identification technique employed in this study is originally based on a blocking methodology from Pelly and Hoskins (2003) and later adapted to quantify RWB characteristics of blocking events by considering the direction of isentrope overturning (cyclonic or anticyclonic), as outlined in Masato et al. (2012). The lack of AWB identified in DJF in the North Pacific remains consistent with findings from Masato et al. (2012), who noted that cyclonic blocking was the dominant type in this region.

Moreover, blocking and wave breaking identification from the seasonal EKE may remain dependent on interannual variability, including the NAO and Pacific-North American (PNA) patterns. The positive phase of the PNA, for example, is sensitive to moisture transport from CWB (Franzke et al., 2011; Baggett et al., 2016). Diabatic heating from latent heat release during CWB acts to amplify planetary waves (Baggett et al., 2016), and may promote downstream blocked conditions (Pfahl et al., 2015; Steinfeld and Pfahl, 2019). Results presented in this paper suggest that moisture transport may be greater under CWB conditions in both the North Atlantic and Pacific. Many models fail to accurately represent both diabatic heating within the warm conveyor belt of extratropical cyclones (Baggett et al., 2016; Zhang and Wang, 2018) and tend to underestimate blocking (e.g., Schiemann et al., 2017; Simpson et al., 2020), leaving future work to examine the interconnectedness of CWB and blocking activity in more detail.

In both the North Atlantic and North Pacific, the theory that tropical Pacific convection and SSTs trigger extratropical responses in atmospheric circulation (e.g., Ding et al., 2014; Baggett et al., 2016; Feng et al., 2017; Matsumura and Kosaka, 2019) has motivated us to further quantify how positive SST anomalies in the tropical Pacific affect RWB and moisture transport. In DJF in the North Atlantic we generally find positive IVT anomalies under AWB, independent

of the location of positive SST anomalies, but there is significantly higher IVT during AWB under El Niño4 conditions. On the other hand, in JJA, we find significantly higher IVT during CWB under El Niño4 conditions. Likewise, in JJA, there is evidence of greater moisture transport in the North Pacific during AWB under El Niño4 conditions.

Although not explicitly addressed, results from this study point towards a possible connection between wave breaking activity and long, narrow plumes of extreme moisture transport known as "atmospheric rivers" in the Arctic (e.g., Mattingly et al., 2016, Mattingly et al., 2018). Current research has shown significant increases in moisture transport into the polar regions, including the North Atlantic more specifically (e.g., Lavers et al., 2015; Mattingly et al., 2016), which are linked to Greenland blocking (e.g., Barrett et al., 2020). However, given that maximum IVT appears to occur within 0 to 1 days ahead of a wave break, the nature of high IVT values, such as those associated with an atmospheric river, to occur ahead of a wave break as shown in this study may allow for the prediction of extreme, persistent blocking conditions.

Moreover, while both types of ENSO events are thought to become more extreme in the future (Cai et al., 2014; Cai et al., 2018), the cause of these shifts remain debated due to uncertainties in ENSO representation in climate models (Zheng et al., 2017; Maher et al., 2018). Regardless of the cause of these changes in ENSO, the results presented in this paper show a distinct hydroclimatological response in high-latitude moisture transport from RWB, particularly in summer, which appears dependent on the type of El Niño conditions. Since extreme moisture transport has shown to significantly alter sea ice cover and produce melting in Greenland (e.g., Yang and Magnusdottir, 2017; Mattingly et al., 2018), future work should aim to quantify impacts of ENSO diversity on the Arctic atmosphere and its impact on the cryosphere.

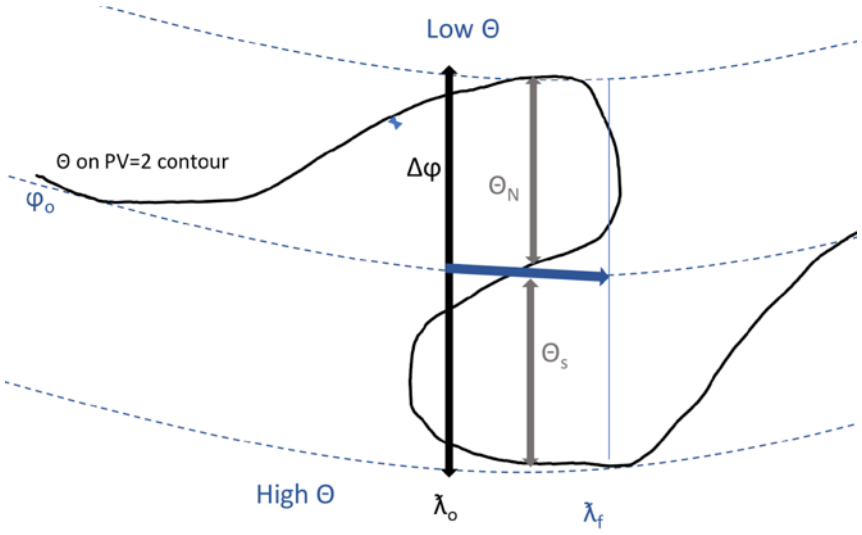

Figure 2.1. A schematic representing key parameters used in blocking and Rossby wave breaking detection about a given latitude (ϕ_o) on the 2PVU surface. The blocking identification is based on Figure 3 of Pelly and Hoskins (2003). Rossby wave breaking direction is based on average θ change between two longitudes (λ_f and λ_o) and is adapted from Masato et al. (2012), their Figure 2.

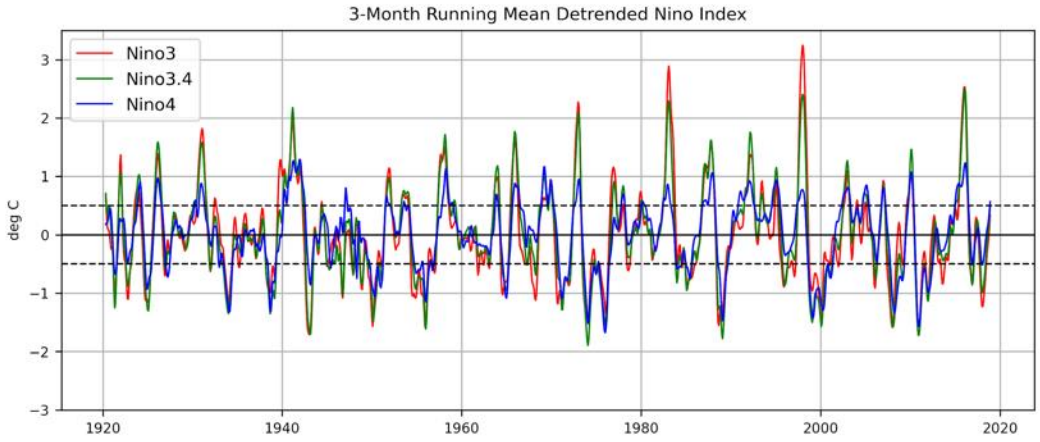

Figure 2.2. Time series of detrended area-weighted monthly SST anomalies from 1920-2018 for the Niño3, Niño3.4, and Niño4 regions as defined by the Climate Prediction Center. Raw monthly SST anomalies were obtained from the National Center for Atmospheric Research Climate Variability Diagnostics Package.

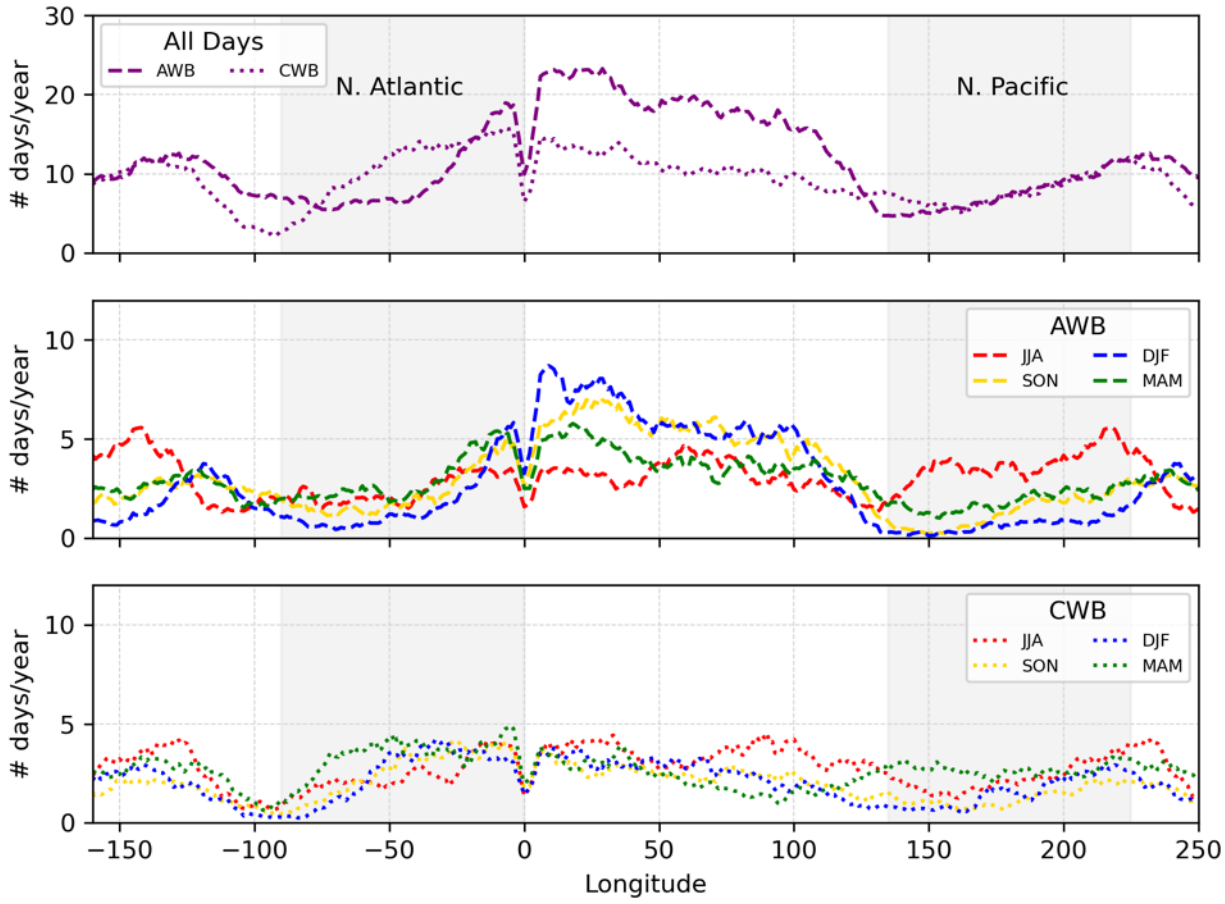

Figure 2.3. Average number of days per season with wave breaking characteristics (+/- 0.4DB threshold), at each longitude. Top panel includes total anticyclonic wave breaking (AWB) and cyclonic wave breaking (CWB) events, middle panel shows seasonal breakdown of AWB events, and the bottom panel shows seasonal breakdown of the CWB events. Frequencies are smoothed with a 1° longitude running mean. Longitudinal range for the North Atlantic (270-360°) and North Pacific (135-225°) are shaded gray.

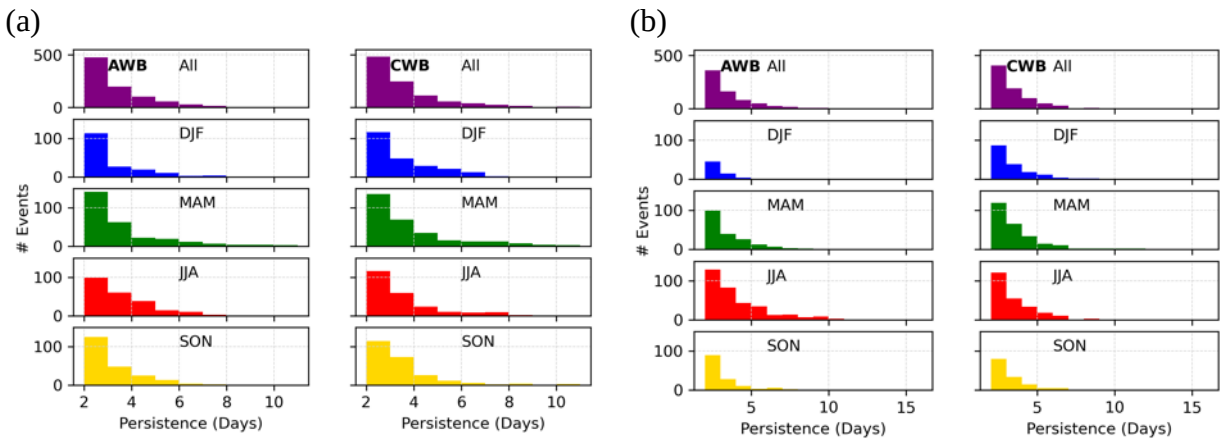

Figure 2.4. Total number of wave breaking events which persisted 2 or more days for (a) North Atlantic and (b) North Pacific.

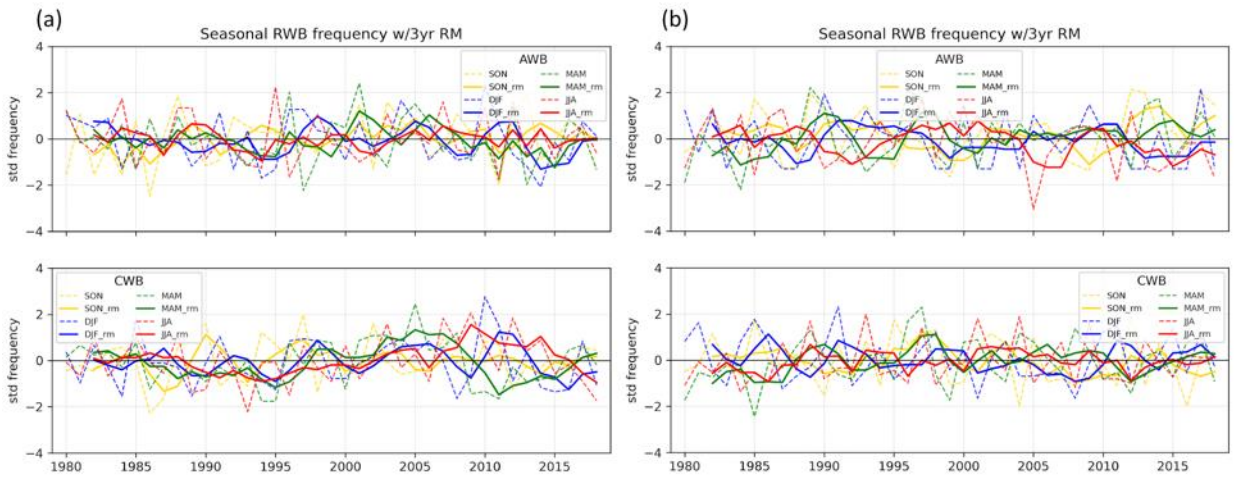

Figure 2.5. Standardized counts of number of days per season with wave breaking criteria for (a) North Atlantic and (b) North Pacific. Included are all events lasting 2 or more days. A 3-year running mean is applied (bolded line). Frequencies are standardized with respect to the 1981-2010 mean.

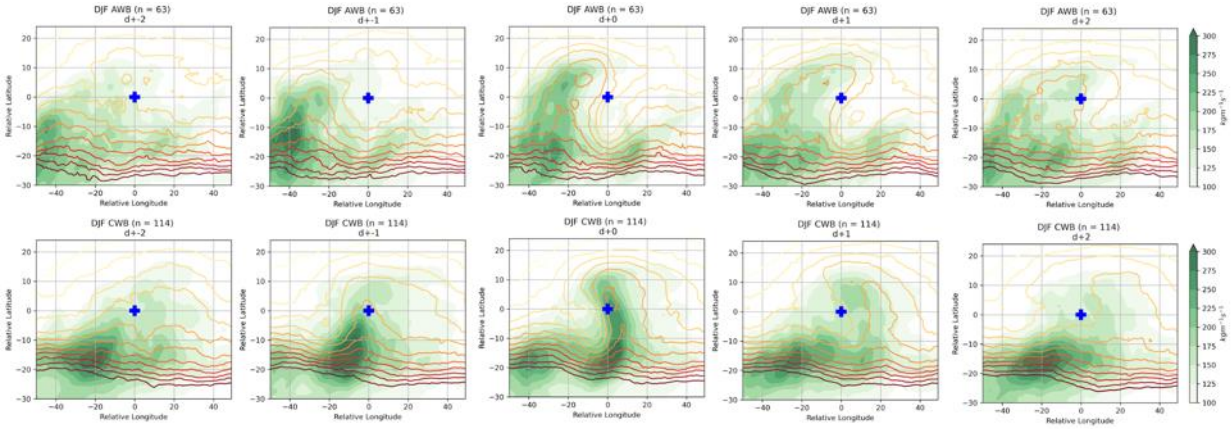

Figure 2.6. Lagged IVT (filled) and θ at 2PV (contours) composites of DJF North Atlantic wave break events lasting 3 or more days. Shown are day of initiation (d+0) and ± 1, 2 days after (before).

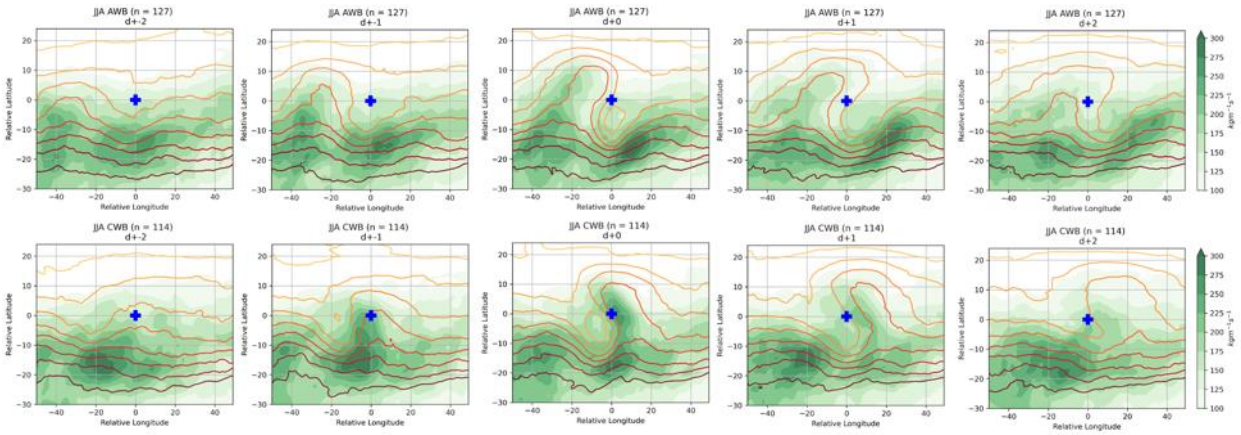

Figure 2.7. Lagged IVT (filled) and θ at 2PV (contours) composites of JJA North Atlantic wave break events lasting 3 or more days. Shown are day of initiation (d+0) and ± 1, 2 days after (before).

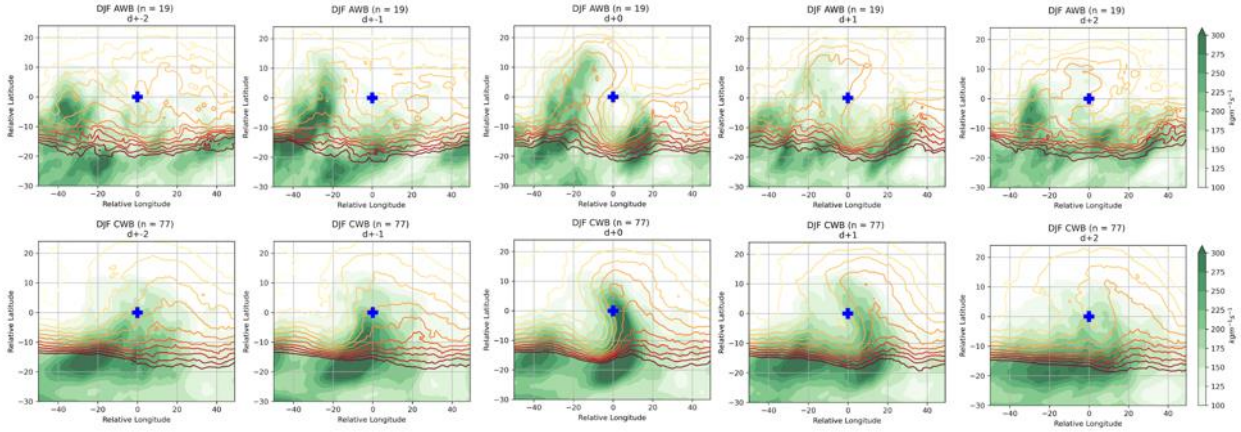

Figure 2.8. Same as Figure 2.6 but for the North Pacific.

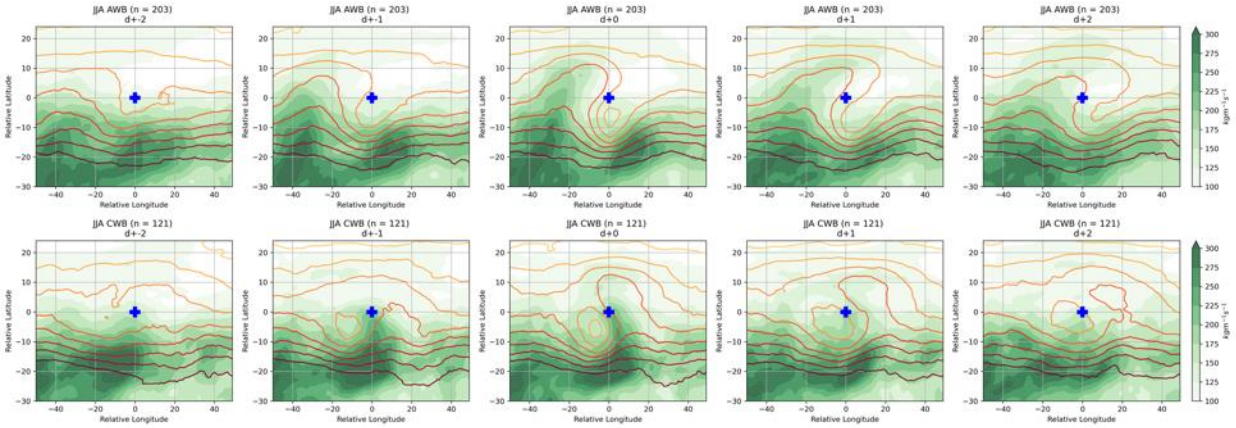

Figure 2.9. Same as Figure 2.7 but for the North Pacific.

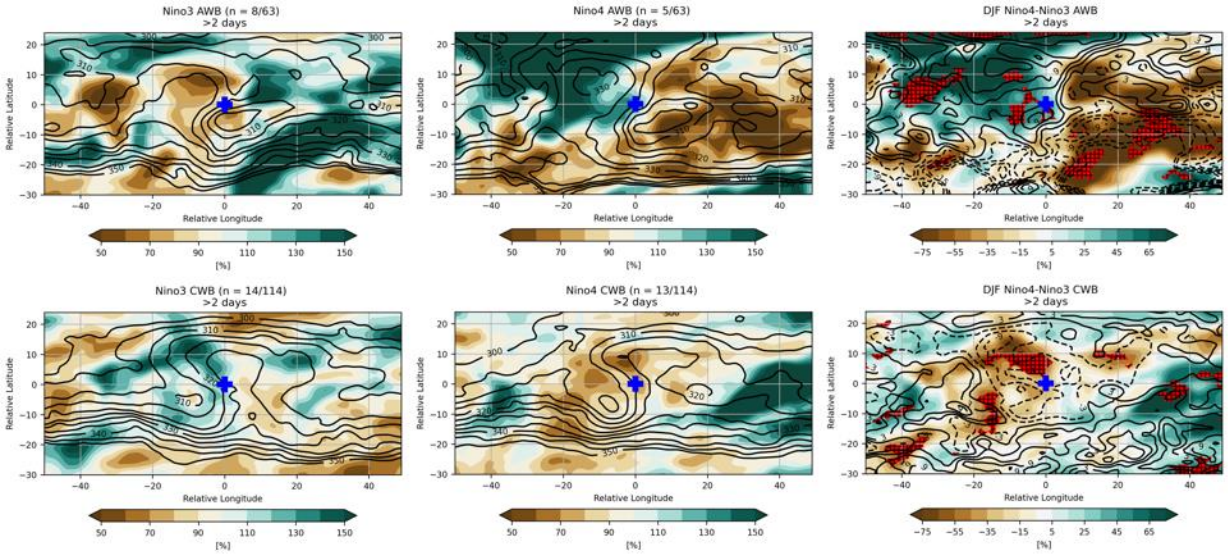

Figure 2.10. North Atlantic %IVT relative to all RWB events lasting 3 or more days in DJF seasons of positive SST anomalies. Significance at 90% using Mann Whitney U test (red shading).

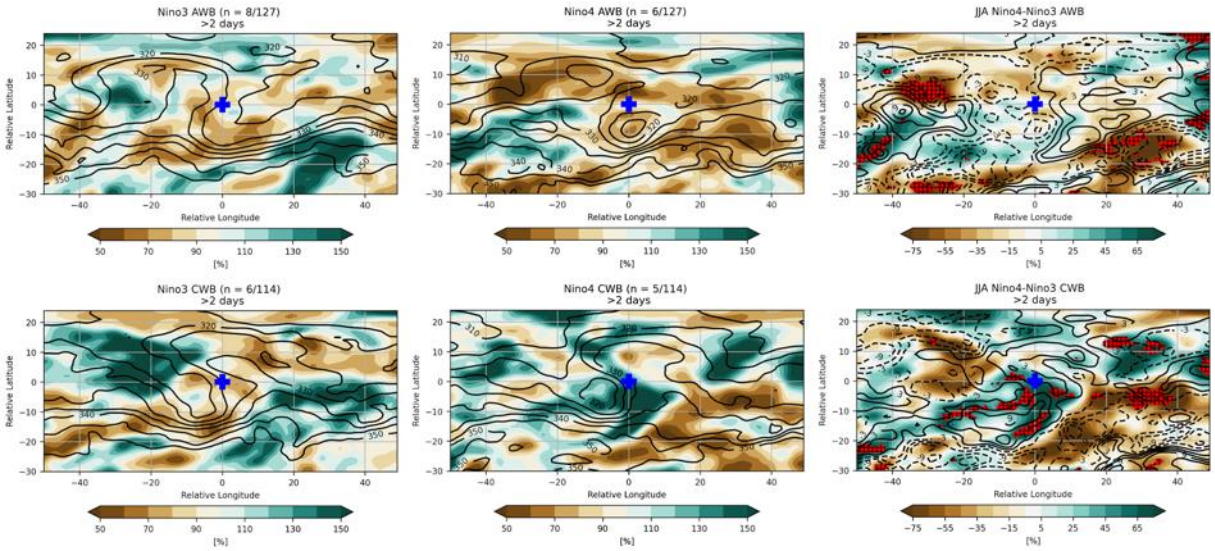

Figure 2.11. North Atlantic %IVT relative to all RWB events lasting 3 or more days in JJA seasons of positive SST anomalies. Significance at 90% using Mann Whitney U test (red shading).

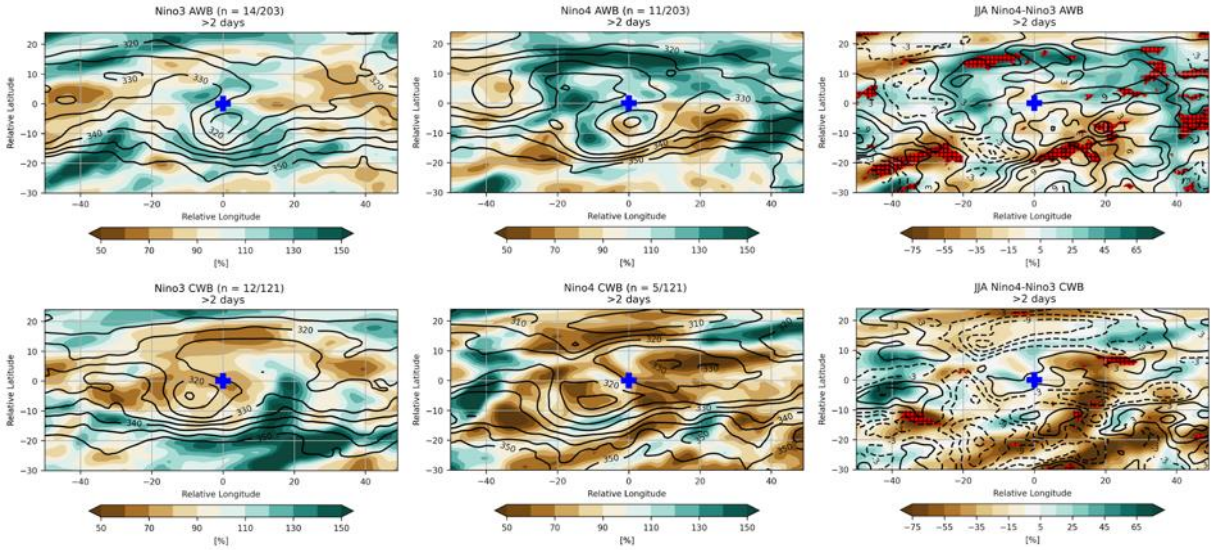

Figure 2.12. Same as Figure 2.11, except for the North Pacific.

CHAPTER 3

CONNECTING ENSO AND ARCTIC SEA ICE SPATIAL AND SEASONAL VARIABILITY THROUGH ATMOSPHERIC LINKAGES[2]

[2] Wachowicz, L.J. and T.L. Mote. To be submitted to *Journal of Climate*.

Abstract

Arctic sea ice plays an integral role in Arctic and global climate through various physical feedbacks within the climate system. Tropical processes, including those associated with El Niño-Southern Oscillation (ENSO), can affect Arctic sea ice and related feedbacks through the transport of moist and dry energy into the Arctic via planetary Rossby waves. Here, we establish a connection between Arctic sea ice and tropical Pacific sea surface temperatures (SSTs) associated with ENSO using monthly observed sea ice concentration and SST datasets. We consider tropical SST anomalies are calculated for the East Pacific (EP) Niño3 index and Central Pacific (CP) Niño4 index regions. We composite circulation and moisture transport anomalies, as these variables are closely connected to high-latitude blocking and associated moisture transport, which have previously been known to significantly impact sea ice. The Community Earth Systems Model Large Ensemble (CESM LE) simulations are further used to assess whether a tropical to polar teleconnection exists in a fully coupled model.

For winter (summer) SST anomalies, a lag was found in Arctic sea ice response about 1 to 3 (0 to 1) months after the SSTs anomalies are present, with the greatest responses in the Beaufort Sea and Canadian Archipelago (Canadian Archipelago and Central Arctic) regions. Summer sea ice response in the Canadian Archipelago and Central Arctic regions appear immediately and can persist for 1 to 4 months, or longer. Summer sea ice in the Canadian Archipelago and Central Arctic regions appears most sensitive to the CP El Niño, as exhibited by significant positive correlations. Under CP Niño/Niña conditions, the Canadian Archipelago region undergoes more moisture transport within the region, but has less sea ice loss, as confirmed by previous studies. CESM LE shows a connection between ENSO and sea ice with 0 to 1 month lag in winter, with little difference due to ENSO diversity compared to observations,

likely due to its representation of overall weaker upper-level circulation regimes compared to observations. The results presented here show evidence of ENSO's variability in influencing seasonal sea ice in the Arctic. Improved representation of high-latitude atmospheric patterns affecting sea ice, such as those associated with enhanced cloud cover, may improve the representation of teleconnections in models going forward.

3.1 Introduction

Arctic sea ice strongly modulates Arctic and global climate by influencing various physical feedbacks contributing to Arctic amplification. Summer sea ice extent has decreased nearly 15% compared to the 1981-2010 average (Arctic Report Card 2019). Recent losses in summer sea ice allow open water to absorb more incoming solar radiation, which increases ocean temperatures and slows winter sea ice growth through latent heat release, leading to enhanced regional warming through an ice-albedo feedback (Stroeve and Notz, 2018). However, sea ice loss is not spatially or temporally uniform (Onarheim et al., 2018; Peng and Meier, 2018), thus illustrating complex spatiotemporal interactions between sea and its environment.

Tropical processes, including those associated with El Niño-Southern Oscillation (ENSO), can transport moist and dry energy into the Arctic via planetary Rossby waves (Kim and Kim, 2017; Ye and Jung, 2019), which enhance other intra-Arctic feedbacks, such as the lapse rate, Planck, cloud and water vapor feedbacks (Taylor et al., 2013; Pithan and Mauritsen, 2014; Kay et al. 2016; Taylor et al., 2018; Huang et al., 2019; Feldl et al. 2020), ultimately affecting sea ice. Stroeve and Notz (2018) suggest ENSO, in particular, could precondition the mean background state of the climate, further suggesting that the nature of the relationship between sea ice and the Arctic atmospheric circulation through such feedbacks may be strongly

dependent on tropical forcing. Disturbances embedded within extra-Arctic-induced Rossby waves increase heat and moisture transport into the high-latitudes and consequently have a strong impact on sea ice (Woods and Caballero, 2016; Kim and Kim, 2017; Yang and Magnusdottir, 2017; Wernli and Papritz, 2018). Moreover, Rossby wave breaking activity increases high-latitude moisture transport (Liu and Barnes, 2015) and is dependent on ENSO and intra-ENSO variability (Liu et al., 2014; Liu and Barnes, 2015; Bowley et al., 2019b). Taken altogether, a thorough understanding of seasonal sea ice variability must include complex tropical-to-Arctic processes and their variability.

Variability within ENSO itself, sometimes referred to as "ENSO diversity" (e.g., Capotondi et al., 2015), also shows unique mid- to high-latitude signals (Feng et al., 2017; Bayr et al., 2018; Li et al., 2019; Zhang et al., 2019). The longitude of the Pacific SST anomalies during ENSO shows substantially different signals regionally and seasonally in Arctic surface air temperature (Li et al., 2019) and sea ice responses (Hu et al., 2016). For example, significant warming and enhanced moisture content over Greenland coincide with a phenomenon known as "Modoki" El Niño, which is when positive SST anomalies originate in the Central Pacific (Ashok et al., 2007; Li et al., 2019; Lim et al., 2019) as compared to Eastern "canonical" Pacific (EP) El Niño. Notably, a longitudinal shift in El Niño has been observed as becoming more frequent (Yeh et al., 2009; Lee and McPhaden, 2010; Cai et al., 2014; Freund et al., 2019), requiring a more comprehensive assessment of its regional and seasonal impact on the Arctic cryosphere.

To complicate matters, the coupled relationship of sea ice and the atmosphere is not well simulated in climate models (Ding et al., 2017; Mioduszewski et al., 2019; Dai et al., 2019). Model simulations of future climate states indicate that high-latitude moisture transport will

increase in the future (Lavers et al., 2015; Woods et al., 2017). Additionally, the Arctic is at risk of becoming ice-free in summer by 2040 (DeRepentigny et al., 2020). Because many climate models fail to adequately represent mid- to high-latitude atmospheric circulation (Kay et al., 2015; Hanna et al., 2018a; Simpson et al., 2020; Davini and D'Andrea, 2020;), moisture transport (Woods et al., 2017; Yang and Magnusdottir, 2018), ENSO diversity (Deser et al., 2017; Bayr et al., 2018; Zhang et al., 2019; Capotondi et al., 2020b), leaving significant gaps in understanding the impact of any combination of these on Arctic sea ice is detrimental when trying to identify key processes contributing to this ice loss.

Therefore, this paper seeks to 1) identify ENSO's impact on Arctic sea ice through various atmospheric pathways and 2) assess whether these relationships exist within climate model simulations. We first conduct a comprehensive analysis of lagged responses of sea ice to tropical Pacific SST variability, in which we show the spatiotemporal effects of ENSO diversity on Arctic sea ice by considering both winter and summer ENSO events. We then attempt to quantify a similar response in a suite of fully coupled climate model simulations. Lastly, we use composite analysis to discern high-impact atmospheric circulation patterns associated with ENSO-related SST anomalies, which may be contributing to ENSO-driven sea ice loss.

3.2 Methodology

3.2.1 Observational Datasets

To establish a connection between Arctic sea ice and tropical Pacific SSTs, such as those associated with ENSO, we use a monthly sea ice concentration dataset derived from in situ and remotely sensed sea ice observations (Walsh et al., 2019), available from https://nsidc.org/data/G10010/versions/2. This dataset provides monthly spatial average sea ice

concentration for the entire Arctic basin, as well as monthly average sea ice area for each region, extending from 1850–2017. Given the inconsistencies in the observation record prior to the satellite era (i.e, 1979), we limit our analysis from 1979 to 2017 to maintain consistency with other datasets used in this study. Similarly, individual regions discussed are limited to those which show the strongest signals in Section 3.3: Bering and Beaufort Seas, Canadian Archipelago, and Central Arctic (Figure 3.1).

Tropical SST anomalies are calculated for the East Pacific (EP) Niño3 index (-5° to 5°N, 210° to 270°E) and Central Pacific (CP) Niño4 index (-5° to 5° N, 160° to 210° E) regions, as defined by the Climate Prediction Center. These are area weighted anomalies within a given region and are derived from the ERSST v5 dataset extending from 1920 to 2017. The time series for both ENSO regions used in this study come from the Climate Variability Diagnostics Package (Phillips et al., 2014), which are available from the National Center for Atmospheric Research (NCAR). To provide a broader definition of ENSO events, if the average SST anomalies exceeds (falls below) the 75th (25th) percentile, they are considered Niño (Niña). Moreover, the ENSO indices will be specifically referred to as EP ENSO (Niño3/Niña3) and CP ENSO (Niño4/Niña4) in the text.

To gain an understanding of the atmospheric circulation during periods of high and low SST anomalies, composites are produced using daily 1° ERA5 reanalysis data for the period of January 1979 through December 2018 (Hersbach et al., 2020). Of particular interest in this paper are 500 hPa heights, 850 hPa winds, and integrated vapor transport (IVT), as these variables are closely connected to similar variables used in identifying high-latitude blocking and associated moisture transport, which have previously been shown to significantly impact sea ice (Yang and Magnusdottir, 2017; Yang and Magnusdottir, 2018). Moisture transport is commonly quantified

in high latitudes using IVT, which is calculated using u- and v-winds and specific humidity (q). We calculate daily IVT following Mattingly et al. (2018) for the 1000 to 200 hPa layer (dp), such that

$$IVT = \frac{1}{g}\int_{1000\ hPa}^{200\ hPa} qv\ dp \quad (1)$$

In this calculation, g is the gravitational constant (9.81 m s^{-2}) and v is the vector wind (calculated from u- and v-winds). Instead of raw IVT values, average IVT is composited with respect to a seasonal climatology to produce respective values of the percentage of IVT compared to a standard, which is useful in high-latitude regions with climatologically low temperatures and low moisture content, as used in Chapter 2.

3.2.2 CESM LE

The Community Earth Systems Model, version 1, Large Ensemble (CESM LE) (Kay et al., 2015) simulations are used to assess whether a tropical to polar teleconnection exists in a fully coupled model. This dataset contains 35 ensemble members originating from the same set of initial conditions for the period of 1920–2100 (1850–2100 for the first member). For this study, historical runs for 1920–2005 are used and concatenated with the years 2006–2017 from the RCP8.5 simulations to ensure a record of 1979–2017 to match observations, similar to the approach used by Yang and Magnusdottir (2018). This period also allows for the use of NCAR's Climate Variability Diagnostic Package calculations of the ENSO indices, including EP Niño3 and CP Niño4 indices for the period of 1920–2018. To account for differences in the mean climate state across ensembles, for each ensemble, seasons of high (low) SST anomalies are those which exceed (are below) the 75th (25th) percentile compared to that ensemble's climatology, similar to observational definition of Niño (Niña) events.

We acknowledge limitations by not examining IVT in the CESM LE dataset. Archived model runs available through the Climate Data Gateway at NCAR do not contain daily specific humidity and wind variables at enough pressure levels to make comparable estimates to ERA5. To address this limitation, we composite 850 hPa winds and specific humidity as a proxy for low-level moisture transport; as such, this method likely underestimates total Arctic moisture transport in CESM, and instead is used as a qualitative indication such as more or less moist conditions under different SST regimes.

3.2.3 Statistical Analyses

Both observational and modeled monthly SIC/sea ice fraction and SST anomalies are detrended using a second-degree polynomial for the period of 1920–2017 prior to correlation analyses. Unless otherwise noted, correlations for both observations and CESM LE output are for the period of 1979–2017. Correlation analysis is conducted with the Pearson correlation. Unless noted otherwise, statistical significance is denoted at 90%. Likewise, atmospheric composites and sea ice anomalies are with respect to the 1981–2010 seasonal or monthly mean. Seasonal sea ice concentration (3-month mean) is further lagged by one or more months to consider delayed sea ice responses to SST anomalies.

To further quantify the impact of ENSO types on sea ice, a principal component analysis (PCA) was conducted on seasonal sea ice concentration anomalies for the different regions. Prior to conducting the PCA, the regional seasonal sea ice concentration anomalies are weighted by the cosine of the latitude and are standardized. The final EOF scores are further detrended prior to correlating with SST time series through the Pearson correlation.

3.3 Sea Ice Response to ENSO

3.3.1 Observed Links

Lagged correlations between winter (JFM) regional ENSO indices and SIC suggest varying regional responses to the location of the SST anomalies (Figure 3.2). Overall, JFM SST anomalies generally do not correlate to JFM SIC, except for some significant correlations to the north of the Canadian Archipelago for EP (Figure 3.2a) and in the southern portion of the Bering Sea for CP (Figure 3.2b). The SIC in these two regions shows stronger, more spatially consistent correlations to JFM SST anomalies approximately one month later (Figures 3.2c,d). At 2 months following the JFM SST anomalies, MAM SIC is negatively correlated to SSTs in the Beaufort Sea for the EP region more so than for the CP region (Figures 3.2e,f). These negative correlations, although strongest for the EP anomalies, coincide with the outer edge of the sea ice extent, suggesting the positive tropical Pacific SSTs in the winter may still contribute to springtime sea ice extent. This is most prominent by AMJ (3 months after JFM SST anomalies) (Figures 3.2g,h), as the strong negative correlations (less than -0.4) are in the Beaufort Sea and in the Canadian Archipelago, primarily for the EP anomalies. While both ENSO indices show negative correlations in the parts of the Bering Sea, the maps presented in Figure 3.2 suggest that EP SST anomalies may be most impactful in springtime sea ice extent near the North American continent, particularly in the Beaufort Sea and the area containing the Canadian Archipelago.

To assess whether the Beaufort Sea and Canadian Archipelago regions show a statistical signal to EP and CP ENSO, lagged time series of sea ice area are shown and correlated to the JFM SST anomalies (Figure 3.3). Despite parts of the Beaufort Sea region indicating a significant correlation from the map for CP, the statistical response in regional sea ice from SST anomalies is most sensitive to JFM SST anomalies in the EP region, particularly from MAM

onward, with $p < 0.10$. (Figure 3.3). Similarly, the Canadian Archipelago displays strongest sensitivity in sea ice area to tropical Pacific SST anomalies when they originate from the EP region from about late spring to summer (April-July, Figure 3.3). This response is not readily apparent for the CP anomalies, despite both ENSO regions indicating a negative correlation in sea ice. Both the Beaufort Sea and Canadian Archipelago regions have less springtime, and possibly early summer, sea ice under positive tropical SST anomalies consistent with El Niño; in particular, sea ice in these regions is likely most impacted by the SST anomalies originating from the Niño3 region.

Figure 3.4 shows the correlation coefficients of JJA SST anomalies and lagged SIC. When considering no lag (i.e., JJA SIC), positive correlations between SIC and SSTs for the Niño4 index exist near the Beaufort Sea into the Canadian Archipelago regions, extending into the Central Arctic, while these positive correlations are limited to the Canadian Archipelago for the Niño3 SSTs anomalies (Figure 3.4a,b). SIC from July–December is positively correlated (correlations exceeding 0.4) to the CP index in the Canadian Archipelago region compared to the EP SST anomalies (Figure 3.5). In fact, results from a PCA of JJA ENSO does indicate some influence on Canadian Archipelago SIC. The second EOF (which explains 15-18% of the seasonal SIC variability) is indeed correlated to the CP-ENSO from July-November (Table 3.1). This is consistent with Hu et al. (2016), who showed that a CP-type of El Niño will inhibit summer Arctic warming and reduce sea ice loss in this region.

Additionally, the prominent positive correlations (exceeding 0.3) in the Central Arctic are prevalent for both ENSO indices, particularly for June–October (Figure 3.5). However, these significant correlations persist longer into the autumn and early winter (October-November) for CP, though are not evident in the results of the PCA. This suggests that historically, mechanisms

associated with ENSO diversity have the strongest impact on Arctic sea ice in summer, leading us to question whether these observed associations exist in GCM simulations.

3.3.2 Representation in CESM LE

For the 1979–2017 period, the CESM LE indicates spatially consistent significant correlations between JFM SSTs and SIC throughout most of the Arctic (Figure 3.6), with these correlations becoming stronger by MAM. This pattern results in mostly negative correlations roughly between -180° to 0° longitude, with positive correlations from 0° to 180° longitude. Visually there is little difference between ENSO type and SIC correlations, except for the Bering Sea near the Aleutian Islands, where the CP index is negatively correlated to SIC in the observations (from Figure 3.2) and the correlations in this region in CESM are slightly stronger for the EP index compared to EP. In general, even with SIC lagged, there is little difference between the JFM EP and CP correlations (Figure 3.6). The direction of these correlations to SIC does qualitatively better match those of observations after 3 months (i.e., AMJJ SIC) in many regions, even when the sea ice 0 to 2 months lagged does not appear to directly match the spatial pattern from Figure 3.2. When taken together, observations and simulations suggest that the modeled springtime Arctic sea ice growth may be delayed due to a possible under-representation of atmospheric processes associated with ENSO more generally, which may lead to sea ice changes and the consequent discrepancies in the modeled spatial variability as exhibited by the observations. This is particularly evident when regional correlations from the simulations, similar to those previously done with the observations, do not yield significant ENSO-SIC signals for the Beaufort Sea and Canadian Archipelago regions (not shown).

The maps of the correlation coefficients between SIC and SSTs from CESM LE best match observations for the CP index when considering the JJA SST anomalies, though suggest

an overall weaker ENSO-SIC signal during the warmer seasons (Figure 3.7). However, in this scenario for no lag in sea ice, positive correlations exist in the Central Arctic, with negative correlations in the North Pacific along the boundary of the sea ice for both ENSO indices. The negative correlations exhibited in the Beaufort Sea are consistently weak and opposite in sign compared to the observed positive correlations. Moreover, modeled lagged sea ice with a positive correlation in the Central Arctic diminishing completely within one month. When considering specific regions more carefully, the negative correlations from the simulations in the Beaufort Sea are no longer confirmed for either ENSO type. The positive correlation in the Central Arctic as a whole in summer, which was prominent in observations, is also not a statistically significant signal in CESM. Moreover, when assessing the most prominent and relatively consistent ENSO-SIC relationship in the Canadian Archipelago region from observations the significant correlations observed in the Canadian Archipelago are not further confirmed in CESM via PCA (Appendix A, Figure A1). It is further evident that the observed ENSO-SIC signals and how these signals vary based on ENSO type is not well-captured within CESM LENS.

3.4 Atmospheric Drivers of Sea Ice Response

To explain the lagged correlations observed between SIC and SSTs in JFM, atmospheric circulation, wind, and moisture transport anomalies are shown for JFM in Figure 3.8. Seasons with SST anomalies exceeding the 75th percentile represent warm events (i.e., “Niño”) and seasons below the 25th percentile represent cold events (i.e., “Niña”) for compositing and are shown in Appendix A, Figure A2.

Atmospheric circulation under both ENSO types during winter differ in that a strong upper-level ridge placed over the Gulf of Alaska with a strong low positioned over the Canadian Archipelago enhances moisture transport out of (into) the Arctic in the Beaufort Sea (Canadian Archipelago) under Niño4 conditions (Figure 3.8). Similar conditions persist for 1-2 months, with some eastward propagation (Appendix A, Figure A3). For Niña4, composites indicate an anomalous low over the Bering Sea with below normal moisture transport there and over the Canadian Archipelago when compared to Niña3 (Figure 3.8), which persists through MAM (Appendix A, Figure A4). The slowdown in winter sea ice growth following these circulation anomalies in JFM may explain why sea ice anomalies are not immediately affected in these regions. While not explored directly here, previous research has shown, that the circulation anomalies may inhibit sea ice growth due to enhanced lower-latitude moisture transport increasing downwelling longwave radiation (Woods et al. 2013; Park et al. 2015; Mortin et al. 2016; Hegyi and Taylor, 2017). Similar mechanisms may be driving the positive correlations at 1-2 months lag for Niño4, in the Bering Sea despite the lack of an overall regional signal (see Section 3.3). The upper-level low during Niño4 is positioned over the Canadian Archipelago and remains through MAM (Appendix A, Figure A3). To the north of this upper-level low, there is stronger northerly low-level winds (and less moisture) positioned in the area where the strong negative SIC correlations appear 1-3 months later under the Niño3 conditions. Johansson et al. (2017) show that winter cloud cover from moisture intrusions may impede spring sea ice recovery, so it is possible that regions experiencing less moist conditions in winter may be conducive to sea ice growth. The stronger correlations exist for the Niño3 than the Niño4 possibly due to the stronger upper-level low that is positioned further north than under Niño4 conditions from JFM through MAM. Therefore, it is reasonable to assume that more sea ice

export may be occurring in the Canadian Archipelago during Niño3. Despite the low-level wind patterns during La Niña seasons, there is still anomalously high moisture transport occurring in and around the Canadian Archipelago for Niña3, which, in combination with cloud cover, may act to prohibit sea ice growth during this region over time. Interestingly, in the Beaufort Sea region, these circulation patterns suggest relatively moister (drier) conditions during Niño4 (Niña4) events, though it is possible that the lower-level winds associated with these may promote more growth or sea ice import into the region when compared to the EP ENSO.

While not a direct comparison to the observations, composites of the CESM ensemble members during different ENSO seasons are used to show general circulation and moisture patterns occurring in the Arctic to gain a better understanding of the model's atmospheric phenomena coinciding with possible SST-sea ice linkages. The general CESM 850 hPa flow pattern overlain with specific humidity highlights similar regions exhibiting moisture advection into and out of the Arctic, particularly for the Niño4 (Figure 3.9, Appendix A, Figure A5-6). The composite of the 500 hPa height difference for Niño4 and Niño3 in CESM indicate a low over eastern North America and the Canadian Archipelago with a ridge-like pattern in the North Pacific for the Niño4. Similarly, the Niña4 seasons exhibit similar circulation anomalies as the observations. However, the strength of the moisture and circulation anomalies are substantially weaker in CESM than observations, which may impact how heat and moisture are transported into the Arctic and coincident cloud cover in the model. Inaccurate representation of heat and moisture transport is likely to misrepresent the surface energy balance associated with sea ice growth and melt processes in JFM. The underestimation of the circulation anomalies would underestimate the impact on sea ice through decreased moisture transport. Because the positioning of winter anticyclonic anomalies deflects cyclones and moisture transport (Yang and

Magnusdottir, 2017; Papritz and Dunn-Sigouin, 2020), and cloud cover from moisture intrusions play an integral role in springtime sea ice processes (Kapsch et al., 2013; Park et al., 2015a; Mortin et al., 2016), the lack of physical representation of these anticyclonic features within CESM may underestimate moisture transport leading to biases in sea ice growth (Woods et al., 2017).

Summer months generally exhibit weaker atmospheric ENSO signals compared to the winter (Figure 3.10). Moisture transport is enhanced by 20% or greater compared to normal in the North Atlantic and northern portion of the Canadian Archipelago under Niño4 conditions compared to Niño3 conditions. These atmospheric responses are visibly similar up to 2 months later (Appendix A, Figure A7), with minor variation in the placement of high/lows. Similarly, above-normal moisture transport occurs in northwestern and coastal Greenland and Barents-Kara seas under Niña4 conditions compared to Niña3, due to the placement of an upper-level ridge over the region (Figure 3.10, Appendix A, Figure A8). Given the northerly 850 hPa winds around the Canadian Archipelago region, under the Niño4/Niña4 conditions it is possible that the positive correlations exhibited between the sea ice and Niño4 SST anomalies are related to circulation patterns conducive to either ice import into the region or is the lagged result of lack of sea ice loss under JFM Niño4/Niña4 conditions.

Figure 3.11 shows the CESM atmospheric response to JJA ENSO variability. Under El Niño conditions, there is little difference between El Niño types regarding 850 hPa specific humidity. However, some variation in upper-level atmospheric circulation is evident, though there are generally weak highs over the Central Arctic and North Atlantic under Niño4 conditions. A symmetric circulation response exists under La Niña conditions, as both regions exhibit lower heights under Niña4 conditions compared to Niña3. Similarly, more moist (dry)

conditions also persist over the North Atlantic 1 to 2 months out under Niño4 (Niña4) conditions (SI 9, 10). Increased longwave radiation from cloud cover associated with enhanced moisture transport in winter can produce anonymously low sea ice cover the subsequent summer (Kapsch et al., 2013; Park et al., 2015a; Park et al., 2015b; Kapsch et al., 2016; Mortin et al., 2016). Given that stationary anticyclones themselves are effective at reducing summer sea ice (Wernli and Papritz, 2018), how these features are represented in models, such as CESM, may affect how sea ice is represented. Future investigation should seek to quantify how much winter and spring moisture and heat transport and radiative impacts from these influence summer and autumn sea ice loss both observationally and within models.

The lack of diversity in ENSO conditions and its Arctic response in CESM is somewhat expected. Deser et al. (2017) report that after running CESM1 pacemaker simulations, the extratropical boreal winter atmospheric response to ENSO shows considerable uncertainty due to internal variability. In addition to examining ENSO diversity within the experiment, CESM fails to account for the variability seen in the spread of simulations of sea level pressure. The results presented in this paper corroborate these findings, arguing for improvements on extratropical-tropical teleconnection representation in CESM. (Fasullo et al., 2020) show that over time, the CMIP archive has improved ENSO representation, though suggest that quantifying modeled ENSO impacts remains to be explored. For example, Gettleman et al. (2019) show significant improvements in clouds and related feedbacks in CESM version 2 from CESM version 1. Related, documented changes in Arctic liquid clouds, related precipitation, and surface energy fluxes in CESM2 may better simulate the sea ice-atmosphere interface and have implications on sea ice (DuVivier et al., 2020; McIlhatten et al. 2020). Considering the positive correlations within the Central Arctic do not vary much between the ENSO type, it is plausible that remote

influences (such as those from the tropics) play a role in inhibiting summer sea ice melt particularly in regions near the Beaufort Sea due to cloud cover, analogous to anomalously low summer 2007 sea ice season forced by winter cloud cover (Letterly et al., 2016). These enhancements, in combination with improved representation of ENSO in CESM2 (e.g., Capotondi et al., 2020b), are promising for quantification of tropical-extratropical teleconnections going forward. For this reason, ENSO influence on Arctic seasonal cloud cover should be further explored both observationally and in climate models as Arctic cloud cover is a large driver of sea ice change.

3.5 Summary and Conclusion

Sea ice loss in recent decades has contributed to rapid warming within the Arctic climate system. While physical feedbacks control much of this warming, remote factors including those from ENSO can influence sea ice loss, which have not been fully explored within climate models. Broadly, using lagged compositing, we discern seasonal and regional signals in sea ice due to tropical SST variability within the ENSO region within the Arctic and identify possible atmospheric drivers. We further demonstrate a lack of tropical-extratropical teleconnections in CESM LE. In particular, we show:

1. There are observed seasonal and regional differences in how SST anomalies associated with ENSO manifest themselves within the Arctic, particularly in the Canadian Archipelago region. There exists a lag in winter/spring Arctic sea ice response in the Beaufort Sea and Archipelago regions by about 1 to 3 months after the SSTs anomalies are present. During summer, there is little temporal lag between summer SST anomalies and sea ice responses in the Canadian Archipelago and Central Arctic regions, but sea ice

responses can persist for 1 to 4 months, or longer, depending on ENSO type. We further confirm summertime sea ice responses to CP ENSO are strongest in the Canadian Archipelago region.

2. Shifts in Arctic atmospheric circulation as a result of CP and EP may explain observed lagged sea ice responses. In particular, during the winter, there is a northward shift in the upper-level low near the Canadian Archipelago during EP Niño may aid in increased sea ice export. Under CP Niño/Niña conditions, the Canadian Archipelago region undergoes more moisture transport within the region, though experiences less sea ice loss, as confirmed by previous studies. It is possible that the lack of winter sea ice loss signal for CP ENSO allows the ice to persist longer into the summer months, thus inhibiting summer sea ice loss in this region.
3. The observed tropic-to-Arctic teleconnection explored in this study is not evident in the CESM LE. More specifically, CESM LE shows some connection with 0-1 months lag in winter, and there is little difference in ENSO diversity although more spatial variability in sea ice response occurs during summer under different ENSO conditions than in the winter. We are further unable to confirm strong observed regional signals, even those in the Canadian Archipelago during summer, through our analyses. Furthermore, examining the upper-level circulation patterns reveal weaker upper-level circulation regimes overall compared to observations for both seasons suggesting that the physical processes associated with tropical-to-polar teleconnections and improving their representation in climate models should be a central focus of further research.

The results presented here show evidence of ENSO's variability in influencing seasonal sea ice in the Arctic. Given uncertainty around how ENSO may manifest in future climates,

understanding possible connections to the Arctic provide insight in discerning the drivers of seasonal sea ice loss. Moreover, these results should motivate the climate modeling community to understand and improve interannual climate variability and associated teleconnection representation in models going forward.

Table 3.1. Canadian Archipelago top 4 EOFs and correlations for June-November SIC and JJA ENSO-related SST anomalies. Explained variance is expressed as %. Correlations where p < 0.10 are bolded.

			JJA			
			Nino3		Nino4	
		Explained Variance	S	P	S	P
JJA	EOF 1	61.1	-0.1031	0.5322	-0.0711	0.6672
	EOF 2	14.7	0.1048	0.5255	0.1942	0.2362
	EOF 3	7.1	-0.1640	0.3185	-0.0474	0.7743
	EOF 4	**3.7**	0.2022	0.2169	**0.2999**	**0.0636**
JAS	EOF 1	45.2	-0.0824	0.6181	-0.0317	0.8483
	EOF 2	**17.3**	-0.0615	0.7098	**-0.3476**	**0.0301**
	EOF 3	9.2	-0.1071	0.5162	0.1139	0.4901
	EOF 4	**6.7**	**-0.2742**	**0.0912**	**-0.3582**	**0.0252**
ASO	EOF 1	43.0	-0.0500	0.7623	0.0320	0.8465
	EOF 2	**15.9**	0.1046	0.5262	**0.3865**	**0.0151**
	EOF 3	8.8	-0.1355	0.4108	0.1129	0.4937
	EOF 4	6.1	0.2286	0.1616	0.2080	0.2039
SON	EOF 1	46.7	0.0148	0.9286	0.0772	0.6404
	EOF 2	**14.0**	-0.1256	0.4461	**-0.4452**	**0.0045**
	EOF 3	8.6	0.1028	0.5334	-0.1710	0.2979
	EOF 4	6.3	0.1431	0.3847	0.0283	0.8640

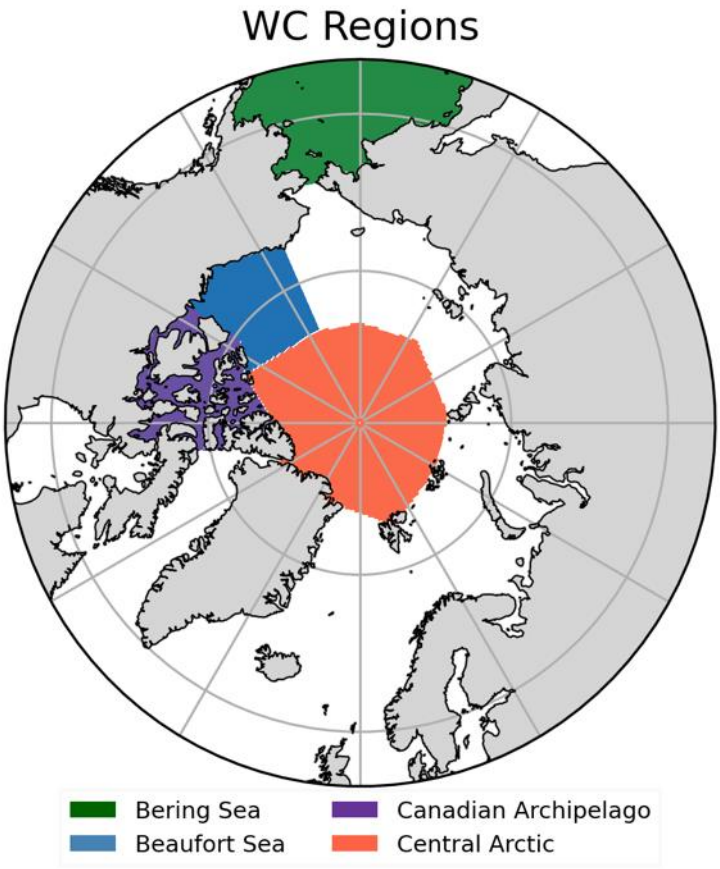

Figure 3.1. Different regions exhibiting the strongest sea ice-ENSO signals, based on those as defined by Walsh et al. (2019).

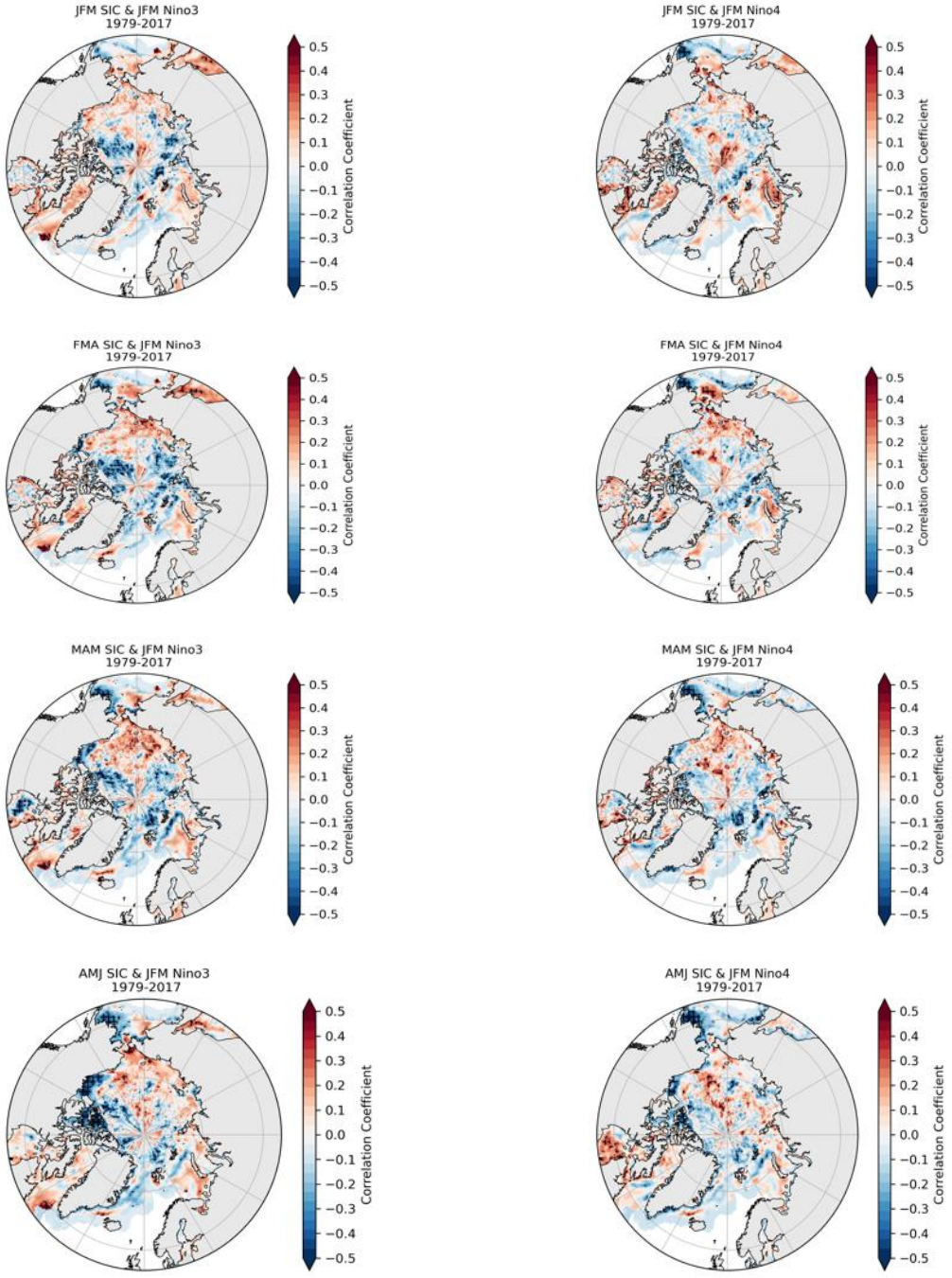

Figure 3.2. Correlation coefficient of JFM SST anomalies for EP (Niño3, left) and CP (Niño4, right) regions with seasonally lagged sea ice concentration of +0 months (JFM SIC, top row) to +3 months (AMJ SIC, bottom row). Significant correlations at 90% are indicated by cross-hatching.

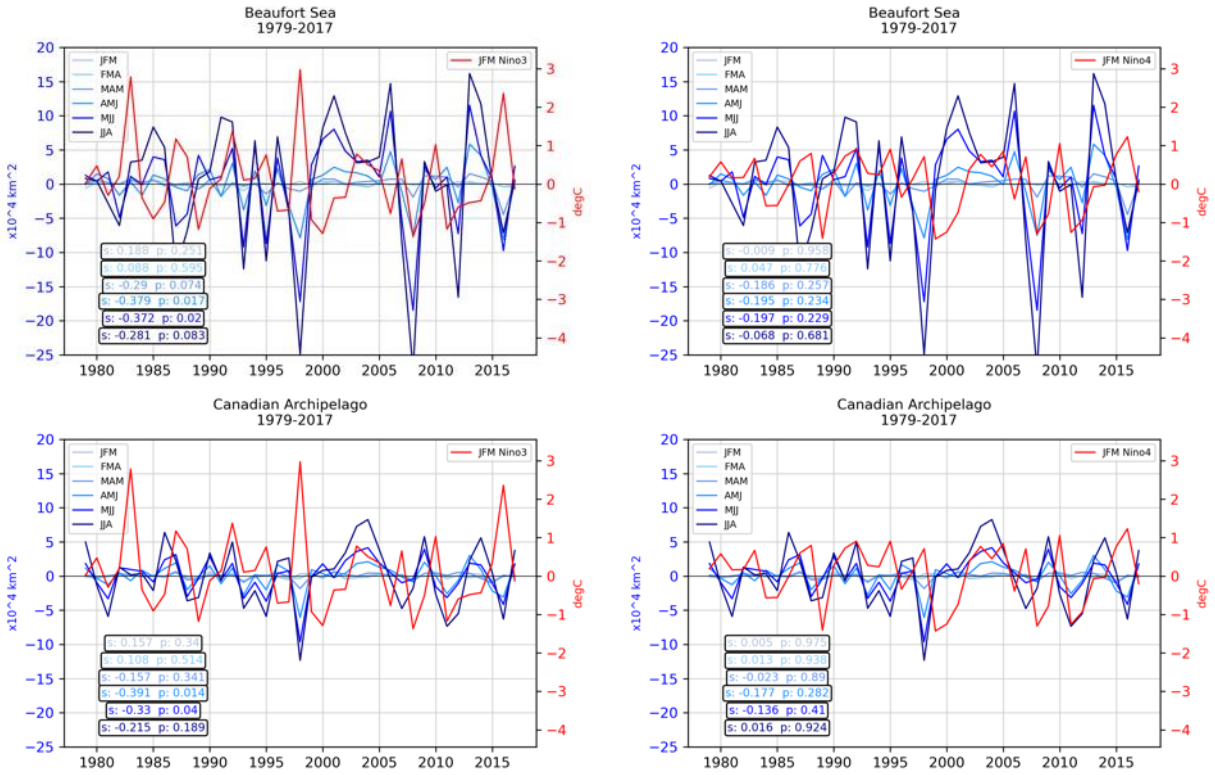

Figure 3.3. Detrended seasonal sea ice area from Walsh et al. (2019) and 3-month average detrended Niño3 (left)/ Niño4 (right) time series for the Beaufort Sea (top) and Canadian Archipelago (bottom). Pearson correlation (s) for JFM SSTs and 3-month average sea ice area and p-value (p) shown.

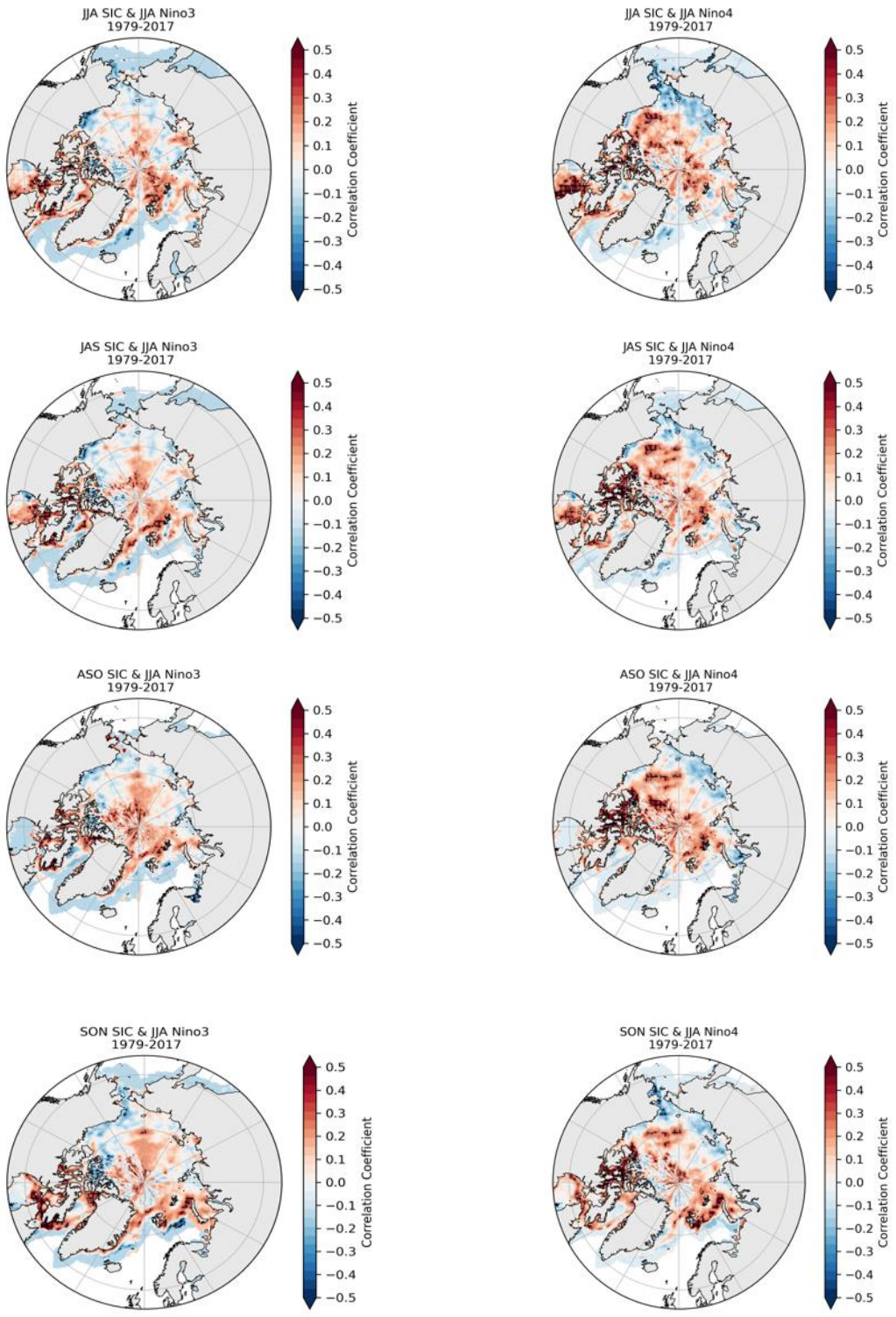

Figure 3.4. Same as Figure 3.1, but for JJA SSTs, starting with JJA SIC.

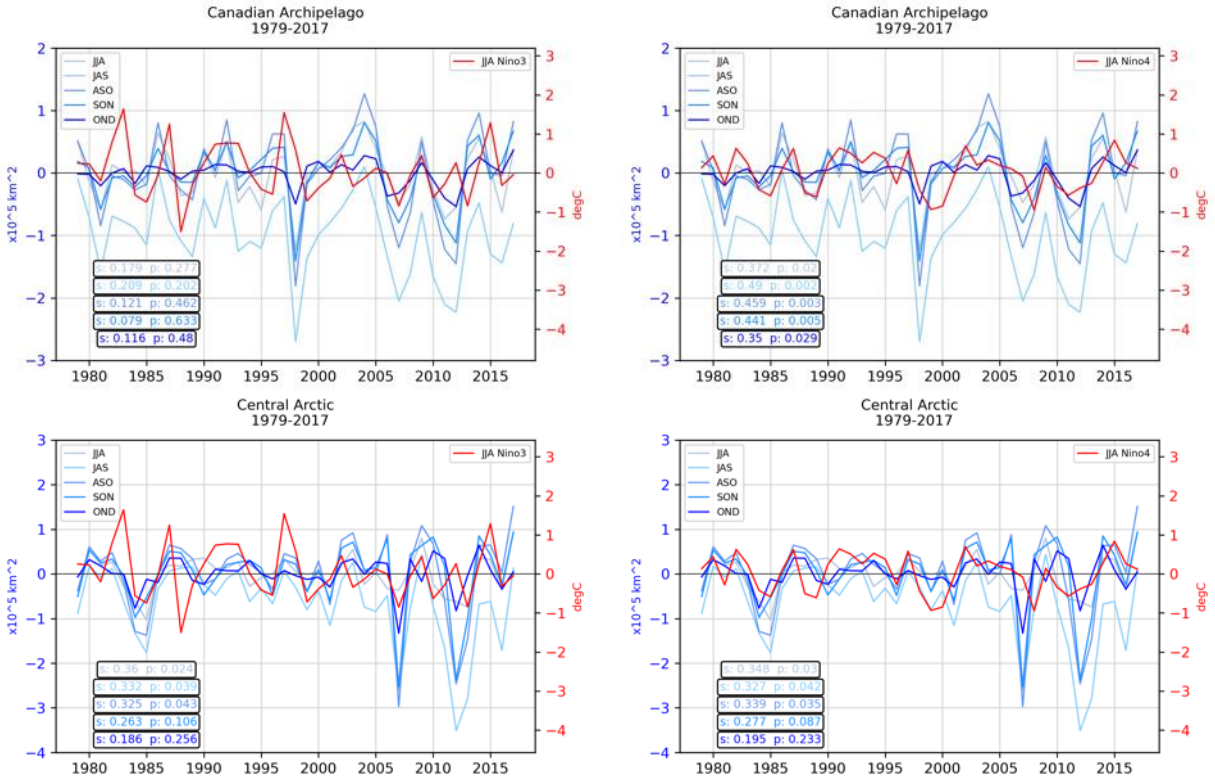

Figure 3.5. Same as Figure 3.3, but for JJA SSTs and starting with JJA sea ice areas in the Canadian Archipelago (top) and Central Arctic (bottom).

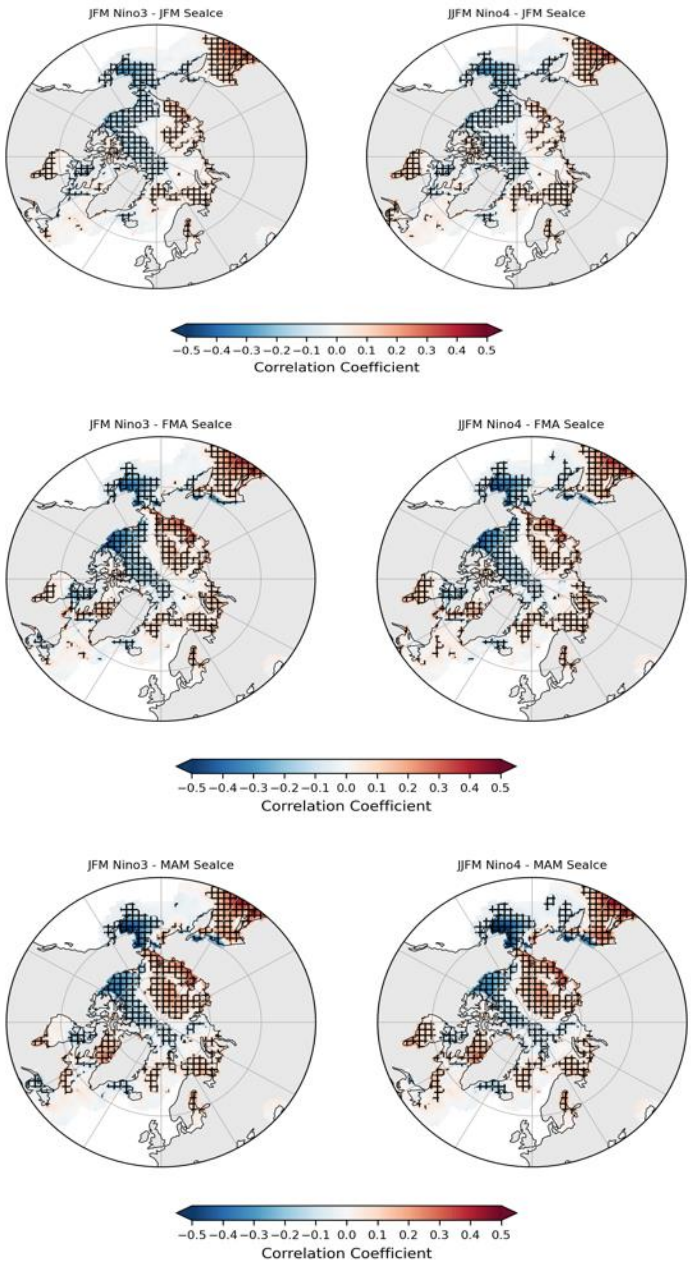

Figure 3.6. Pearson correlation between all 35 ensemble members for JFM Niño3 (left)/Niño4 (right) and lagged seasonal average sea ice fraction time series from 1979-2017. Cross-hatching indicates statistical significance when $p < 0.1$.

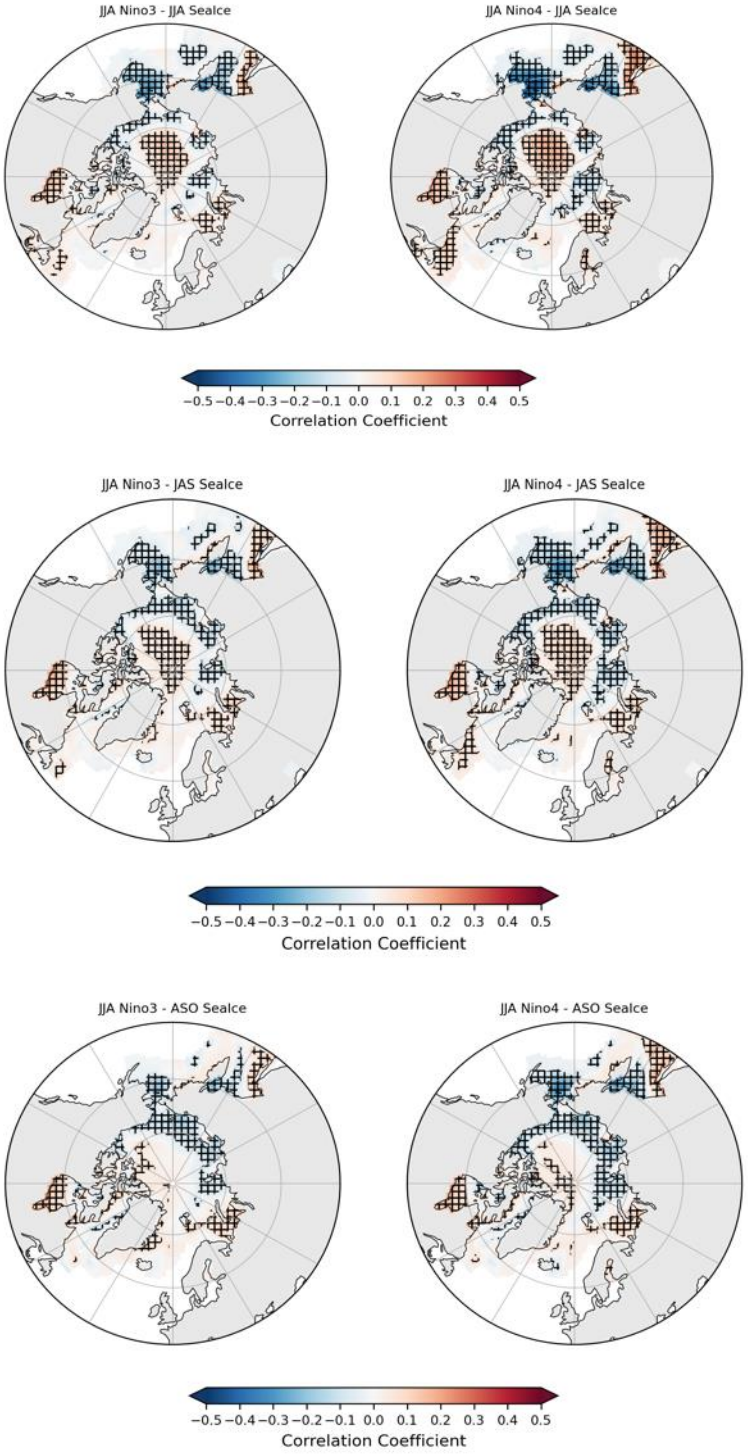

Figure 3.7. Same as Figure 3.6, but for JJA SSTs.

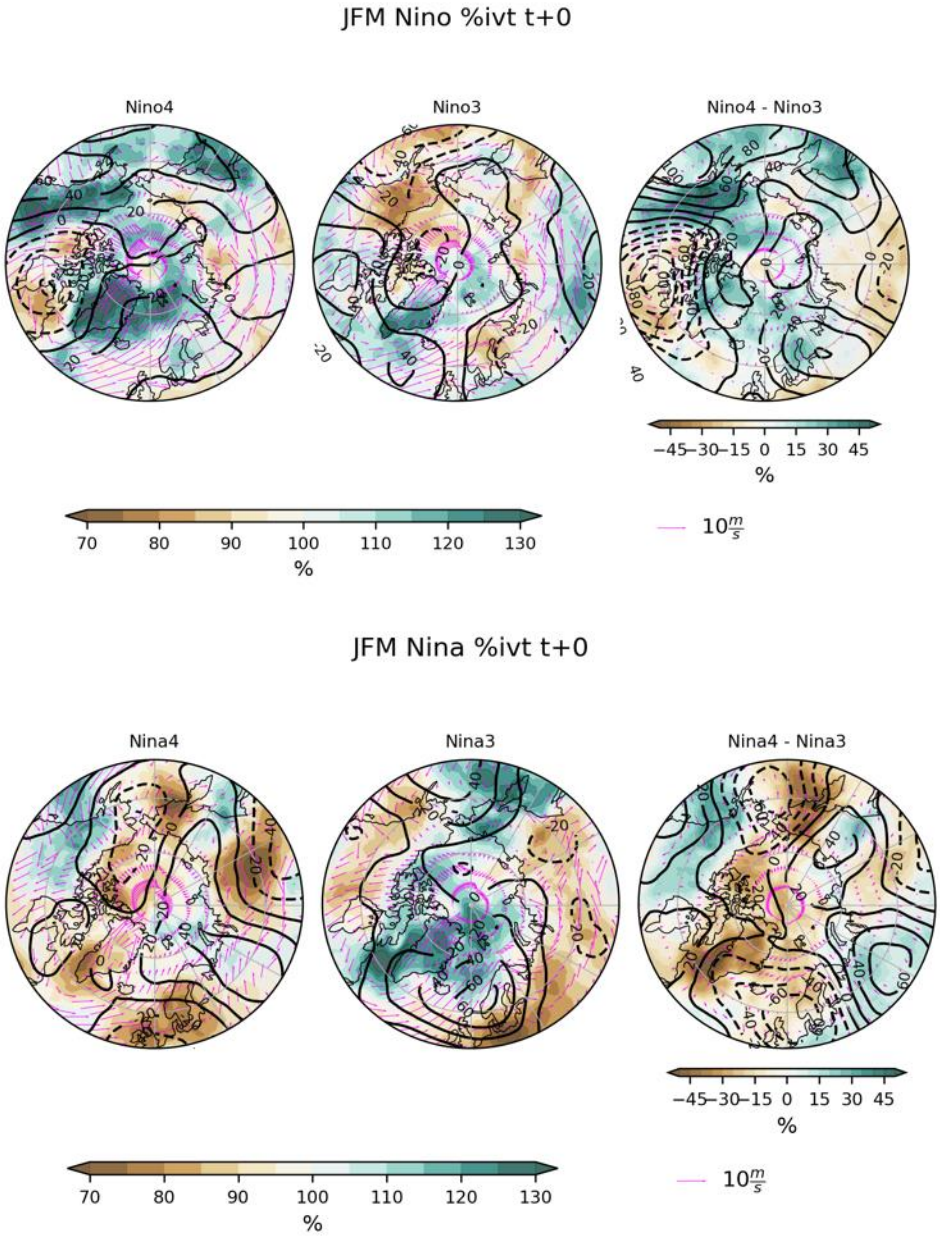

Figure 3.8. Composites of the JFM 500 hPa height anomalies (black contours), integrated vapor transport (IVT) expressed as a % of the seasonal mean (filled), and 850 hPa seasonal mean wind (magenta) for Niño (top) and Niña (bottom) seasons.

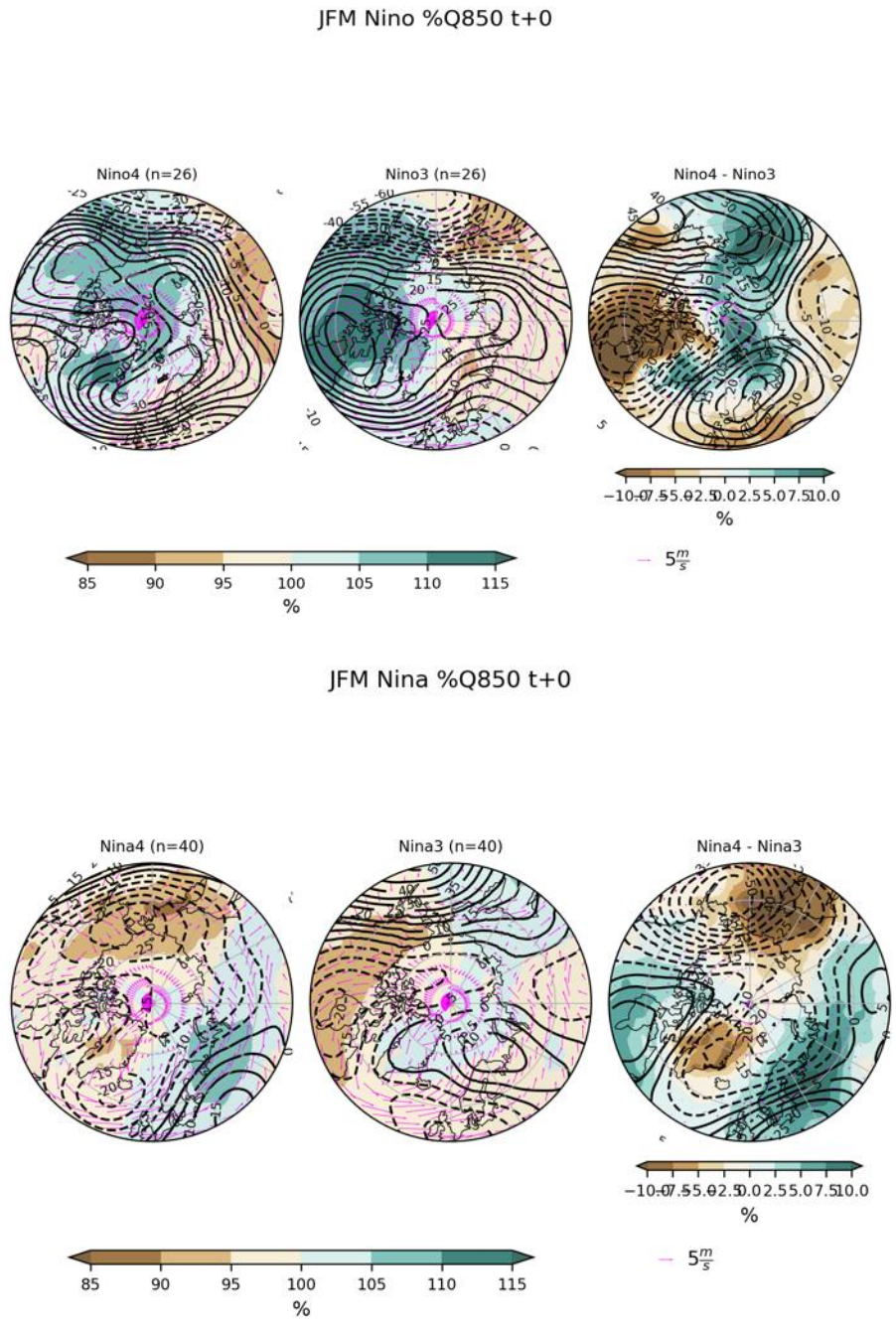

Figure 3.9. Similar to Figure 3.8, except for seasons within each ensemble member with JFM SST anomalies. Note that 850 hPa specific humidity is the filled quantity and is expressed as a percent of the seasonal mean. Contour interval for 500 hPa heights at 5m intervals.

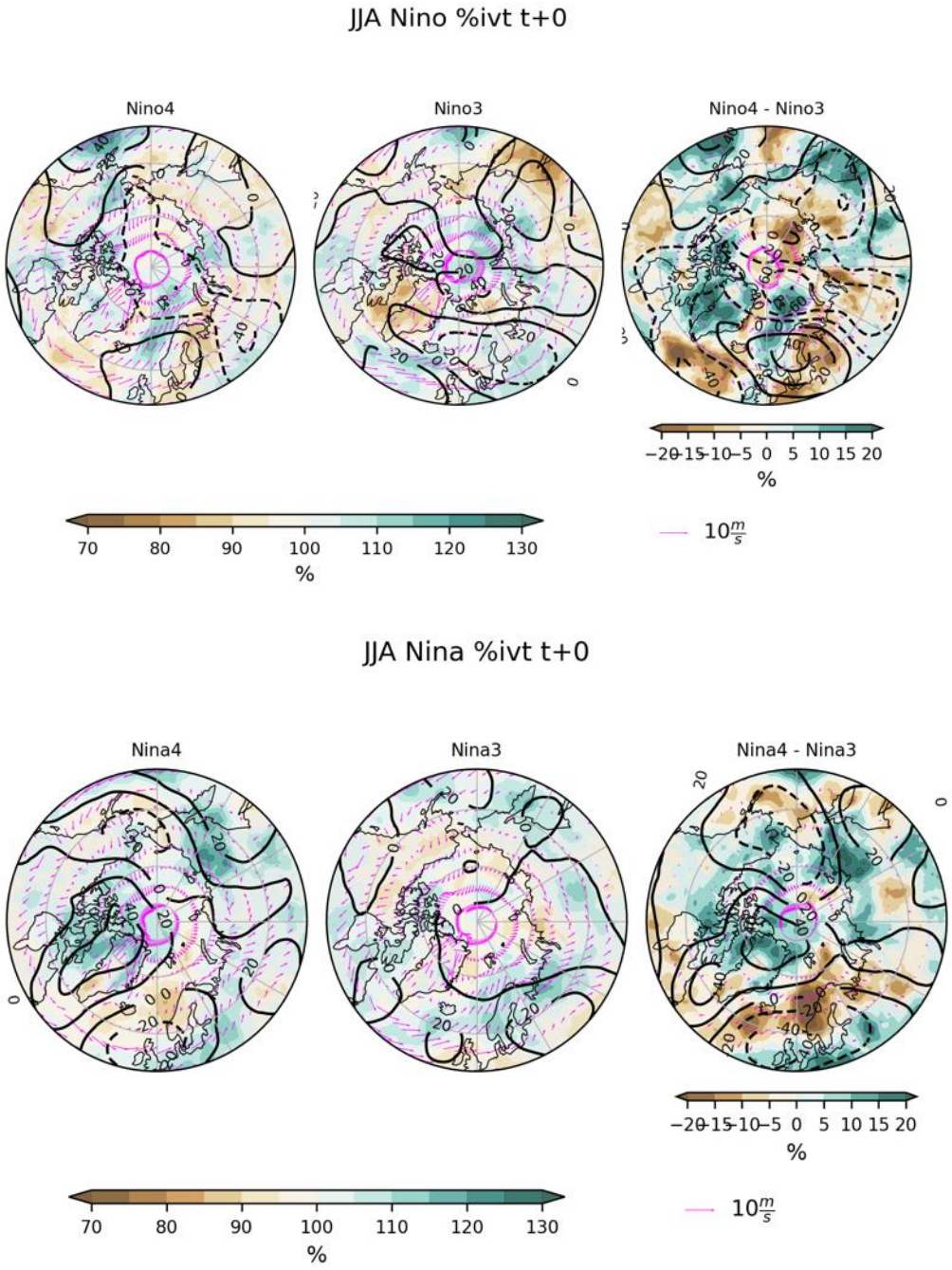

Figure 3.10. Same as Figure 3.8, but for JJA SST anomalies.

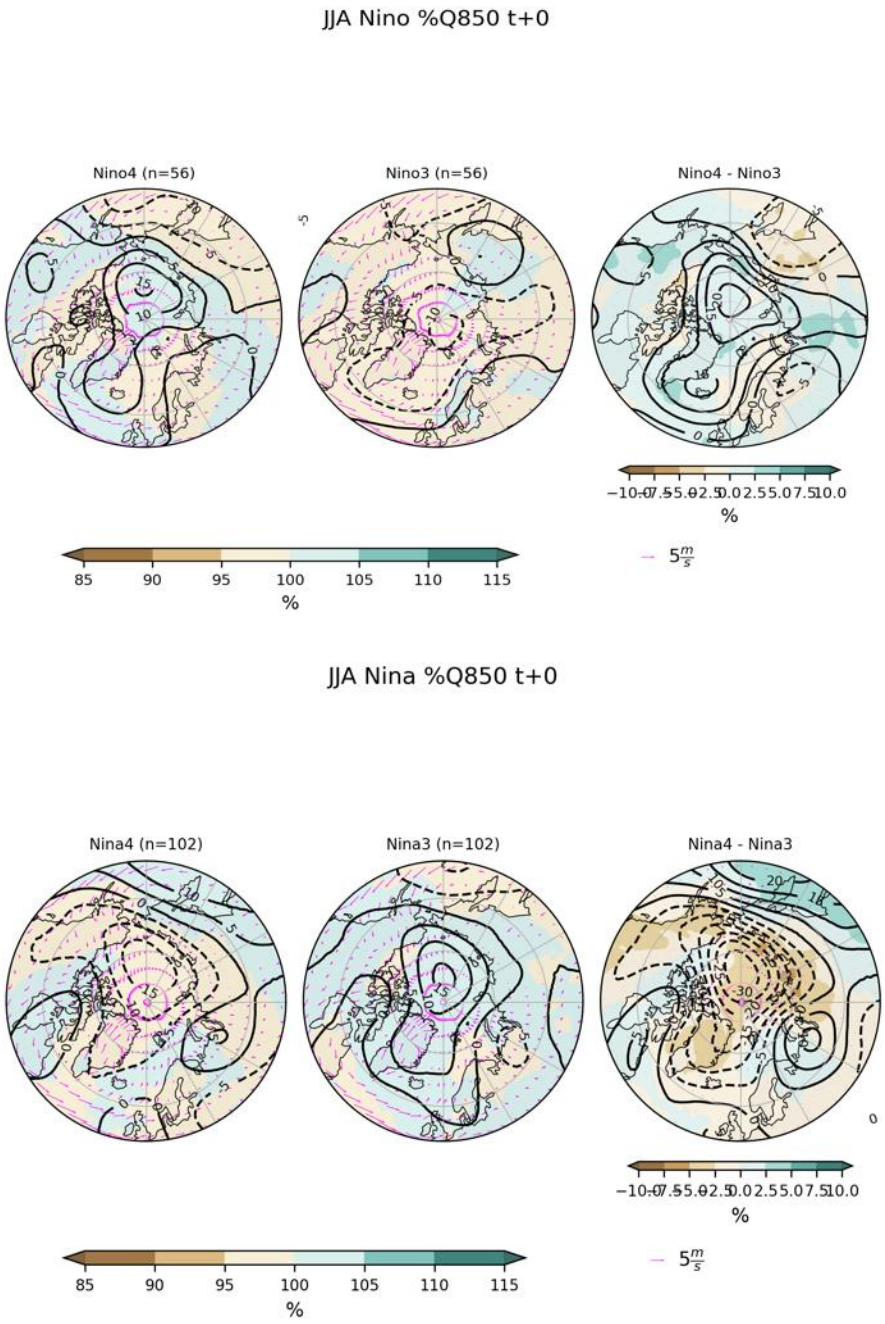

Figure 3.11. Same as Figure 3.9, but for JJA SST anomalies.

CHAPTER 4

UNDERSTANDING BLOCKING IMPACTS ON CURRENT AND PROJECTED SEA ICE IN CESM LENS[3]

[3] Wachowicz, L.J. and T.L. Mote. To be submitted to *Journal of Geophysical Research: Atmospheres*

Abstract

Blocking anticyclones significantly alter the surface mass and energy budgets of the Arctic by advecting warm, moist air and leading to sea ice loss. Representation of high latitude blocking is not well documented in climate models, leading to uncertainties in quantifying cumulative effects of blocking on sea ice. Furthermore, this increases uncertainty behind future projections of blocking impacts on the cryosphere and the relative contribution of these systems in accelerating ice loss. This study assesses high latitude blocking in a global climate model ensemble, Community Earth Systems Model Large Ensemble (CESM LENS) both historical (1979-2005) and projected (2081-2100) blocking to discern how blocking impacts on sea ice may change over time. We show that a dynamic-based blocking index has a realistic historical blocking climatology in CESM LENS, a projected increase (decrease) in JJA (DJF and MAM) blocking days in the North Atlantic, and a projected increase (decrease) in JJA and MAM (DJF) blocking days in the North Pacific. A novel contribution of this study shows that changes in the number of blocking days are largely driven by changes in the persistence of these systems. CESM LENS appears to best simulate the blocking-sea ice relationship in MAM in both ocean basins, as the atmospheric conditions associated with blocking are most realistic. CESM reasonably represents a prevalent JJA North Atlantic blocking and sea ice relationship, though is substantially underestimated in Baffin Bay. Furthermore, projections of the MAM blocking-sea ice relationship suggest blocking events may play a more critical role in future sea ice growth.

4.1 Introduction

Anticyclones play a pivotal role in the Arctic climate system by advecting heat and moisture into the Arctic, which is linked to sea ice decline (Woods et al., 2013; Woods and

Caballero, 2016; Kim and Kim, 2017; Yang and Magnusdottir, 2017). Stationary anticyclones, known as blocking anticyclones, further enhance heat, moisture, and radiative fluxes, leading to immediate sea ice impacts (Henderson et al., 2021). Blocking events have long been underestimated in global climate models (GCMs) throughout the climate model era (Davini and D'Andrea, 2016; Woollings et al., 2018b; Davini and D'Andrea, 2020), with even more attention brought to the importance of the underestimation of Greenland blocking, in particular (e.g., Hanna et al., 2018a). The inability to accurately assess blocking and its Arctic impacts within GCMs has several implications for ice sheet surface mass and energy budgets (Belleflamme et al., 2013; Fettweis et al., 2013) and regional sea ice concentration and extent (Smith et al., 2018). Therefore, obtaining accurate estimations of changes in blocking as well as understanding the physical implications of blocking-related contributions to sea ice loss remains challenging.

Blocking events account for more than 60% of extreme moisture injections into the Arctic (Yang and Magnusdottir, 2017). Diabatic heating from injections of warm, moist airstreams can amplify upper-level ridges through ascent and latent heating, particularly over the North Atlantic, leading to more extreme ridging and forming anticyclones (Zhang and Wang, 2018), especially combined with strong negative potential vorticity anomalies aloft (Wernli and Papritz, 2018). The amplification of these ridges can reinforce extreme blocking due to the displacement of the jet stream (Tachibana et al., 2019). Consequently, the role of low-level transient heat fluxes embedded within Rossby waves can reinforce persistent climatological patterns, like the North Atlantic Oscillation, and related regional surface weather (Masato et al., 2012; Swenson and Straus, 2017).

The decline in September sea ice is thought to be attributed to stronger anticyclonic circulation patterns over Greenland and related increases in warmer, more moist conditions in the

Arctic (Kapsch et al., 2013; Ding et al., 2014; Ding et al., 2017). Strong anticyclonic circulation anomalies, such as those associated with blocking over Greenland, increase sea ice export out of the Greenland Sea, thus contributing to September sea ice decline (Kwok, 2009; Kapsch et al., 2013; Smedsrud et al., 2016). Arctic anticyclones increase incoming shortwave radiative fluxes, and reduced cloudiness and adiabatic warming contribute to melting of the sea ice (Wernli and Papritz, 2018; Papritz, 2020). For example, a blocking pattern in the Arctic may result in positive surface skin temperature anomalies under clear sky conditions of more than 5K in spring and as much as 2K in summer (Johansson et al., 2017). Model sensitivity experiments suggest downwelling shortwave radiation anomalies play a much more limited role on summer sea ice, when compared to positive downwelling longwave radiative anomalies associated with cloud cover (Kapsch et al., 2016). As such, spring negative water vapor anomalies and clear sky conditions, such as those associated with anticyclones, result in late melt onset and below normal air temperatures occur about a month prior to melt onset (Woods and Caballero, 2016). Alternatively, earlier melt onset is characterized by an increase of moisture transport convergence due to stronger circulation anomalies before and at onset (Mortin et al., 2016).

Blocking representation in climate models has consistently improved with each iteration of the Coupled Model Intercomparison Projects, from phase 3 (CMIP3) to phase 6 (CMIP6), though significant progress remains necessary (Woollings et al., 2018b; Davini and D'Andrea, 2020; Schiemann et al., 2020; Simpson et al., 2020). Currently, many GCMs suggest decreases in blocking in winter and summer more generally throughout the Northern Hemisphere (Barnes et al., 2012; Dunn-Sigouin and Son, 2013), with specific regions showing increases in either summer or winter blocking (Davini and D'Andrea, 2020). Despite regional differences (Masato et al., 2013b; Kennedy et al., 2016; Hanna et al., 2018a; Woollings et al., 2018b), blocking has

largely been underestimated under the RCP8.5 scenario. Many CMIP5 models project decreases in blocking in the North Atlantic and Pacific in fall and winter (Dunn-Sigouin and Son, 2013; Woollings et al., 2018b), with an increase in the spatial extent of blocking, particularly in summer (Nabizadeh et al., 2019). Moreover, of the many models included in the CMIP suites, the Community Earth Systems Model (CESM) model large ensemble (LENS) datasets (versions 1 and 2) show greater accuracy in representing blocking (Kay et al., 2015; Simpson et al., 2020). Yet, assessing high latitude blocking representation in CESM and its direct impact on Arctic sea ice has received little attention (e.g., Woods et al., 2017).

There exists an ongoing need to utilize fully coupled Earth system models, like CESM, to better understand the dynamic relationship between blocking and sea ice, when considering implications for future sea ice conditions. Therefore, this study seeks to address the following questions:

1) How is high latitude blocking represented in CESM LENS and how is it expected to change by the end of the century?
2) What is the historical and projected impact of blocking on Arctic sea ice concentration?
3) How are blocking impacts on sea ice mediated through atmospheric circulation and the surface energy budget?

4.2 Methodology

This study seeks to quantify past and future high latitude blocking and the effect of blocking on Arctic sea ice in the Community Earth Systems Model (CESM) Large Ensemble (LENS) project (Kay et al., 2015). This dataset contains 35 ensemble members originating from the same set of initial conditions for the period of 1920–2100 (1850–2100 for the first member).

For this study, the historical period of 1979–2005 is extracted from the historical runs (1920–2005) and compared with the RCP8.5 scenario projections for the period 2081–2100 (totaling 2006–2100) and compared with ERA5-based observations for the 1979–2005 period.

Blocking events are identified in the CESM LENS simulations (35 ensembles) using a seasonal variation on the Pelly and Hoskins (2003) and Masato et al. (2013) methodology as described in Chapter 2 and Wachowicz et al. (2021), but for daily 500 hPa heights instead of the 2PVU surface (given data availability) for both the 1979–2005 (historical) and 2081–2100 (RCP8.5 projected) periods. For both periods, a central blocking latitude similar to Pelly and Hoskins (2003) is calculated but follows the seasonal mean bandpass 200 hPa eddy kinetic energy computed similar to Wachowicz et al. (2021). For each ensemble member, along each longitude's central blocking latitude, the difference in daily 500 hPa approximately 15° north and south are computed (based on CESM's spatial resolution), where a positive difference indicates a reversal in the height field (i.e., positive height anomalies to the north with negative anomalies to the south). Blocking events are considered if these anomalies occur for two or more consecutive days and span a minimum of 15° longitude for both the historical and projected periods. For this study, we consider the North Atlantic (NA) basin as 270° to 360° longitude and the North Pacific (NP) as 135° to 225°. We further compare the seasonal blocking climatology from CESM LENS with the ERA5-based blocking index from Chapter 2 and Wachowicz et al. (2021) for the period 1979–2005.

Seasons of high and low blocking frequency in CESM LENS are computed for the North Atlantic and North Pacific basins to test how blocking frequency changes between the historical and end-of-century periods for each basin. To identify the high and low blocking seasons across all simulations for each separate period, the total number of blocking days are extracted for each

season, and the highest and lowest 10% of seasons are considered. From these seasons, mean atmospheric and sea ice conditions are calculated. Variables from CESM LENS that are considered include sea level pressure, 850 hPa winds and specific humidity, surface turbulent heat fluxes, and sea ice.

Sea ice observations used include the Walsh and Chapman sea ice concentration (WC) data set, spanning from 1920–2017, although only values from 1979–2005 are used here (Walsh et al., 2019). This dataset includes monthly average sea ice concentration throughout the entire Arctic basin. Atmospheric variables included in this study come from the ECMWF Reanalysis (ERA5, Hersbach et al. 2018) using both at a daily 1° spatial resolution and averaged over an entire season (meteorological variables) to maintain consistency with the ERA5-based blocking index from Wachowicz et al. (2021), or monthly averaged data (surface sensible and latent heat fluxes). Note that the convention for vertical fluxes is positive downwards for ERA5, where CESM vertical fluxes are corrected to reflect this convention. Unless otherwise indicated, statistically significant differences in the composites between seasons of high and low blocking activity in both observations (WC and ERA5) and the CESM LENS simulations (historical and projected) are computed using a 2-tailed t-test where $p < 0.1$.

4.3 Results

4.3.1 Historical Blocking Climatology

Figure 4.1 depicts the longitudinal breakdown of blocking frequency during the observational record. The blocking metric used for the ERA5 1979–2005 period suggests a strong underestimation of blocking in CESM LENS in the North Atlantic (NA) region, which is expected based on previously documented assessments of Greenland blocking representation in

climate models (e.g., Hanna et al., 2018). Some underestimation in annual blocking in CESM LENS compared to ERA5 is evident in the North Pacific (NP), but the magnitude is less than the North Atlantic.

The seasonal breakdown of blocking frequency indicates that in the western half of the NA, an underestimation of MAM and JJA blocking is more pronounced than in SON and DJF (Figure 4.1). The overestimation in the eastern half of the NA basin is driven by more MAM events in CESM, thus suggesting the location of MAM storm tracks in CESM is further east than expected. This overestimation of blocking in the eastern half of the NA basin for CESM LENS compared to reanalysis is likewise consistent with Kwon et al. (2018), who show biases in the wintertime eddy-driven jet representation playing a role in blocking climatology; this is further demonstrated when comparing the latitude of maximum 200 hPa EKE in ERA5 and CESM LENS (Figure 4.2a), which show a higher maximum latitude near 50 degrees in CESM compared to around 45 degrees in ERA5. The JJA, SON, and DJF spread of blocking frequency in the eastern portion of the region is comparable to ERA5, as evident by consistent agreement in seasonal EKE in ERA5 (both 200 hPa and 300 hPa) and CESM LENS (200 hPa) (Figure 4.2a-b). In the NP, JJA and SON blocking in CESM appears consistent with ERA5, while blocking is underestimated in both DJF and MAM in CESM (Figure 4.1), despite an overestimation in CESM of the latitudinal placement of maximum 200 hPa EKE in SON (Figure 4.2a). Given both blocking metrics' dependence on longitudinal variation in EKE by which blocking is estimated, the likely cause for the differences in blocking climatology may stem from a displacement in the predominant storm track in CESM, which has been previously documented by other studies (Kay et al., 2015: Kwok et al., 2018; Simpson et al., 2020).

While there is some discrepancy in blocking representation in CESM LENS for both basins compared to ERA5, we acknowledge this for two reasons. First, the dynamical representation of blocking between the two variables used (i.e., PV-theta-based versus 500 hPa height-based) may result in minor differences due to blocking types (e.g., Omega blocking, Rossby wave breaks, etc.), such as those originally documented by Pelly and Hoskins (2003) and others (Barnes et al., 2012; Wachowicz et al., 2021; Preece et al., 2022), and the respective levels of EKE selected to estimate seasonal storm tracks, given the availability of certain CESM variables. The availability of saved CESM LENS output to compute daily blocking does not allow for exact calculation and interpolation to a constant potential vorticity surface, as used in Pelly and Hoskins (2003) and Wachowicz et al. (2021). However, the calculation of daily blocking closely follows the procedure outlined in Masato et al. (2013a), Masato et al. (2012) and Drouard et al. (2021), which are based on Pelly and Hoskins (2003). The second reason which may explain differences between the ERA5 and CESM blocking frequency, particularly in the NA, is related to CESM's internal variability inherently affecting blocking and blocking-related processes in this region, thus leading to an underestimation of blocking. Although the intricate nature of the NA climate processes is becoming better represented in climate models, systematic biases in NA blocking climatologies remain (Barnes and Polvani, 2015; Simpson et al., 2020; Athanasiadis et al., 2020). Regardless of the source(s) of blocking differences between CESM LENS and ERA5, the authors find a consistent pattern of relative maxima/minima between observations and the historical CESM simulations for the NA and NP regions, despite disagreement in the magnitude of blocking activity. By identifying high and low blocking seasons as a percentile based on number of blocking days for compositing, we can account for climatological differences brought on by CESM LENS and ERA5.

4.3.2 Historical and Projected Changes in Blocking

The distributions of number of blocking days per season within the CESM LENS simulations for the NA and NP regions are shown on the top row of Figure 4.3. In the NA (Figure 4.3a), CESM produces most variation in the number of days with blocking in MAM, with as many as 60 blocking days both historically and by the end of the century (2081–2100). Similarly, the spread for DJF, MAM, and JJA suggest upper bounds of high blocking activity of as many as 35 to 45 days. Comparing the mean number of days per season, historically, MAM experiences around 22 blocking days and is expected to see about a significant 10% decrease in the number of blocking days by the end of the century (Table 4.1). Both SON and DJF show a similar number of blocking days (10-11 days), though a significant 20% decrease is projected in DJF (Table 4.1). Of particular interest, however, is the significant 32% increase in projected JJA blocking by 2100, with as many as 14 blocking days (Table 4.1).

When considering the same metrics for the NP region (Figure 4.3b), the smallest change in the spread of the number of blocking days per season occurs in SON and DJF in both the historical and projected periods with 30-35 days of blocking each. There is little difference in the number of projected blocking days in MAM (maximum of ~45), although there is an increase in the number of projected blocking days in JJA in the future (maximum of about 55 compared to 80 days) (Figure 4.3b). Comparing the mean projected blocking days across all seasons from the 35 simulations (Table 4.1), DJF is projected to have a 19% reduction in the mean number of blocking days. Contrary to the NA, NP MAM events are projected to increase by 14% by the end of the century (Table 4.1). Most notable from Table 1 is the significant increase of almost 70% in blocking days in JJA. Taken altogether, results from Figure 4.3 and Table 4.1 suggest that by 2100, JJA (DJF) blocking may become much more (less) frequent in both regions while MAM

blocking may become more frequent in the NP and less frequent in the NA. The projected differences in individual seasons' number of blocking days may be partially attributed to the overall poleward shift in EKE (Figure 4.2c-d), combined with the role of transient eddies in blocking formation (Hwang et al., 2020; Drouard et al., 2021; Yang et al., 2021).

To build on the previous findings, histograms showing the distributions for the NA and NP regions of persistence in individual events are shown on the bottom row in Figure 4.3c-d, respectively. In the NA region (Figure 4.3c), overall (top panel) there is little discernible difference in the persistence of blocking events, particularly for events lasting less than 20 days; it appears that overall blocking is less persistent in the future compared to the historical period given the distributions of the historical (gray) versus the projected (colored) histograms. However, when considering seasonal changes, blocking in DJF is projected to be less frequent and less persistent than the historical period, with a reduction in average block persistence of about 9% (Table 4.2). In MAM, blocking appears to show no clear direction in terms of projected persistence (Figure 2c), however is expected to decrease (Table 4.2). Similarly, there is no clear change in blocking persistence in SON. For events lasting 10-15 days, projected JJA blocking may become more persistent than the historically period (Figure 4.3c). The average JJA block duration is projected to increase by almost 9% (Table 4.2). It appears that the projected decrease (increase) in DJF (JJA) blocking day *frequency* in the NA may be due to changes in the blocking *persistence*.

Broad shifts in the persistence of blocking overall are present in the NP region (Figure 4.3d), indicate more persistent events overall (top panel). The seasonal breakdown of the persistence at the end of the century indicates sharp changes in persistence occurring primarily in JJA but also in MAM. The thicker tail in the distribution for the projected persistence indicates a

large portion of events exceeding 20 days or greater primarily for JJA (Figure 4.3d), with average JJA block persistence increasing from 5.75 days to about 8.25 days (Table 4.2). Furthermore, Figure 4.3d suggests less persistent DJF and SON blocking in the NP, though neither decrease is considered significant (Table 4.2). Like the findings of NA persistence, it is plausible that the change in number of blocking days is driven by longer episodes of blocking instead of more frequent, but shorter events. Given the significance of persistent blocking in the current and projected climatic state, we turn now to examine blocking impacts on Arctic sea ice.

4.3.3 Expected Physical Impacts to Arctic Sea Ice

Figures 4.4-4.6 show lagged sea ice responses during high (top 10% of number of blocking days per season) and low (bottom 10%) blocking seasons in the NA. Generally, CESM LENS sea ice simulated responses to blocking activity do not match observations in terms of the magnitude to response, although the simulated regional sea ice-blocking response somewhat shows comparable directions of sea ice change, which is sensitive to specific seasons. Figure 4.4 shows the difference between high and low blocking for JJA, where observations show two regions with a sea ice response: the Baffin Bay and the Laptev Seas (Figure 4.4a). Based on observations, Baffin Bay sees less than 20% sea ice under high blocking conditions when compared to low blocking conditions starting immediately and continuing through the 3-month lagged period (Figure 4.4a-d). The magnitude of below-normal sea ice concentration experienced during high JJA blocking seasons is not represented in the historical CESM LENS runs, though the lagged loss in the Laptev Sea after 2 months remains consistent with observations (Figure 4.4e-h). However, because projected JJA sea ice is likely to deplete by mid-century (DeRepentigny et al., 2020), the projected blocking impacts on end-of-century JJA-SON sea ice appear moot (Figure 4.4i-l), though its contribution to accelerating summer sea ice loss going

into mid-century are of utmost importance. Observed increases in JJA NA blocking (Ding et al., 2017; Barrett et al., 2020; Wachowicz et al., 2021) when combined with projected increases in persistent blocking may accelerate the sea ice loss in the Laptev Sea going into the end of the century projections. Consequently, the lack of summertime Greenland and NA blocking representation in climate models like CESM, is problematic for assessing long-term climate impacts, especially given the connection between regional sea ice extent and Greenland ice sheet mass balance (Stroeve et al., 2017; Pedersen and Christensen, 2019).

The observed and simulated sea ice growing season in SON demonstrates no statistically significant sensitivity to blocking activity in the NA region (not shown). However, there is an observed, persistent sea ice loss near the southwest tip of the Greenland coast under high DJF blocking conditions when compared to low blocking, which is not exhibited in the CESM LENS simulations until after 2-3 months (Figure 4.5a-h). There is increased observed sea ice growth exceeding 10% of climatology near the east-central coast of Greenland occurring about 1 month after high DJF blocking activity (Figure 4.5b), which is not likely to not be a driver in regional sea ice growth by the end of the century (Figure 4.5i-l). The historical CESM simulations show sea ice loss exceeding 10% off the southeastern coast, which is somewhat evident in observations. Composites of observed sea ice and historical CESM runs indicate less sea ice in this region during high blocking conditions, which is projected to continue sea ice loss from high blocking the end of the century in the Canadian Basin and Labrador Sea (Figure 5i-l). This shift in the direction of sea ice signal near the end of the century suggests that receding sea ice in the region is likely during the earlier part of the growth season.

During months of high blocking activity in MAM (Figure 4.6), the spatial pattern in sea ice response is similar to DJF (Figure 4.5), with the southern tip of Greenland experiencing

below normal (exceeding 15%) sea ice conditions, but above normal conditions on the central-eastern coast, persisting up to 2 months after MAM blocking when compared to low blocking conditions (Figure 4.6a-d). Although not as evident in observations after the 2-month lag, a similar pattern appears in the historical CESM LENS simulations (Figure 4.6e-h) under high blocking conditions, suggesting that CESM appears to capture the spatial pattern and magnitude of the sea ice response 0-1 months out within the NA basin along southern and eastern coastal Greenland. However, the CESM historical simulations overestimate this response at the 2-3 month lag when compared to observations. Projected patterns of sea ice responses to future MAM blocking (Figure 4.6i-l) show similar patterns to the observations and historical simulations, suggesting that projected seasons of high blocking activity will likely result in less sea ice compared to seasons of low blocking in the Labrador Sea and more sea ice along the central-eastern coast of Greenland.

Similar sea ice composites to those in the NA are produced for high versus low blocking conditions in the NP (Figures 4.7-4.10). Seasons of high JJA NP blocking show below normal sea ice exceeding -10 % compared to climatology (as well as compared to low blocking seasons) in the Beaufort Sea persisting later into the season, including above normal sea ice conditions of 15% or more in the Laptev Sea (Figure 4.7a-d). This observed pattern remains consistent with the CESM historical simulations only in the Beaufort Sea region (Figure 4.7e-h), though appears stronger compared to the observations. Similar to the findings from the NA, projected high blocking impacts on summer sea ice are likely limited to only the Bering Strait and Central Arctic in JJA only (Figure 4.7i-l), as future JJA-SON sea ice will also be physically limited.

Seasons of high SON blocking relative to low blocking in the NP show consistent positive sea ice anomalies in the Canadian Basin and the periphery of the North Atlantic, with

negative ice anomalies in the Bering Sea after 1 month (Figure 4.8a-d). The CESM historical runs indicate significant positive sea ice anomalies in the Canadian Basin at a 1-3 months lag as well as the negative anomalies after 2 months, though both anomalies are not of a comparable magnitude to those observed (Figure 4.8e-h). Furthermore, the projected sea ice anomalies after 1-3 months of high SON blocking suggest below normal sea ice north of the Canadian Archipelago and into the Central Arctic (Figure 4.8i-l). This shows that winter sea ice growth in this region may become more sensitive to SON blocking conditions in the future, even if the persistence or number of blocking days remain unchanged.

In DJF, under high blocking conditions, persistent observed positive sea ice anomalies exceeding 15% are evident through the 3-month lag in the Bering Strait (Figure 4.9a-d) when compared to low blocking seasons. Additionally, positive anomalies are observed along the periphery of the Labrador Sea with negative anomalies off the coast of east-central Greenland. However, a consistent pattern matching those in observations of sea ice under high/low blocking conditions is not evident in the historical CESM simulations, which instead shows negative anomalies in the Canadian Basin during a 0-1 month lag and off the coast of Scandinavia through a 3-month lag (Figure 4.9e-h). Although CESM does not capture the observed sea ice variability under high and low blocking conditions, the projected sea ice signal with respect to the modeled signal suggests strong sensitivity in sea ice to blocking activity throughout the Arctic (Figure 4.9i-l). In particular, CESM projects DJF high blocking seasons to result in greater sea ice loss in the Beaufort Sea, enhancement of the historical sea ice loss off the coast of the Scandinavian Peninsula (Figure 9e-h), concurrent with greater sea ice growth in the Canadian Basin and western portion of the Greenland Sea (Figure 4.9i-l). The confidence of the sensitivity of sea ice to DJF NP high blocking activity in CESM LENS is therefore limited, given the inability of the

model to represent the historical variability in sea ice concentration caused by high or low blocking activity.

Figure 4.10 depicts MAM NP blocking impacts on sea ice. The most prevalent sea ice signals occur after 1 month of high MAM blocking conditions, when observed blocking conditions in the NP promote below-normal sea ice in the NP and above-normal sea ice along the periphery of the NA (Figure 4.10a-d). However, in CESM there is a modest negative signal in the western Bering Sea during lag of 0-1 months (Figure 4.10e-f), with increasingly positive anomalies in the Beaufort Sea with the 2-3 month lag (Figure 4.10g-h), which is not evident in the observations. Furthermore, the remote positive sea ice signal observed in the NA basin is not exhibited in the historical CESM simulations (Figure 4.10e-h). The inconsistencies between CESM and with observations further lowers confidence in the projected sea ice responses. Strong projected positive anomalies developing in the Canadian Basin and NA after 1 month may or may not be physically plausible (Figure 4.10i-l). However, given the projected increase in MAM blocking in the NP (Table 4.1), like DJF, care must be taken to better account for historical blocking representation and consequential physical processes to firmly discern blocking impact on future Arctic sea ice and global climate.

4.3.4 Atmospheric Drivers of Sea Ice Changes During Blocking

We show composites of atmospheric conditions (500 hPa heights, 850 hPa temperatures and specific humidity, and surface latent and sensible heat fluxes) under high and low blocking seasons for ERA5, historical CESM and projected CESM simulations to discern atmospheric drivers of sea ice variability (Figures 4.11-4.18). The average atmospheric conditions during seasons of high and low blocking for the NA are shown in Figures 4.11-4.14 and for the NP shown in Figures 4.15-4.18 for both ERA5 and CESM LENS. In the NA, JJA high blocking

seasons coincide with significantly above average 500 hPa geopotential heights over northern Europe in ERA5 (Figure 4.11a), where this pattern is likewise consistent within the historical CESM simulations (Figure 4.11b). At the end of the century, the CESM simulations suggest a westward shift and broadening of the center of the positive anomaly to the Labrador Sea/Baffin Bay and over Greenland (Figure 4.11c), though the magnitude of the anomaly does not appear to change. Significant 850 hPa temperature and specific humidity anomalies are observed over Greenland, Northern Europe, and the Laptev Sea, with negative temperature anomalies over the Scandinavian Peninsula (Figure 4.11d) and remain relatively consistent between the historic CESM simulations and ERA5 reanalysis (Figure 4.11e). The projected location and magnitude of the strongest specific humidity anomalies appears to not change at the end of the century, though a 1K temperature change is exhibited over Greenland (Figure 4.11f). Observed positive anomalies of turbulent (latent and sensible) heat fluxes occur near Iceland (Figure 4.11g, j), though these anomalies appear underestimated in CESM (Figure 4.11h, k). Projected positive anomalies of the turbulent heat fluxes follow the westward shifts in height and temperature under high blocking conditions compared to low blocking, though will remain weaker compared to the historical simulations (Figure 4.11i, l). Taken together, the positive temperature and turbulent heat anomalies from ERA5 and CESM coincide with the negative sea ice anomalies in the Laptev Sea shown in Figure 4.4.

Figure 4.12a-b shows SON blocking in the NA as a broad area of significant positive height anomalies, though the spatial extent of these anomalies is smaller in CESM. The anomalies are projected to increase both spatially and in magnitude throughout the NA (Figure 4.12c). Positive temperature anomalies (near 5K) are observed with high blocking in ERA5 when compared to low blocking seasons (Figure 4.12d) but are not comparable in magnitude to

the CESM historical simulations (Figure 4.12e), despite a projected increase in the Labrador Sea region of 3-4K anomalies compared to the historical simulations (Figure 4.12f). Unsurprisingly, there is a shift in areas of positive turbulent heat flux anomalies under high blocking when compared to low blocking between ERA5 and CESM historical simulations (Figure 4.12g-h,j-k), where simulated fluxes in the NA are also severely underestimated regarding magnitude compared to ERA5 (5-10 W m^{-2} in CESM compared to >20 W m^{-2} in ERA5). Despite weaker heat anomalies, the projected location of latent and sensible heat anomalies appears to match the historical simulations, though may become weaker near the end of the century (Figure 4.12i, l). This may explain the limited sea ice response both observationally and from the model simulations (not shown).

Strong ridging and positive height anomalies are present in the Atlantic basin under DJF high blocking conditions in the NA (Figure 4.13a). While CESM appears to overestimate the magnitude of the NA height anomaly, it does indicate significant height anomalies over Greenland and the entire NA basin during periods of high blocking when compared to low blocking seasons (Figure 4.13b). It is likely that the magnitude and spatial extent of this anomaly will increase at the end of the century (Figure 4.13c), assuming a hypothesized shift to a more meridional flow (Francis and Vavrus, 2015; Nabizadeh et al., 2019; Sussman et al. 2020). Despite underestimated temperature and specific humidity anomalies in CESM compared to ERA5 when considering seasons of high versus low blocking (Figure 4.13d-e), a significant increase in 850 hPa temperatures is likely in the western portion of the NA (Figure 4.13f). The increase in 850 hPa temperatures and specific humidity coincide with significant increases in turbulent fluxes (particularly latent heat) at the end of the century, even though the magnitude of observed significant positive turbulent flux anomalies is not well-captured in the CESM

historical simulations (Figure 4.13g-l). It seems plausible that the underestimation of the heat anomalies in CESM may explain why the negative sea ice response around Greenland is not as prevalent as observations (Figure 4.5).

While the magnitude of the simulated MAM height anomalies associated with NA high blocking seasons is not consistent with ERA5, the location of the anomaly is realistic when compared to ERA5 (Figure 4.14a-b). Furthermore, there is a projected increase in magnitude in NA MAM blocking in CESM, where the location of high versus low blocking remains spatially consistent (Figure 4.14c). This projected increase in NA MAM blocking is likely to result in the significant temperature and specific humidity anomaly increases over Greenland, despite historically underestimating these variables compared to observations (Figure 4.14d-f). Consequently, the projected increase in turbulent fluxes in CESM are still historically underestimated compared to ERA5, though historical simulations of CESM do indicate significant positive anomalies of both latent and sensible heat in the NA under high NA blocking conditions when compared to low blocking conditions (Figure 4.14g-l). While the magnitude of the modeled atmospheric anomalies vary from the observations, they appear to be well-enough aligned in location to elicit similar sea ice responses (Figure 4.6), given the positioning and relative magnitude of the anticyclonic anomalies to possibly enhance sea ice export in the Greenland Sea.

Positive height anomalies during JJA in the Bering Sea during seasons of high NP blocking in the historical CESM simulations appear to shift poleward by the end of the century when compared to seasons of low blocking (Figure 4.15a-c). Along with the projected poleward shift in the height anomalies, consistent observed and simulated 850 hPa temperature anomalies of 0.5-2K and above-normal specific humidity anomalies occur in the Bering Sea region (Figure

4.15d-f). Given a somewhat weaker height anomaly in CESM compared to ERA5, there are associated weaker specific humidity anomalies, which are projected to shift poleward following the shift in high blocking conditions. Despite no observed significant turbulent heat fluxes, CESM shows significant positive flux anomalies north of the Bering Strait which may become more negative because of the projected shift in location of NP JJA blocking (Figure 4.15g-l). Despite the negative Beaufort sea ice response within 0-1 months to JJA blocking, the lack of observed significant heat fluxes in CESM introduces some uncertainty into the atmospheric drivers of sea ice loss in this region (Figure 4.7).

The ERA5 and CESM historical SON NP blocking indicate positive 500 hPa height anomalies in the Bering Sea with an increase in the projected strength (Figure 4.16a-c). Furthermore, the historical height anomaly in CESM is negatively tilted and the projected anomaly appears to become more positively tilted. The shift in the tilt of the anticyclonic anomaly implies potential changes in wave propagation and associated heat transport. Despite a projected increase broadening of the low-level temperature anomaly spatial extent as well as more moist conditions under high blocking seasons compared to low blocking near the Bering Sea (Figure 4.16d-f), the area of significant positive turbulent fluxes is no longer present in the projection (Figure 4.16g-l). Furthermore, the limited sea ice signal associated with SON blocking (Figure 4.8), suggests that remote sea ice signals from NP SON blocking may be more important going into the future, as the projected negative sea ice signal in the Canadian Archipelago is worth exploring in greater detail.

Similar to the NA, DJF blocking appears alongside strong height gradients through the entire NP basin during high blocking seasons (Figure 4.17a). The pattern of simulated historical blocking remains mostly consistent with ERA5, though the eastern position of the NP basin

contains greater height anomalies in CESM (Figure 4.17b). Most change in projected height anomalies during high blocking conditions coincide with a projected increase in the height gradient, though only the magnitude appears to increase (Figure 4.17c). Furthermore, there are projected significant temperature anomalies compared to both the historical simulations and ERA5, and specific humidity appears unchanged under seasons of high blocking activity despite observed significant positive specific humidity anomalies (Figure 4.17d-f). Significant positive heat flux anomalies occur along the western coast of the Bering Sea and the Pacific Ocean are still somewhat evident in the historical simulations, though the magnitude of these anomalies is noticeably lower in CESM (Figure 4.17g-l). The projected increase in temperature further explains the significant positive heat fluxes throughout the basin under high blocking activity compared to the low blocking seasons (Figure 4.17i, l). The observed positive sea ice anomalies in the North Pacific and the northern Greenland Sea appear directly related to negative turbulent flux anomalies, where this connection is not well captured in the CESM simulations (Figure 4.9).

The historical CESM simulations do not adequately capture the apparent magnitude and extent in MAM blocking in the NP, as CESM shows weaker height anomalies compared to ERA5 (Figure 4.18a-b). Moreover, projected height anomalies in this region indicate weaker anomalies associated with high blocking seasons near the end of the century (Figure 4.18c). As a result, CESM estimates of 850 hPa temperature and specific humidity anomalies are comparatively weak with ERA5 and projected to become less extreme during high blocking seasons with respect to low blocking seasons (Figure 4.18d-f). Positive latent heat flux anomalies are not significantly strong during high blocking seasons in the CESM historical simulation compared to ERA5 along the western portion of the NP (Figure 4.18g-h), whereas the spatial pattern of latent heating in CESM shows negative latent heat anomalies which are not evident in

observations. Moreover, the magnitude of sensible heat anomalies is not adequately represented in CESM, though both observations and CESM show significantly higher positive sensible heat anomalies with high blocking season (Figure 4.18 j-k). Both projected latent and sensible heat anomalies during high blocking seasons appear to strengthen, and follow similar geographic patterns as the historical simulations, though latent heating appears to be stronger than sensible heating (Figure 4.18 i, l). Overall, while CESM underestimates the magnitude of the atmospheric anomalies associated with historical blocking, the current representation shows the general pattern of negative sea ice anomalies in the NP basin (Figure 4.10).

Taken together, observations and the historical CESM simulations show strong blocking-sea ice connections in MAM and JJA in the NA. While the magnitude of observed positive sea ice anomalies occurring under high blocking seasons in the North Atlantic during this time are not present in CESM, the inconsistency in the magnitude and location of the modeled turbulent heat flux anomalies may prevent a proper remote sea ice response within the model. Furthermore, the preconditioning of the summer sea ice minima historically is consistent with findings from Yang and Magnusdottir (2017, 2018), where anticyclone (and blocking) activity during the spring will set the precedent of summer sea ice. Although not explored in detail here, the moisture transport along the periphery of strong anticyclones results in significant spring and summer sea ice loss (Kapsch et al., 2013; Yang and Magnusdottir, 2017; Yang and Magnusdottir, 2018; Huang et al., 2019). While we only considered 850 hPa specific humidity, it is evident from this work that seasons high blocking activity correspond with strong temperature and specific humidity anomalies in areas of the NA experiencing low sea ice anomalies.

The differences in CESM sea ice response to blocking compared to ERA5 and the WC sea ice observations is not surprising, as studies have documented ongoing issues with Arctic

cloud representation (including liquid clouds) affecting sea ice representation in even the most recent CESM simulations (Duvivier et al., 2020; McIlhattan et al., 2020; DeRepentigny et al., 2020). Because Arctic cloud representation in climate models is critical to realistic surface mass and energy balances, processes associated with insufficient representation of Arctic clouds during blocking events may be contributing to weaker sea ice responses, especially in the NP region. Despite previously documented cloud biases, we show in this study that warm season (MAM and JJA) blocking-sea ice relationships are realistic in the CESM LENS historical simulations for NA blocking. Given the projected increase (decrease) in JJA (MAM) blocking activity in the NA and specifically the persistence of these events, the extent to which projected anticyclonic anomalies and associated moisture transport play a role in the conditioning of MAM-JJA sea ice leading into the mid-century and end-of-century has yet to be explored and is encouraged as future work.

4.4 Summary

In this study, we compared an observed high latitude blocking climatology to that from a prominent global climate model large ensemble, CESM LENS. We further considered observed and projected impacts of blocking on Arctic sea ice in the North Atlantic and North Pacific basins through the use of spatial composites. The findings of this analysis further demonstrate a significant need for improving blocking representation in climate models, as the climatological impacts of blocked anticyclones play a significant, yet still uncertain, role in our understanding of the future of Arctic sea ice. This study has the following key findings.

When using a dynamic blocking index to identify events (e.g., Pelly and Hoskins, 2003; Masato et al. 2012), the CESM LENS simulations capture the historical (1979-2005) blocking

climatology in the North Atlantic and North Pacific. This instills confidence that there is likely to be an increase in the number of blocking days in JJA (~30%) and decreases in DJF and MAM (~10-20%) in the North Atlantic by 2081-2100, based on CESM LENS projections under the RCP8.5 scenario. Similarly, the North Pacific is projected to experience an increase in blocking days in JJA (70%) and MAM and decreases of ~20% for DJF by the end of the century. We showed that the change in number of blocking days may be related to changes in the persistence of these systems instead of the number of events.

There is strong seasonal variability in how sea ice concentration responds to seasons of high blocking activity both geographically and in magnitude. Moreover, the extent to which CESM LENS captures the sea ice responses varies drastically compared to observations, leading to increased uncertainty surrounding mass balance estimates. Although relatively comparable to observations, the lack of certain regional sea ice signals during North Atlantic JJA blocking in CESM may be consequential. Ongoing hypotheses relating regional sea ice to circulation patterns going into the future ice sheet mass balance projections rely heavily on accurate historical model simulations.

Both observed and simulated (historical and projected) blocking a shows the magnitude of the anomalies directly linked to greater low-level temperature, moisture, and turbulent heat flux anomalies. As such, seasons with weaker positive height anomalies in CESM when compared to observations result in weaker surface and near-surface atmospheric anomalies. The blocking seasons with immediate (0-1 month lag) basin-specific sea ice responses and consistent model representation include MAM in both the North Atlantic and North Pacific, and JJA in the North Atlantic. Despite weaker atmospheric anomalies (500 hPa geopotential height and 850 hPa temperature and specific humidity) when comparing historical CESM LENS simulations with

ERA5 during MAM blocking in both basins, increased focus should be placed on improving the representation of high-latitude MAM blocking anticyclones and associated atmospheric drivers and sea ice responses (both immediate and lagged into the summer) within CESM to determine whether the anticyclonic anomalies induce sea ice export. Consequently, increased blocking activity (but weaker blocks with weaker heat fluxes) in the North Pacific may result in the depletion of NP sea ice at a slower rate. Alternately, reduced MAM blocking frequency (but increased intensity and persistence) may promote sea ice conditions through altering nearby heat and moisture fluxes needed for growth or by enhancing surface wind conditions conducive to ice export, allowing for more sea ice cover throughout the Arctic, even near the end of the century.

These findings, when taken together, should improve confidence in the current understanding of climate model representation of high latitude blocking in the ocean basins, despite some areas for improvement. Future work should aim to further quantify uncertainties in climate model representation of blocking and associated atmospheric-sea ice relationships, particularly during the projected sea ice growth season.

Table 4.1. Mean number of blocking days under historical (Hist) and projected (Proj) periods for blocking events lasting 2 or more days including the percent change (%) between the two periods (Proj – Hist). Statistic (t) and p-value (p) are computed using a t-test. Significant values ($p < 0.05$) are bolded.

	Hist	Proj	%	t	p
N Atlantic					
JJA	11.15	14.69	**31.76**	9.05	**4.51E-19**
SON	10.12	9.72	-3.99	-1.14	0.25
DJF	10.97	8.78	**-19.97**	-5.51	**4.30E-08**
MAM	22.18	19.75	**-10.95**	-4.45	**9.13E-06**
N Pacific					
JJA	20.04	34.02	**69.75**	23.38	**2.74E-104**
SON	8.28	7.93	-4.18	-1.13	0.26
DJF	8.46	6.85	**-19.04**	-4.26	**2.31E-05**
MAM	9.49	10.86	**14.38**	3.71	**0.00021**

Table 4.2. Mean blocking persistence under historical (Hist) and projected (Proj) periods for blocking events lasting 2 or more days including the percent change (%) between the two periods (Proj – Hist). Statistic (t) and p-value (p) are computed using a t-test. Significant values ($p < 0.05$) are bolded.

	Persistence (# Days)				
	Hist	Proj	Change (%)	t	p
N Atlantic					
ALL	5.02	4.91	-2.21	1.68	0.09
JJA	4.45	4.84	**8.86**	-3.25	**< 0.01**
SON	4.11	3.97	-3.43	1.33	0.18
DJF	4.44	4.03	**-9.33**	3.40	**6.96E-04**
MAM	6.11	5.83	**-4.55**	2.16	**0.03**
N Pacific					
ALL	4.82	6.24	**29.29**	-15.01	**1.96E-50**
JJA	5.75	8.22	**42.85**	-14.78	**2.03E-48**
SON	3.85	3.80	-1.40	0.50	0.62
DJF	4.16	3.89	-6.29	1.86	0.06
MAM	4.24	4.90	**15.68**	-4.13	**3.74E-05**

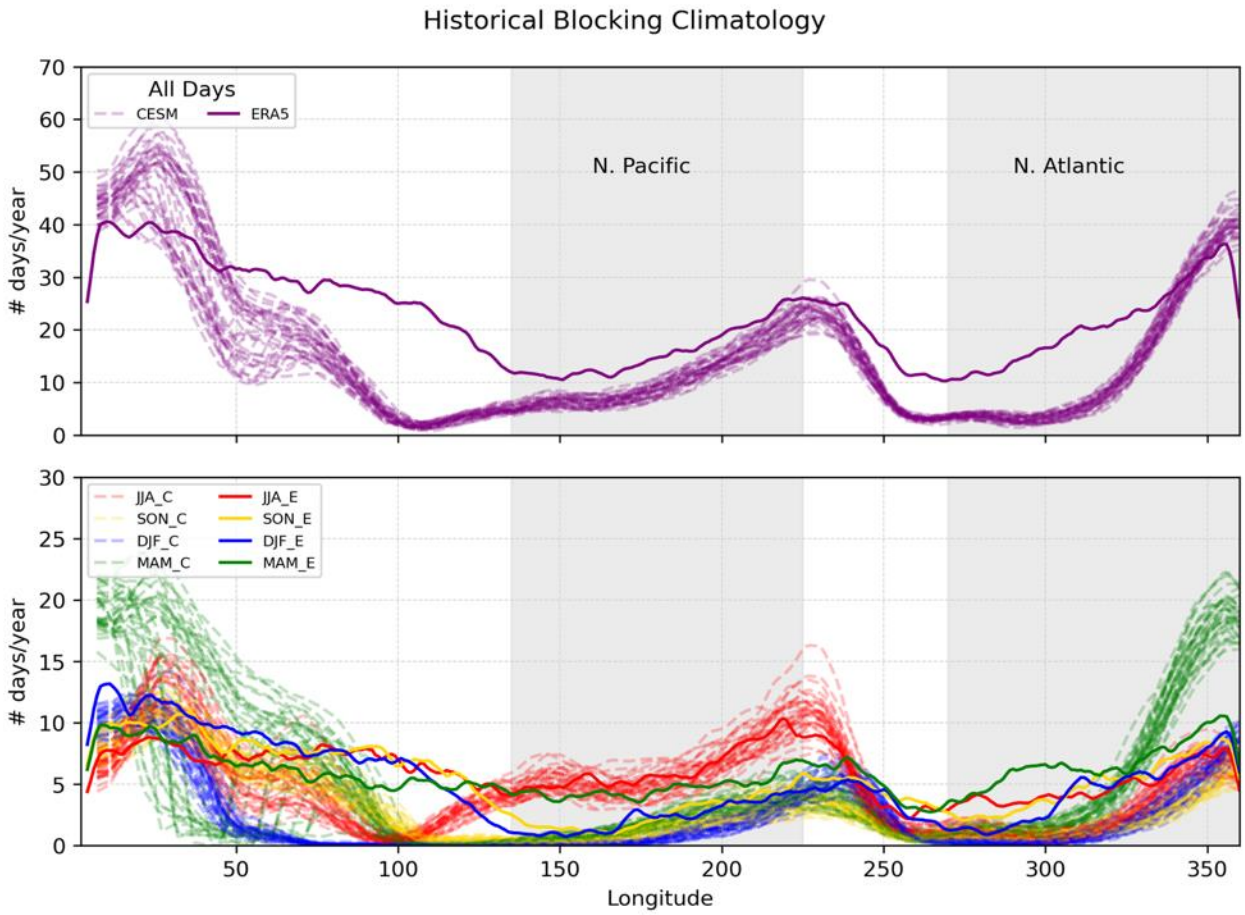

Figure 4.1. Total (top) and seasonal blocking frequencies by longitude during 1979–2005 for ERA5 (solid) and CESM LENS simulations (dashed).

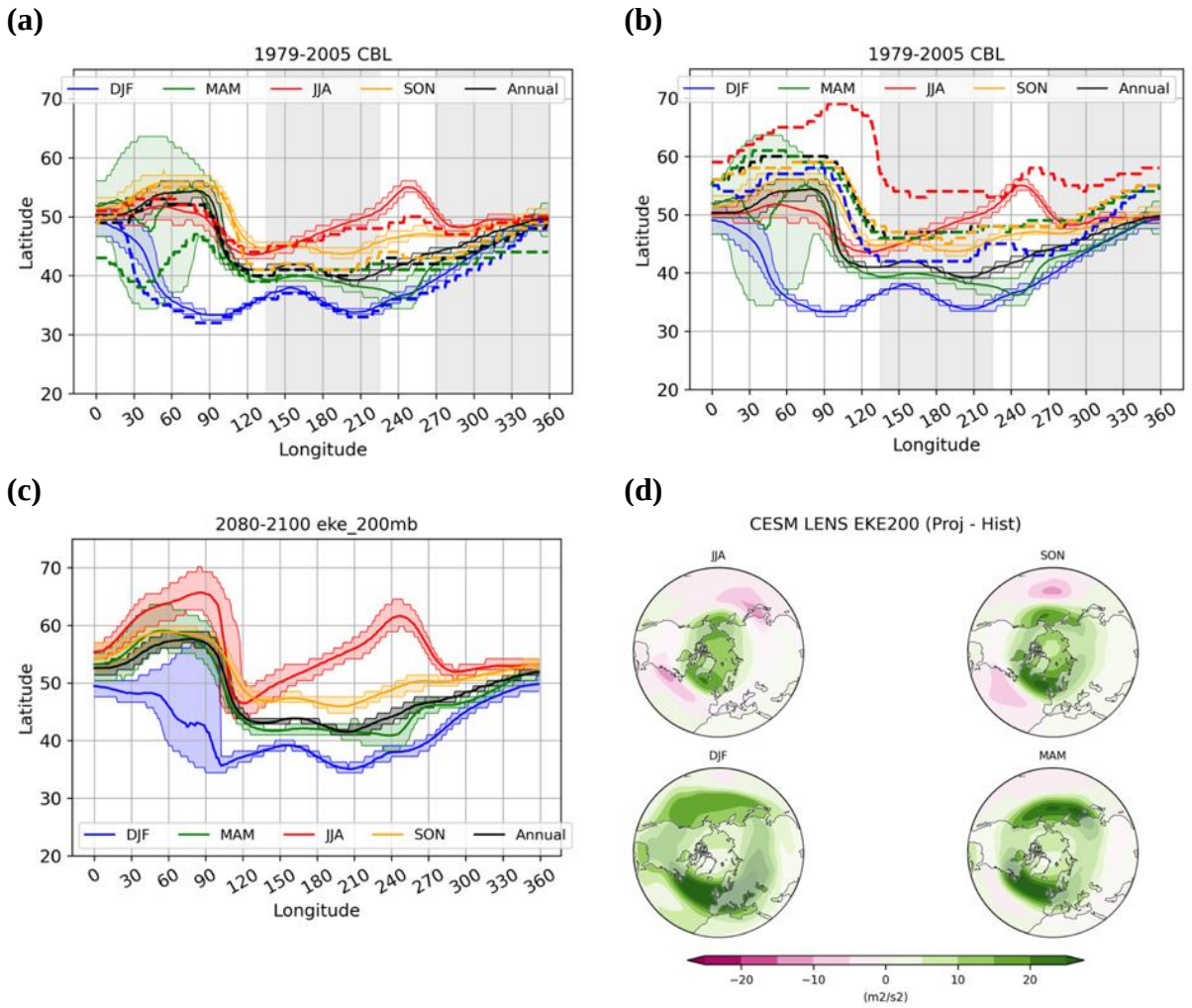

Figure 4.2. (a) Latitude of maximum 200 hPa EKE in ERA5 (dashed) and CESM LENS (solid) for the 1979-2005 period. (b) Central Blocking Latitudes (CBLs) used for identifying blocking from ERA5 (300hPa EKE; dashed) and CESM LENS historical (200 hPa EKE; solid) with the range of CBLs for individual ensemble members highlighted. (c) Range of projected period CBLs in CESM LENS (200 hPa). (d) Difference in average 200 hPa EKE for the projected period (2081-2100) minus the historical period (1979-2005) in CESM LENS.

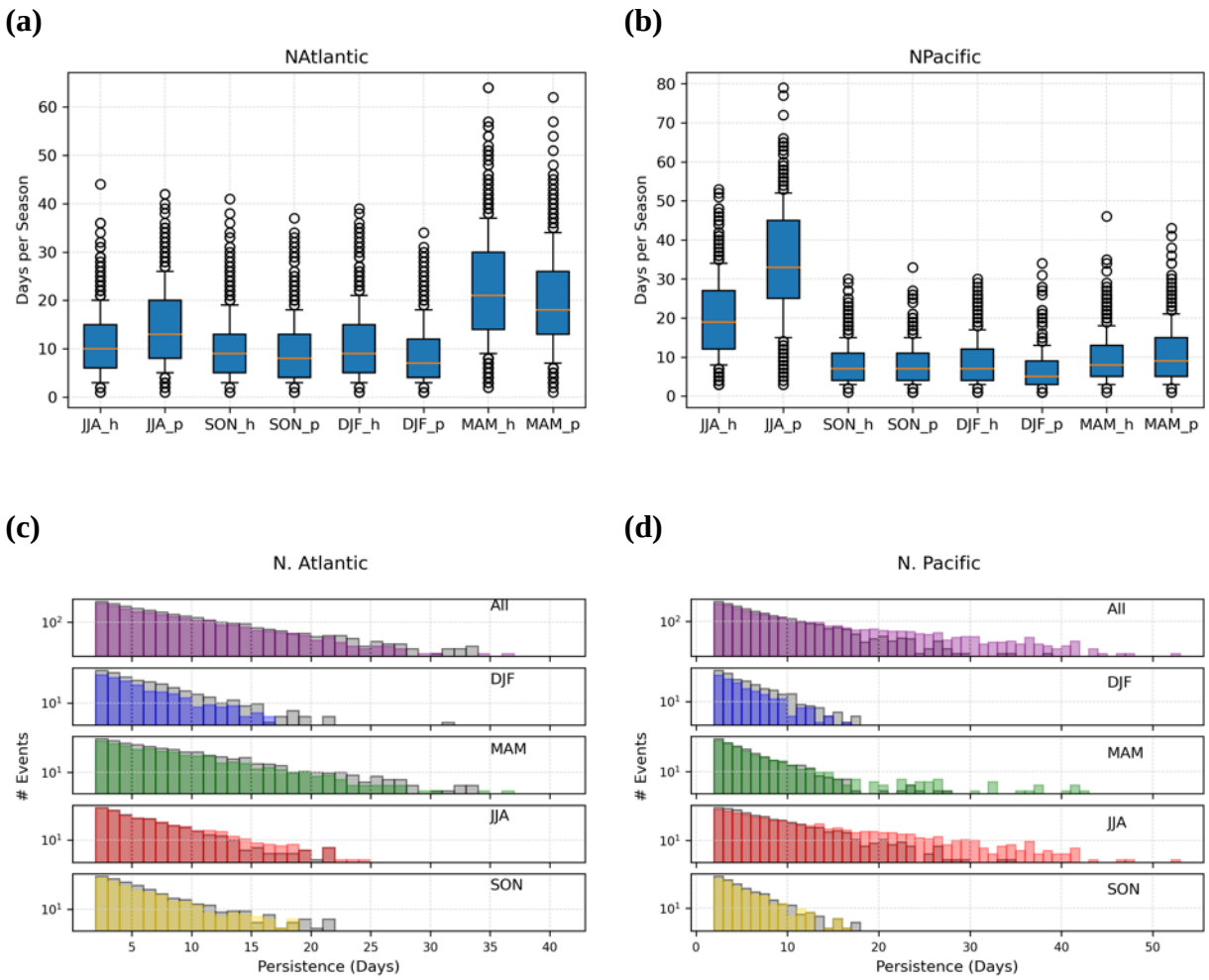

Figure 4.3. (a, b) Distribution of all blocking day counts per season across all 35 ensemble members for blocking events lasting 2 or more days for historical and projected periods for the North Atlantic (a) and North Pacific (b). The mean number of events is denoted by the orange line. The whiskers are at the 10 and 90 percentiles. (c, d) Distributions of persistence of blocking events lasting 2 or more days for historical period (1979–2005; gray) and projected period (2081–2100; colored) for the North Atlantic (c) and North Pacific (d). Seasonal blocking events are categorized by the month of the start of the block.

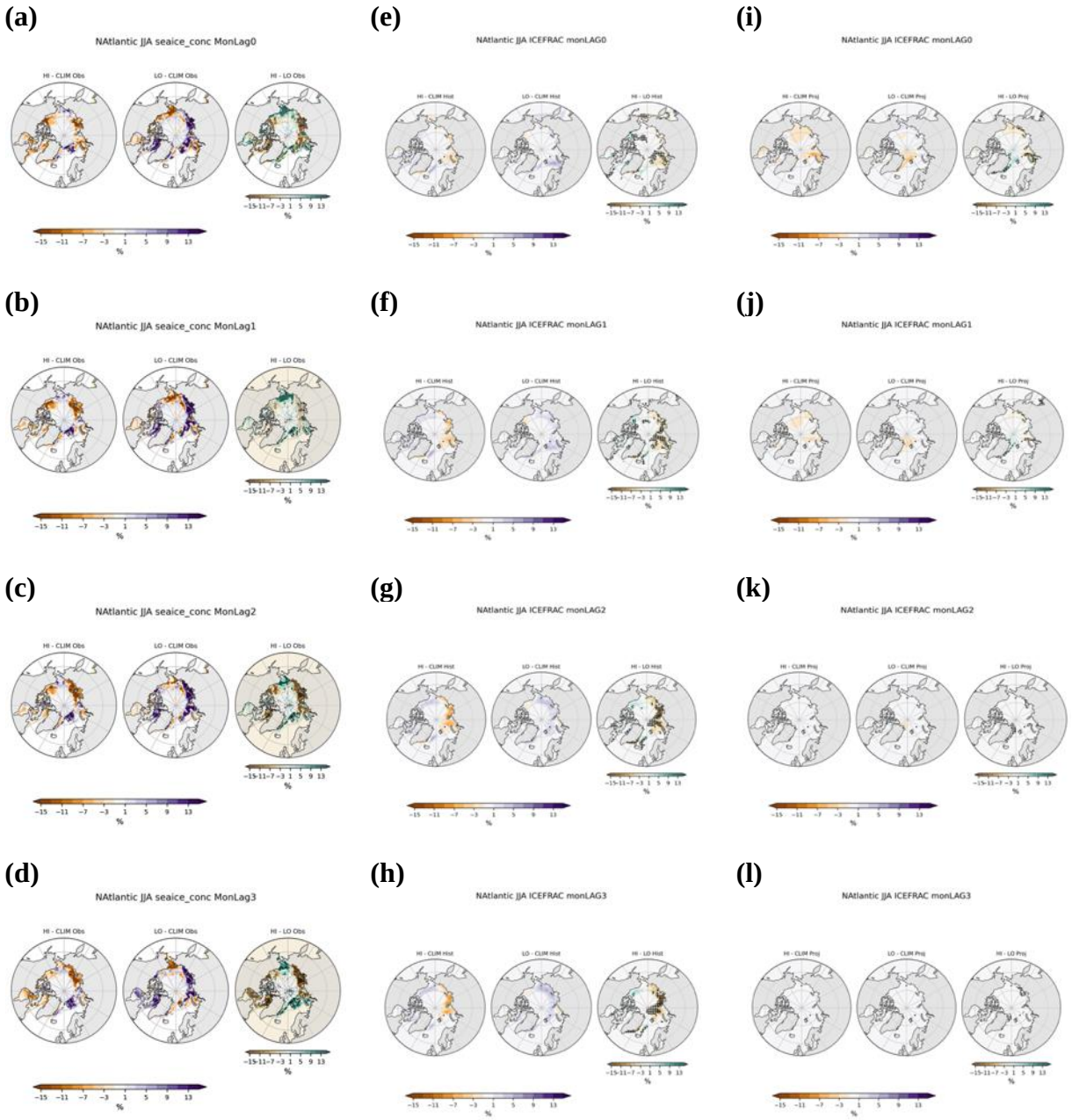

Figure 4.4. Lagged average sea ice concentration during North Atlantic JJA blocking for 1979 to 2005. Left column is observations, the center column is the CESM LENS historical simulation, and the right column is the CESM LENS RCP 8.5 projection for the 2081-2100 period. Seasonal sea ice is lagged by one month from JJA blocking seasons where JJA sea ice corresponding to JJA blocking is lag 0 (top row) and SON sea ice corresponding to JJA blocking is lag 3 (bottom row).

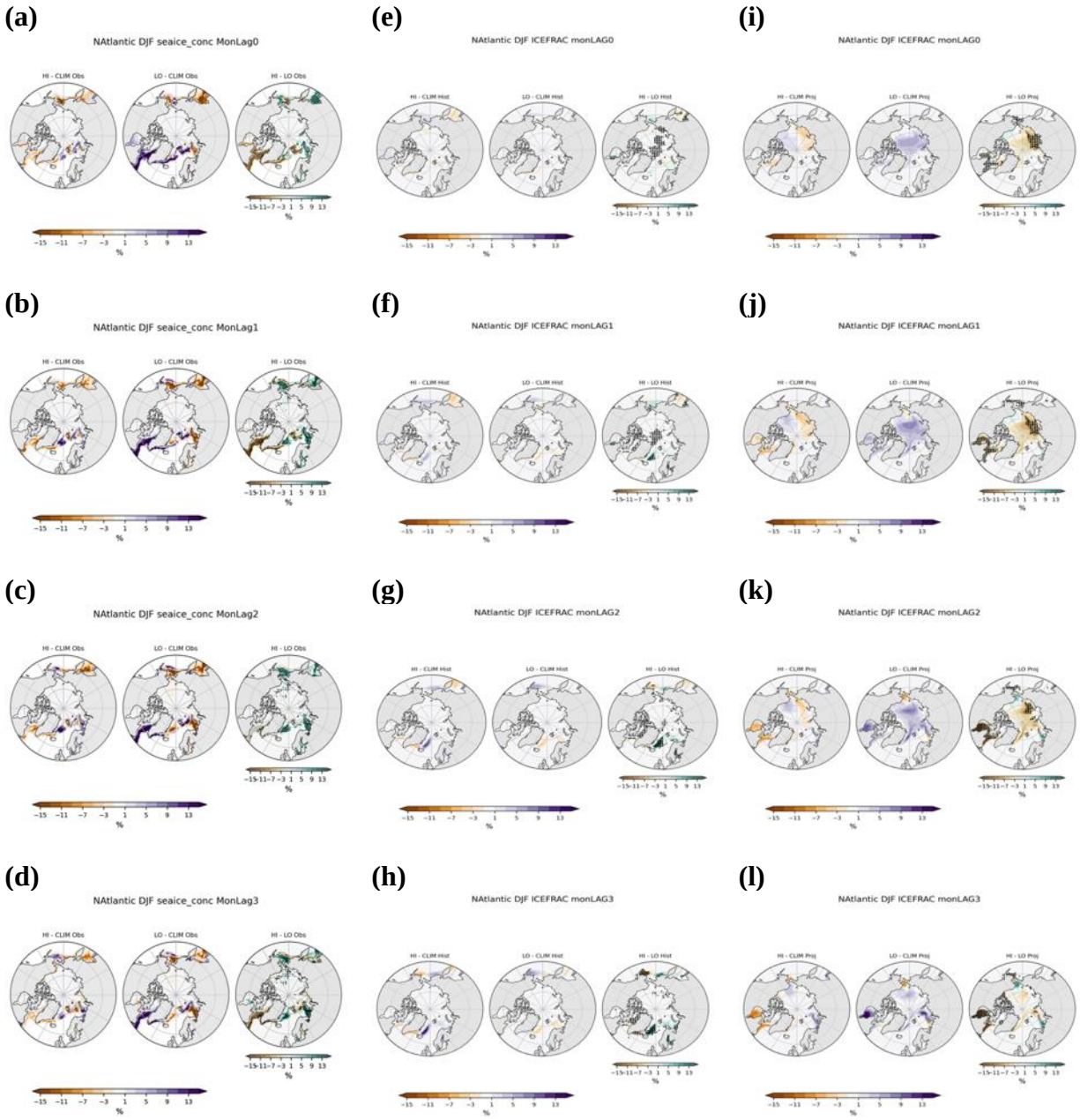

Figure 4.5. Same as Figure 4.4, but for DJF blocking and DJF (lag 0) to MAM (lag 3) sea ice.

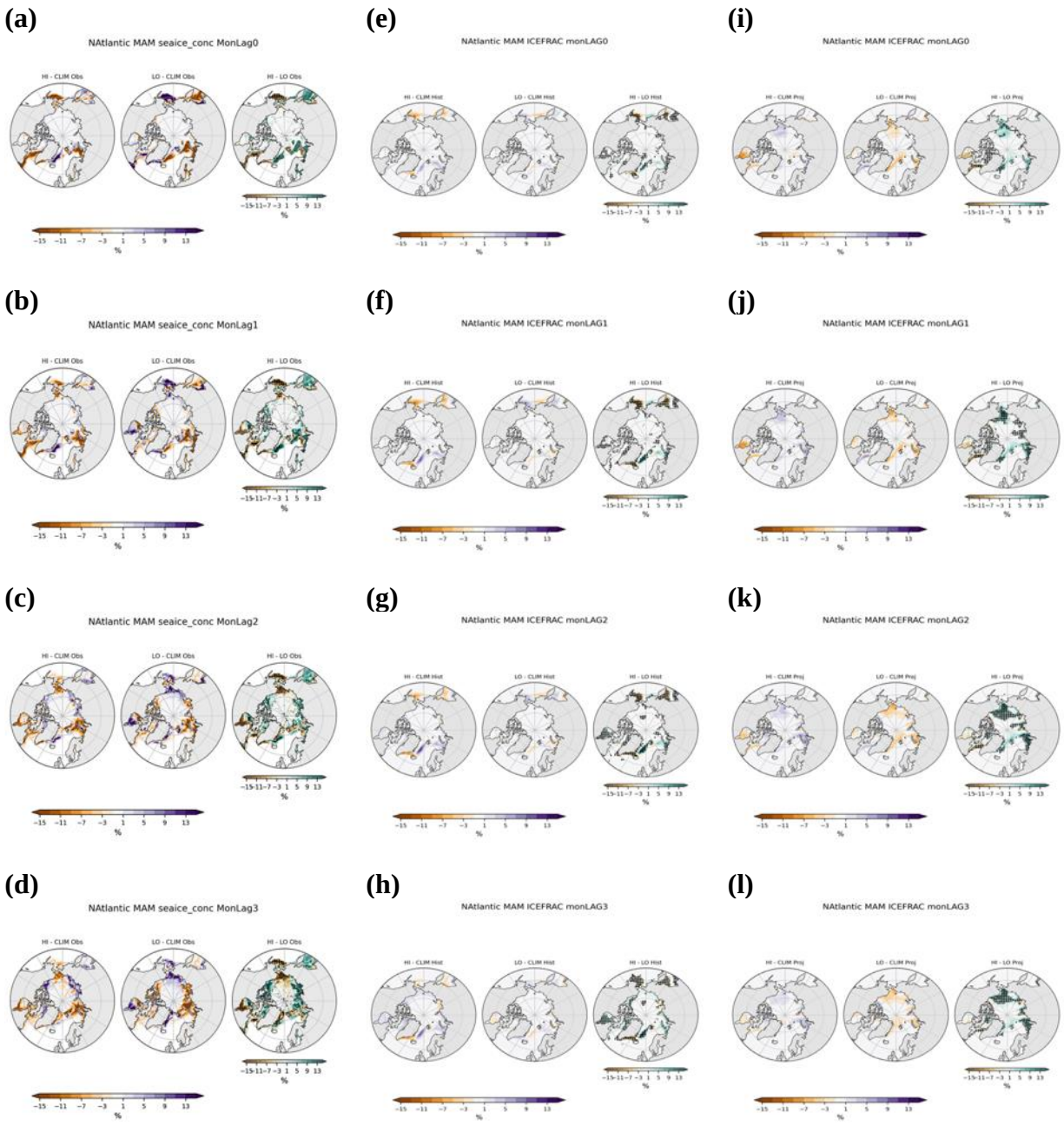

Figure 4.6. Same as Figures 4.4, but for MAM blocking and MAM (lag 0) to JJA (lag 3) sea ice.

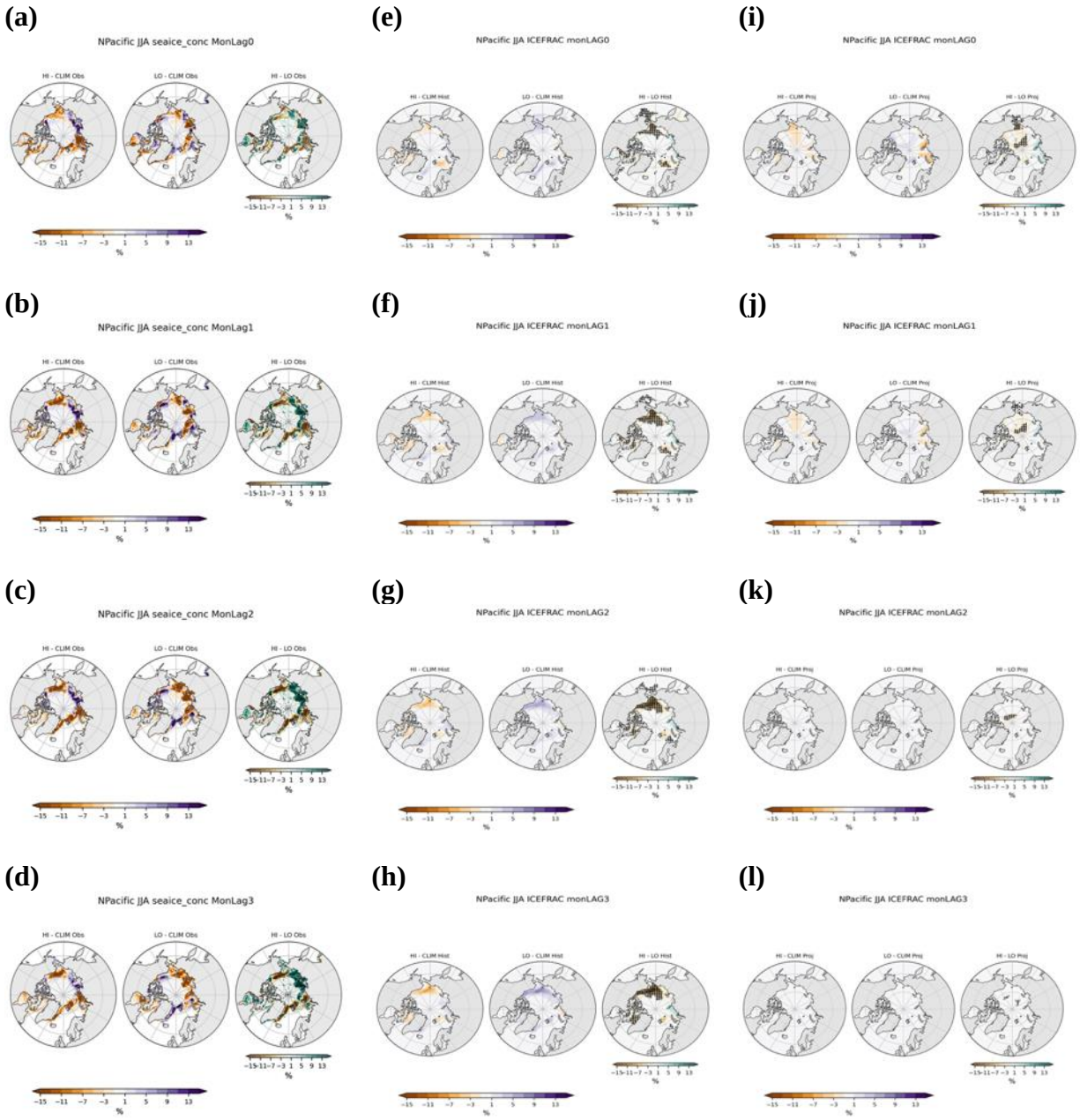

Figure 4.7. Same as Figure 4.4, but for North Pacific JJA blocking seasons.

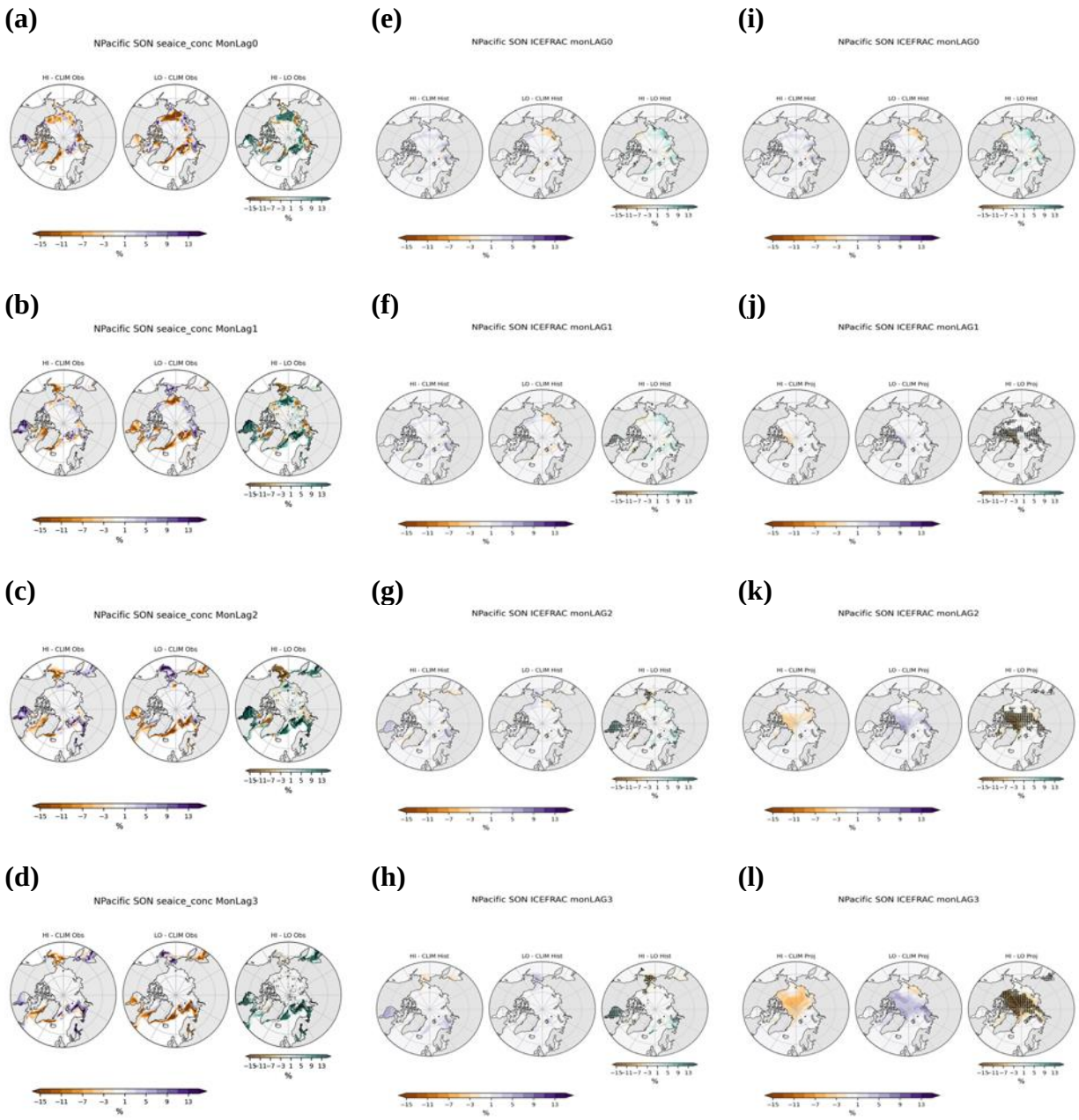

Figure 4.8. Same as Figures 4.4-4.7, but for SON North Pacific blocking and SON (lag 0) to DJF (lag 3) sea ice.

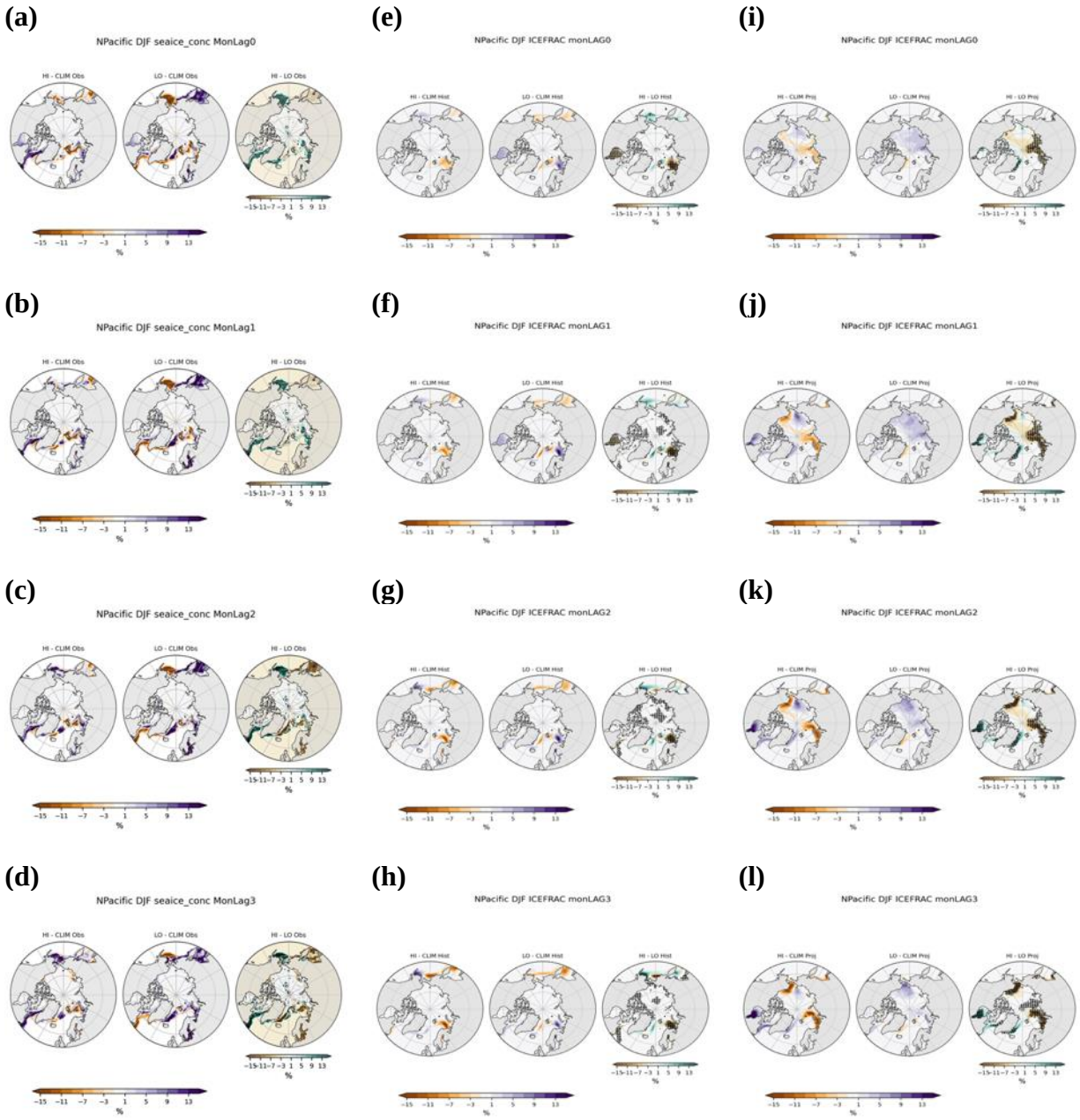

Figure 4.9. Same as Figures 4.4-4.8, but for DJF North Pacific blocking and DJF (lag 0) to MAM (lag 3) sea ice.

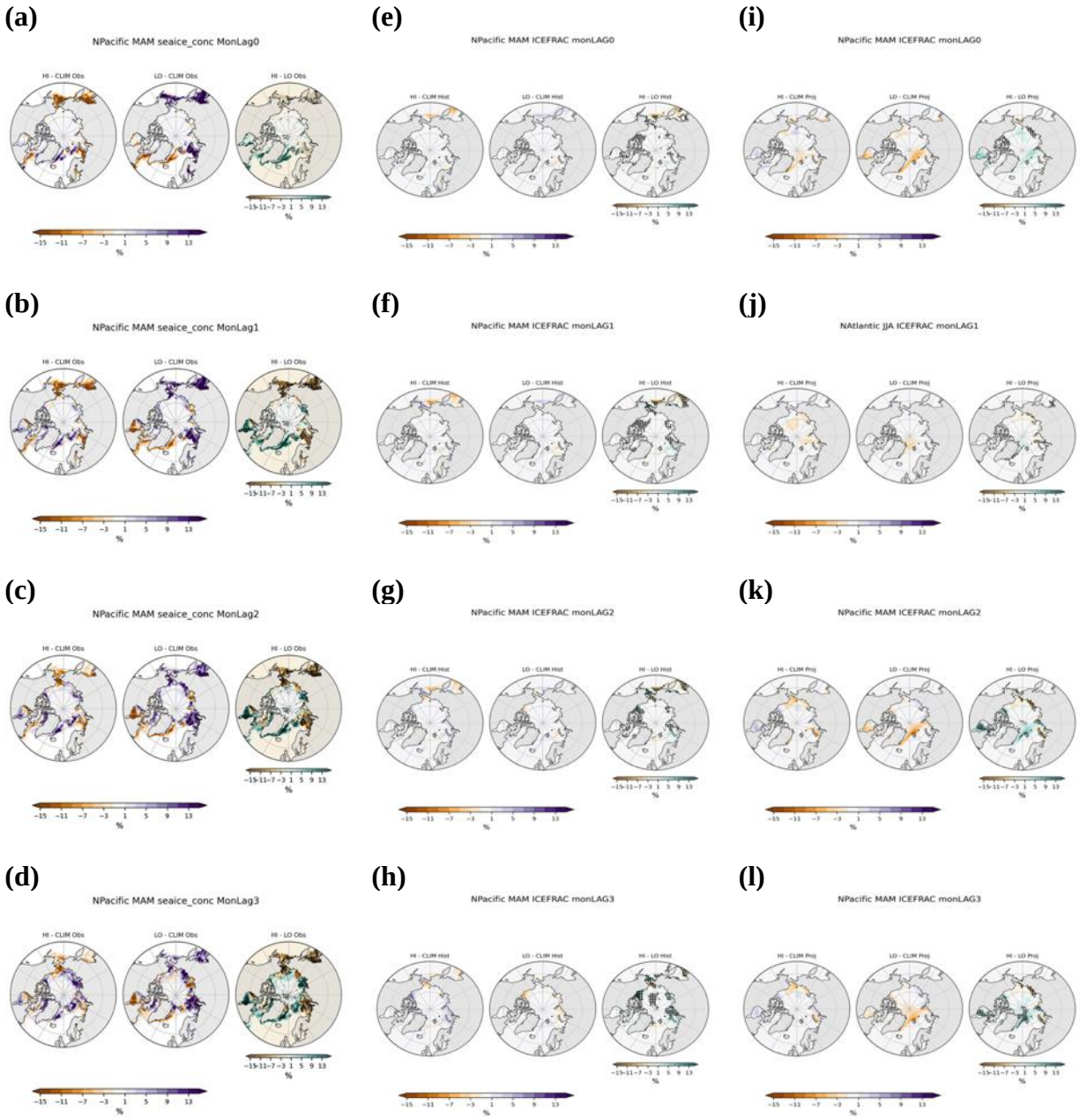

Figure 4.10. Same as Figures 4.4-4.9, but for MAM North Pacific blocking and MAM (lag 0) to JJA (lag 3) sea ice.

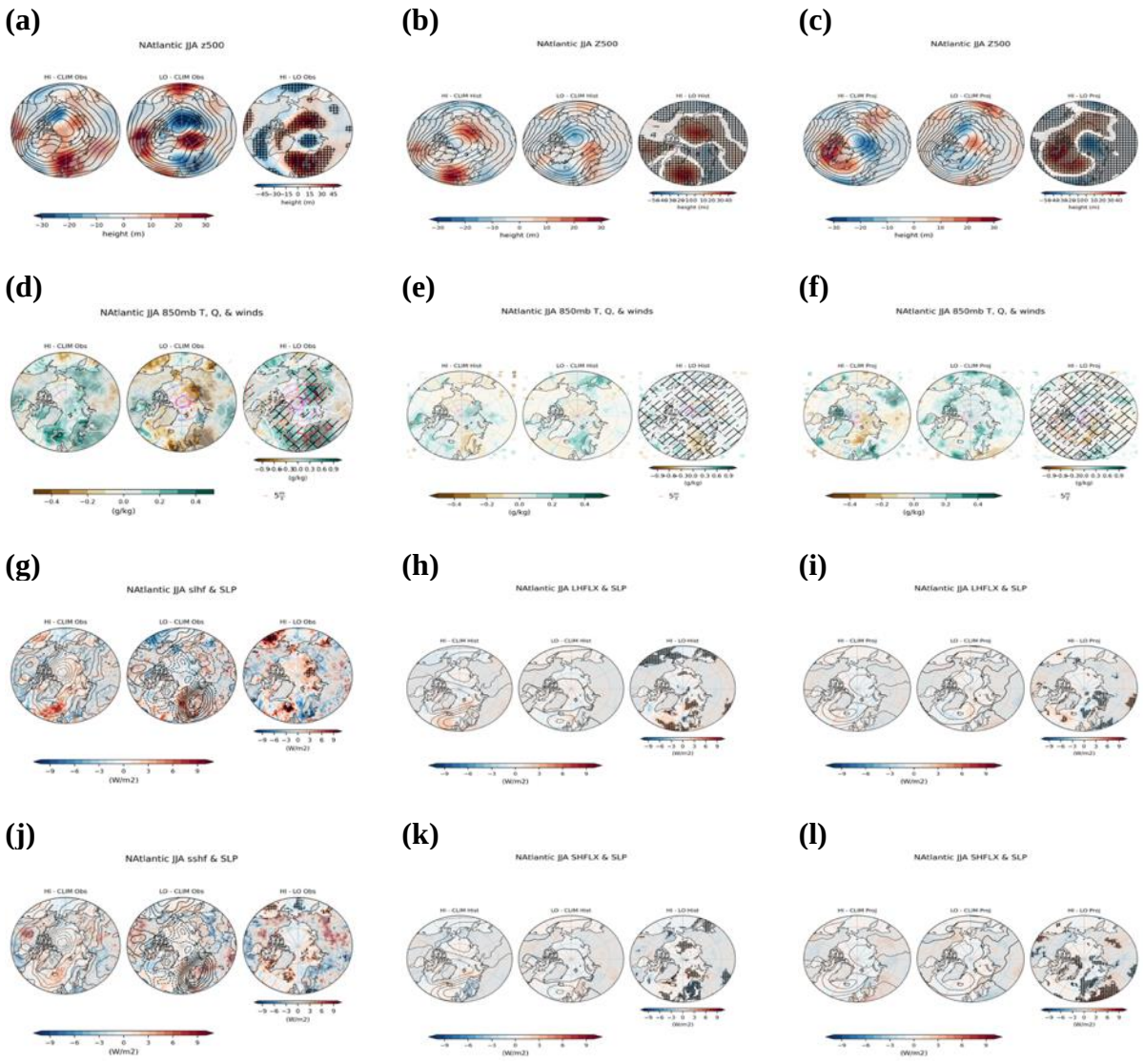

Figure 4.11. Observed (ERA5, left column), CESM historically simulated (center column), and projected (right column) seasonal meteorological conditions during North Atlantic JJA blocking seasons. Variables include 500 hPa heights (contours) and anomalies (filled; a-c); (d-f) 850 hPa temperatures (colored contours), specific humidity (filled contours), and winds; sea level pressure (contours) and latent heat flux (filled; g-i); sea level pressure (contours) and sensible heat flux (filled; h-l). Statistically significant differences between high/low blocking seasons are denoted by the hatching for 500 hPa height anomalies, 850 hPa temperature and humidity, and turbulent fluxes.

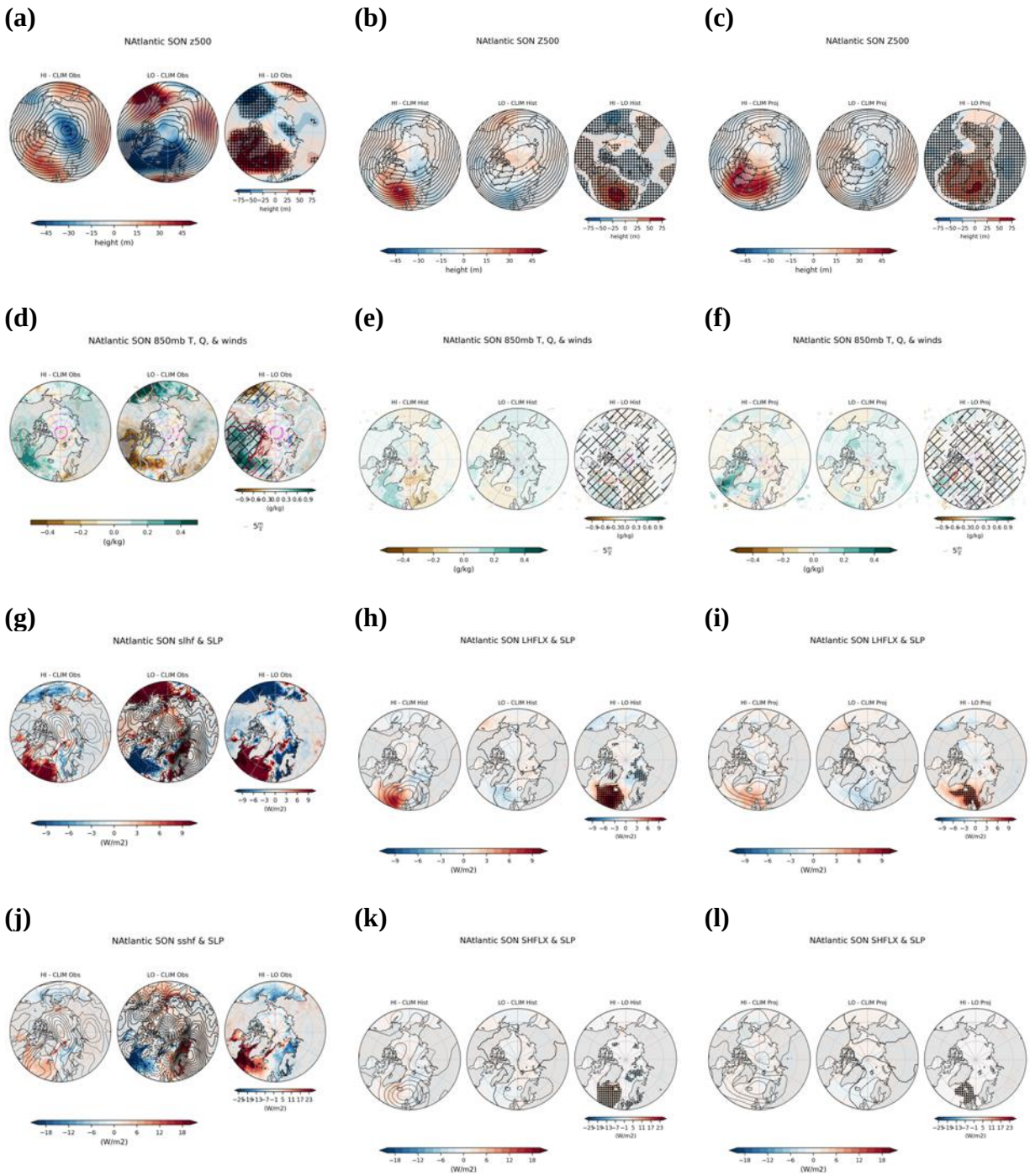

Figure 4.12. Same as Figure 4.11, but for North Atlantic SON blocking.

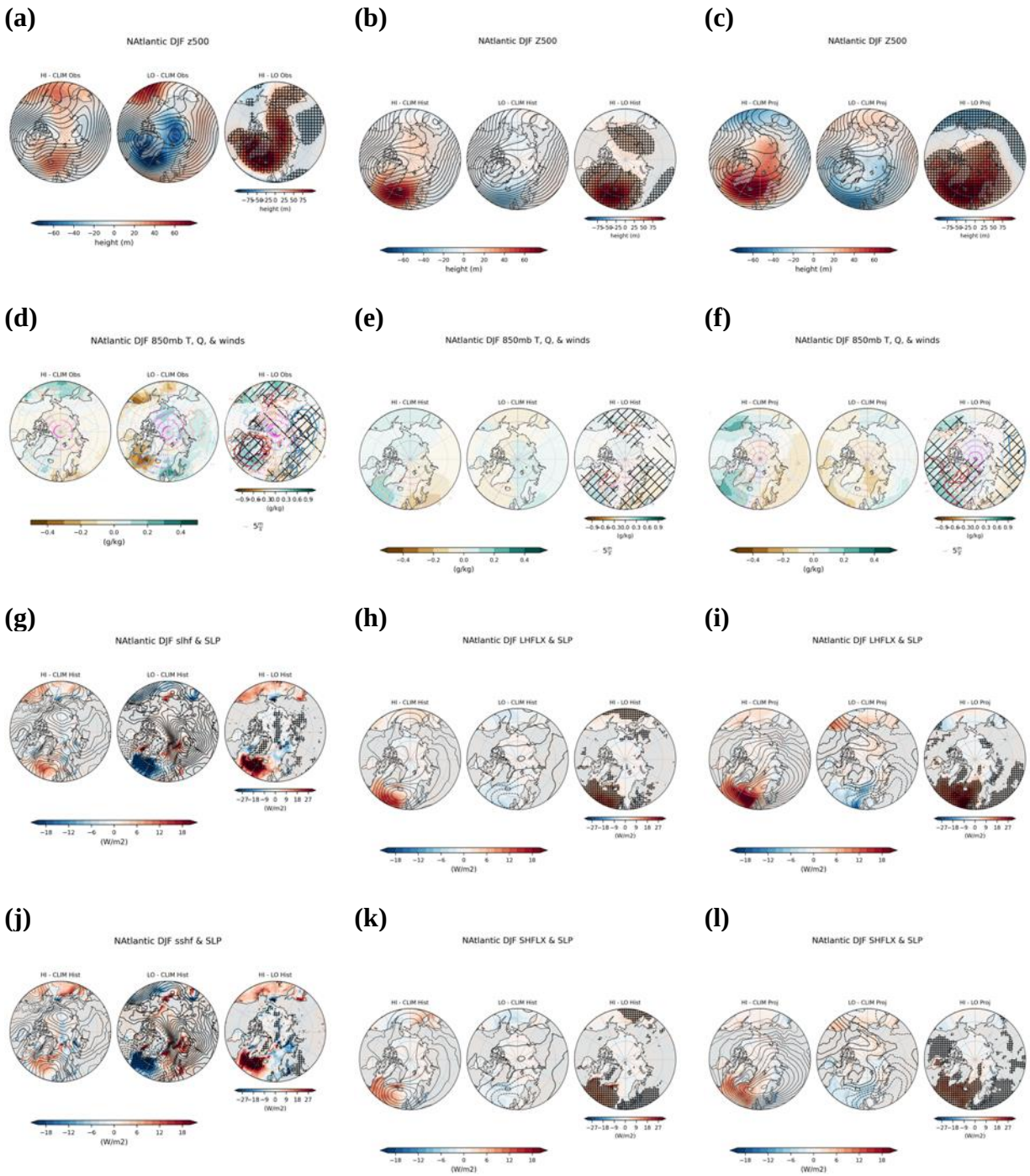

Figure 4.13. Same as Figures 4.11-4.12 but for North Atlantic DJF blocking.

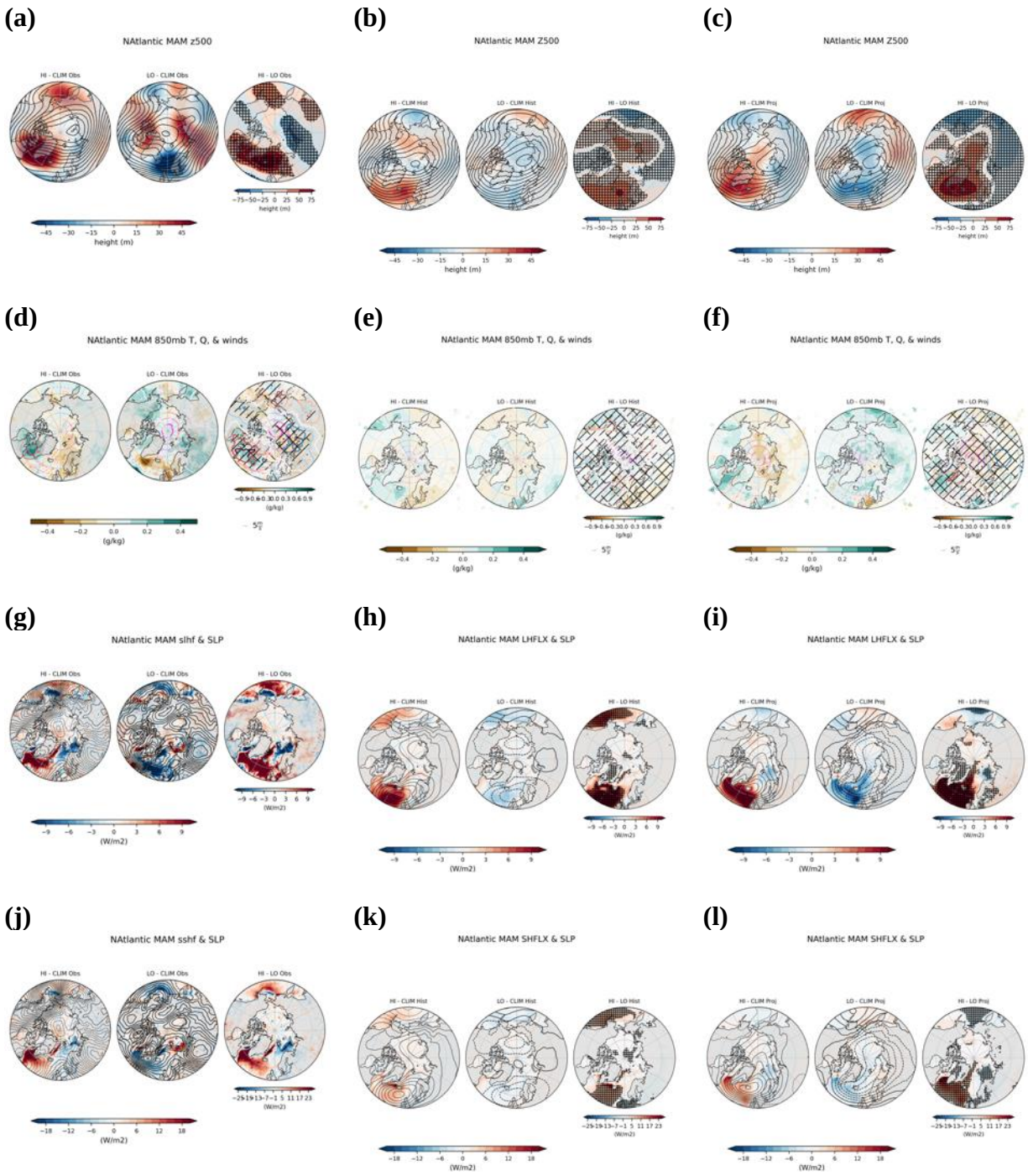

Figure 4.14. Same as Figures 4.11-4.13, but for North Atlantic MAM blocking.

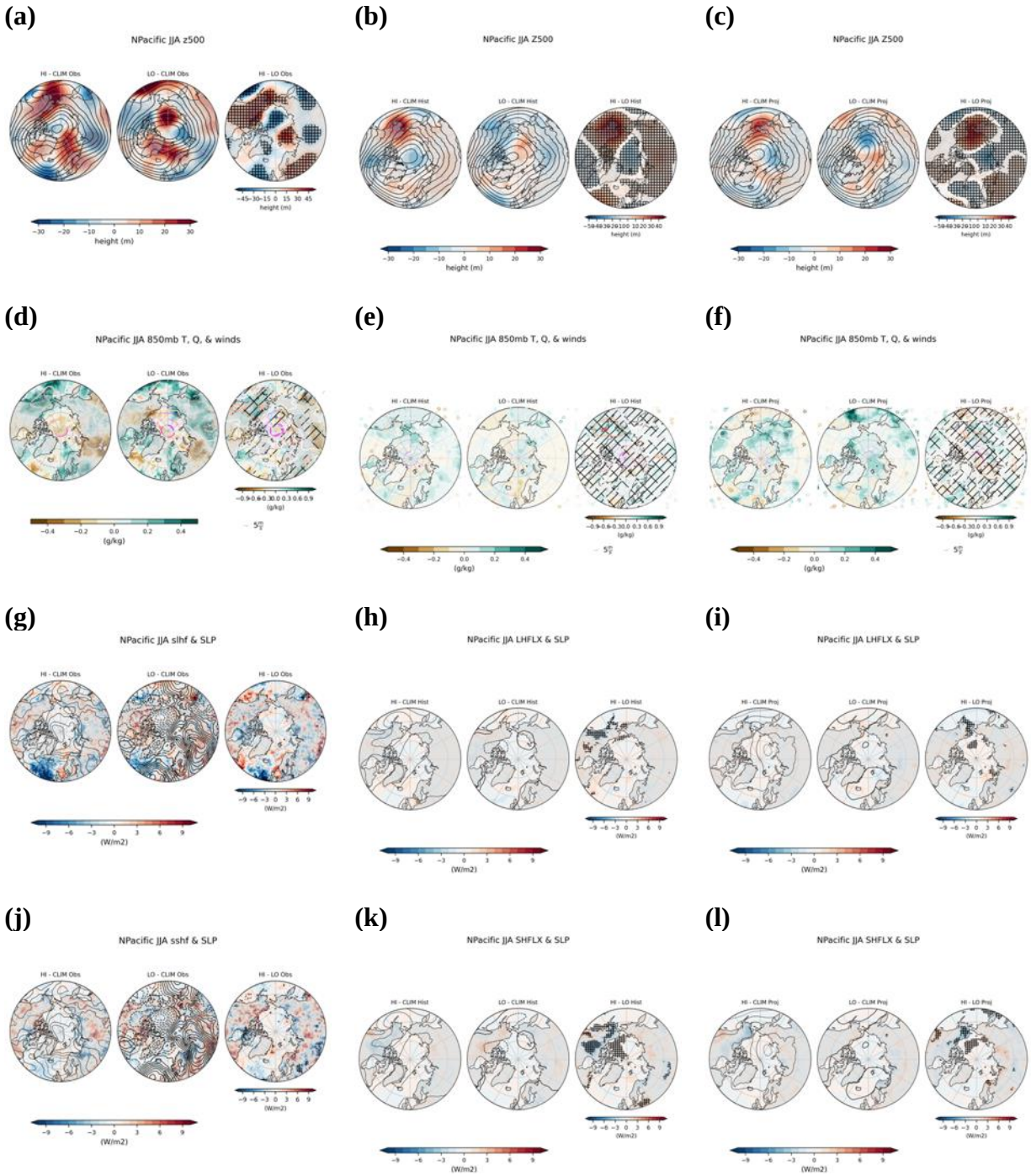

Figure 4.15. Same as Figure 4.11, but for North Pacific JJA blocking.

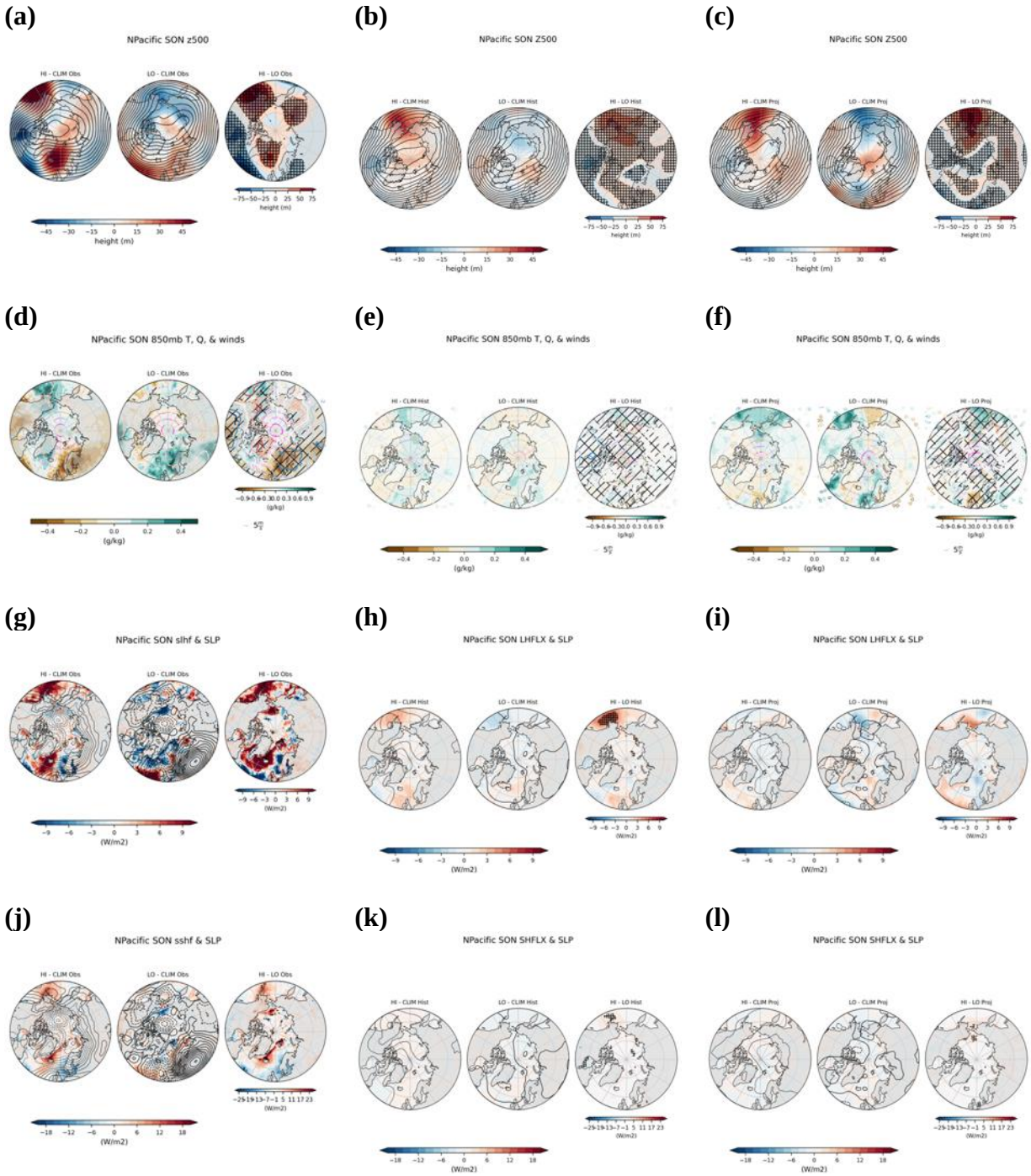

Figure 4.16. Same as Figure 4.15, but for SON blocking.

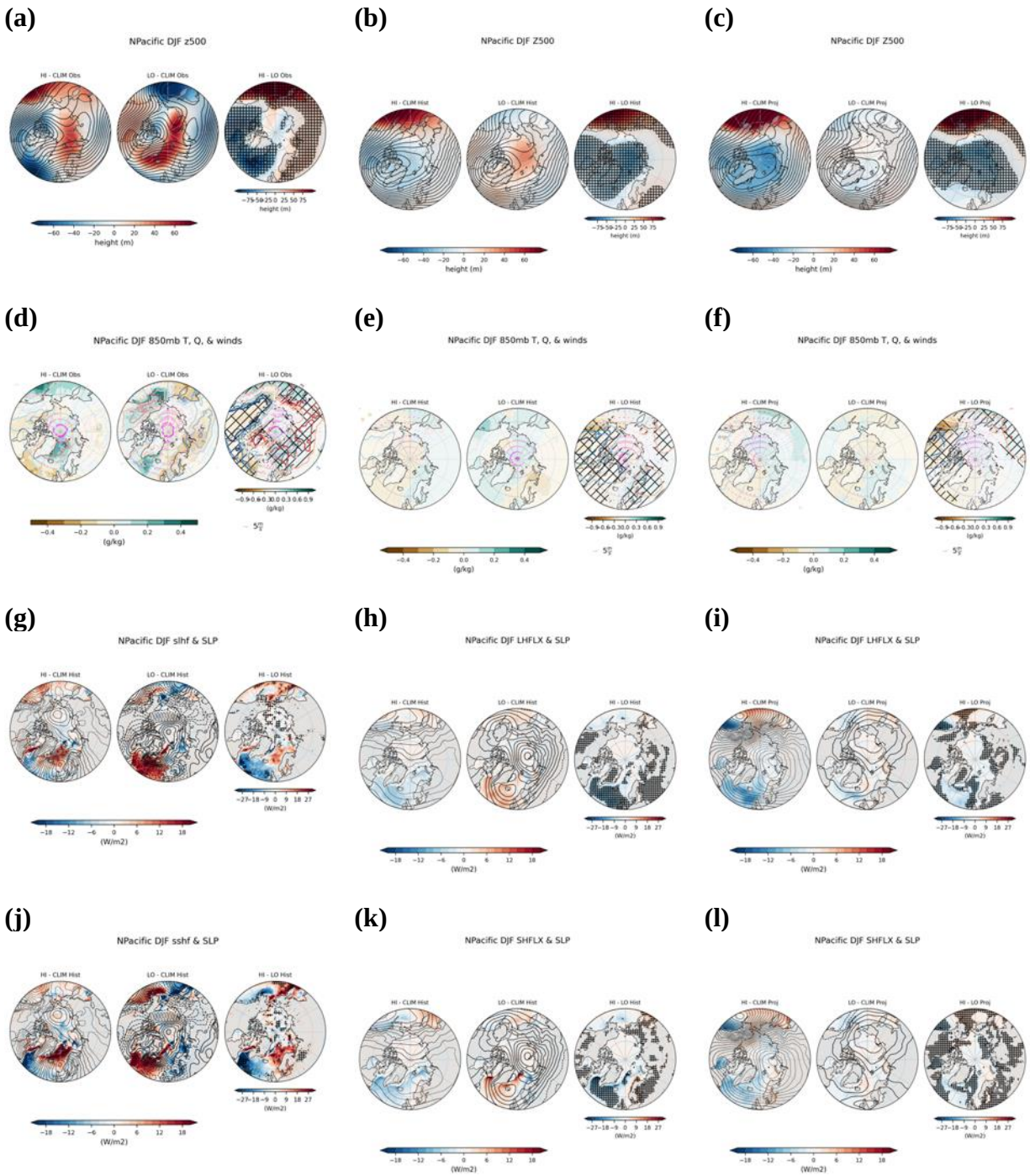

Figure 4.17. Same as Figures 4.15-4.16, but for DJF blocking.

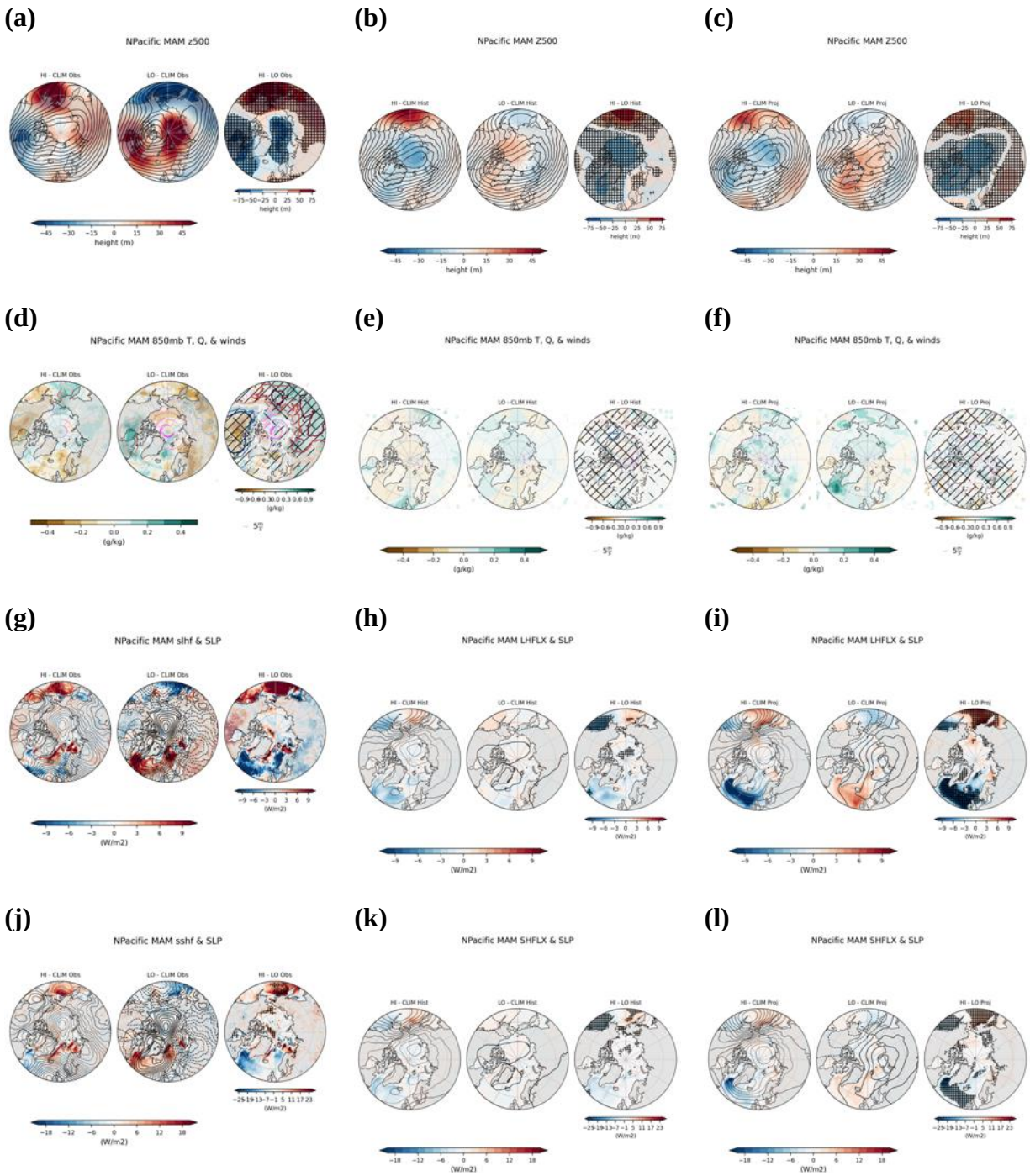

Figure 4.18. Same as Figures 4.15-4.17, but for MAM blocking.

CHAPTER 5

CONCLUSION

This dissertation connects tropical Pacific sea surface temperature (SST) variability and Arctic sea ice through the lens of synoptic-scale atmospheric blocking patterns. Past studies indicate significant increases in blocking activity predominantly over the North Atlantic and Greenland (e.g., Hanna et al., 2018a; Wachowicz et al., 2021), which contribute to increased heating and moisture transport into the region and consequential cryospheric impacts (e.g., Mattingly et al., 2018; Barrett et al., 2020; Preece et al., 2022). Many studies have attributed changes in atmospheric circulation in this region to variations in El Niño-Southern Oscillation (ENSO), particularly in summer. Furthermore, there has been limited work in teasing out these relationships in GCMs, as well as considering impacts beyond the winter and/or summer seasons. This research brings together observations and a GCM ensemble (CESM LENS) to assess historical and projected changes in high-latitude atmospheric blocking, including the tropical drivers of blocking and impacts on Arctic sea ice. This research increases our understanding of tropical-to-polar teleconnections, their contribution to Arctic amplification, and the representation of these processes in climate models, which will ultimately inform socioeconomic policies regarding climate change.

Manuscript 1 (Chapter 2) examines observed trends in blocking during the 1979–2018 period, particularly events with Rossby wave breaking, its connection to ENSO diversity and the overall impact on moisture transport in the North Atlantic and North Pacific. This chapter confirms the increase in summertime cyclonic wave breaking (CWB) and enhanced moisture

transport under Central Pacific (CP) El Niño events. The corresponding increase in moisture transport from CWB under CP El Niño conditions further align with previous research noting increases in summertime Greenland blocking, suggesting that possible links between tropical Pacific SST variability and ice loss in this region. Moreover, North Pacific blocking associated with RWB indicates more moisture transport under anticyclonic wave breaking (AWB), especially during summer CP El Niño conditions. While not explicitly assessed in this chapter, results of the greatest moisture transport occurring ahead of the wave break in both basins put forth a hypothesis of a possible connection between wave breaking and narrow plumes of extreme moisture transport known as "atmospheric rivers". Consequently, the results here illustrate the importance of considering tropical Pacific SST variability due to ENSO "diversity" in distributing high latitude moisture, particularly in the North Atlantic basin.

In the second manuscript (Chapter 3), the connection between ENSO diversity and Arctic sea ice is explored in both observations and in a GCM large ensemble dataset, CESM LENS, for the period of 1979–2018. The results from this chapter indicate observed regional sea ice varies based on ENSO type (CP or EP), though the extent of this is not captured by the CESM LENS dataset. In particular, observations show a 1-3 month lag in sea ice concentration response from winter sea surface temperature (SST) anomalies in the Beaufort Sea and Canadian Archipelago regions, with an immediate response in the Canadian Archipelago during the summer, particularly under CP ENSO conditions. As such, CP ENSO leads to sea ice in the Canadian Archipelago region to persist longer into the summer months, both confirming previous findings and motivating continued work to identify implications of increased regional sea ice on local hydroclimate. Furthermore, while reanalysis-based composites show shifts in atmospheric circulation and associated atmospheric conditions under CP and EP ENSO conditions, the

strength of these circulation anomalies and consequent sea ice responses appear severely underestimated in CESM LENS, leaving implications for long-term sea ice prediction.

The third and final manuscript (Chapter 4) addresses the gap in understanding historical blocking trends and observed sea ice impacts and compares with and assesses current projections of blocking and expected sea ice impacts in CESM LENS. A comparison of wave breaking-related blocking events (total of CWB and AWB) from Chapter 2 with historical (1979–2005) simulations of blocking in CESM LENS show relative agreement in CESM's ability to capture the climatological characteristics of blocking in both the North Atlantic and North Pacific sectors. JJA blocking activity in both sectors increases in CESM (exceeding 30% more blocking days). A novel contribution of this chapter shows that the projected increase in summer blocking is the result of more persistent events. On the other hand, DJF blocking is expecting to decrease by at least 10% in both sectors, where this decrease in the North Atlantic is further attributed to a decrease in blocking persistence. However, observed sea ice concentration during and following seasons of high blocking activity show varying degrees of sensitivity in timing, magnitude, and by region. Consequently, there is generally little agreement between observations and CESM historical simulations, with the exception of MAM and JJA blocking and sea ice in the North Atlantic. There is consistent agreement in placement of anticyclones in CESM and its associated turbulent heat fluxes compared to observations, particularly during MAM. Reduced MAM blocking in the North Atlantic may either promote sea ice growth or import sea ice into the region, whereas increased MAM blocking in the North Pacific may deplete sea ice. As such, how MAM blocking activity changes at the end of the 21st Century appears to play a role in determining springtime sea ice maximum. Meanwhile, more persistence JJA blocking in the North Atlantic may speed up sea ice loss in this region ahead of the future projections.

Altogether, the findings from this dissertation contribute to the ongoing understanding of observed and simulated remote contributions to Arctic amplification by examining the representation of remote drivers of sea ice loss within a well-known global climate model, CESM. The observed remote contributions of ENSO on Rossby wave breaking and associated moisture transport from Chapter 2 showcase the significant influence the tropical Pacific has over high-latitude hydroclimatology. Moreover, the results of Chapter 2 may be beneficial to high latitude atmospheric river-related literature, given the close connection of extreme moisture transport during the wave breaking itself. Ongoing studies have shown the impact of these mechanisms on sea ice, as reviewed in Chapter 1, where results from Chapter 3 further confirm tropical influences on sea ice, despite not being well-represented in climate models. As a result, despite some uncertainty in the representation of blocking in climate models, GCMs, like CESM, show promise in assisting the scientific community in quantifying future regional cryospheric impacts from tropical-Arctic teleconnections, particularly around the Canadian Archipelago region and North Atlantic, as demonstrated in Chapter 4, though the quantifying the magnitude of these impacts requires substantial model enhancements.

Overall, an increase in observed and projected summer blocking activity over the North Atlantic as a consequence of tropical CP sea surface temperature anomalies remains consistent with existing studies and highlights an immediate importance for improving climate models to better understand and estimate long-term cryospheric changes. Shifts in the global state of climate suggest more frequent CP El Niño events, where expected high latitude responses from CP El Niño events remain underestimated, given both blocking activity and ENSO diversity are not fully captured by the current state of CESM, as confirmed in this dissertation. More importantly the underestimation of the modeled sea ice sensitivity to ENSO in requires ongoing

work to improve model physics, including cloud and radiative processes, which may also alleviate uncertainty surrounding how CESM captures long-term blocking impacts on sea ice. With improvements to GCMs, like CESM, increased confidence regarding long-term impacts of internal climate variability and its contribution to Arctic amplification is likely, which will allow Arctic communities in adjacent regions to better mitigate climate risks from cryospheric loss.

REFERENCES

Ashok, K., S. Behera, S. Rao, H. Weng, and T. Yamagata, 2007: El Niño Modoki and its possible teleconnection. *Journal of Geophysical Research*, **112**, C11007, doi:10.1029/2006JC003798.

Athanasiadis, P. J., S. Yeager, Y. Kwon, A. Bellucci, D. W. Smith, and S. Tibaldi, 2020: Decadal predictability of North Atlantic blocking and the NAO. *NPJ Climate and Atmospheric Science*, **3**, 1-10, doi:10.1038/s41612-020-0120-6.

Baggett, C., S. Lee, and S. Feldstein, 2016: An Investigation of the Presence of Atmospheric Rivers over the North Pacific during Planetary-Scale Wave Life Cycles and Their Role in Arctic Warming. *Journal of the Atmospheric Sciences*, **73**, 4329-4347, doi:10.1175/JAS-D-16-0033.1.

Barnes, E. A., L. M. Polvani, 2015: CMIP5 Projections of Arctic Amplification, of the North American/North Atlantic Circulation, and of Their Relationship. *Journal of Climate*, **28**, 5255-5271, doi:10.1175/JCLI-D-14-00589.1.

Barnes, E., J. Slingo, and T. Woollings, 2012: A methodology for the comparison of blocking climatologies across indices, models and climate scenarios. *Climate Dynamics*, **38**, 2467-2481, doi:10.1007/s00382-011-1243-6.

Barrett, B. S., G. R. Henderson, E. McDonnell, M. Henry, and T. Mote, 2020: Extreme Greenland blocking and high-latitude moisture transport. *Atmospheric Science Letters*, **21**, e1002, doi:10.1002/asl.1002.

Bauer, H. -., V. Wulfmeyer, and L. Bengtsson, 2008: The representation of a synoptic-scale

weather system in a thermodynamically adjusted version of the ECHAM4 general circulation model. *Meteorology Atmospheric Physics*, **99**, 129-153, doi:10.1007/s00703-007-0275-2.

Bayr, T., M. Latif, D. Dommenget, C. Wengel, J. Harlaß, and W. Park, 2018: Mean-state dependence of ENSO atmospheric feedbacks in climate models. *Climate Dynamics*, **50**, 3171-3194, doi:10.1007/s00382-017-3799-2.

Belleflamme, A., X. Fettweis, and M. Erpicum, 2015: Recent summer Arctic atmospheric circulation anomalies in a historical perspective. *The Cryosphere*, **9**, 53-64, doi:10.5194/tc-9-53-2015.

Belleflamme, A., X. Fettweis, C. Lang, and M. Erpicum, 2013: Current and future atmospheric circulation at 500 hPa over Greenland simulated by the CMIP3 and CMIP5 global models. *Climate Dynamics*, **41**, 2061-2080, doi:10.1007/s00382-012-1538-2.

Biskaborn, B. K., S. L. Smith, J. Noetzli, H. Matthes, G. Vieira, D. A. Streletskiy, P. Schoeneich, V. E. Romanovsky, A. G. Lewkowicz, A. Abramov, M. Allard, J. Boike, W. L. Cable, H. H. Christiansen, R. Delaloye, B. Diekmann, D. Drozdov, B. Etzelmüller, G. Grosse, M. Guglielmin, T. Ingeman-Nielsen, K. Isaksen, M. Ishikawa, M. Johansson, H. Johannsson, A. Joo, D. Kaverin, A. Kholodov, P. Konstantinov, T. Kröger, C. Lambiel, J. Lanckman, D. Luo, G. Malkova, I. Meiklejohn, N. Moskalenko, M. Oliva, M. Phillips, M. Ramos, A. B. K. Sannel, D. Sergeev, C. Seybold, P. Skryabin, A. Vasiliev, Q. Wu, K. Yoshikawa, M. Zheleznyak, and H. Lantuit, 2019: Permafrost is warming at a global scale. *Nature Communications*, **10**, doi:10.1038/s41467-018-08240-4.

Bowley, K. A., J. R. Gyakum, and E. H. Atallah, 2019a: The role of dynamic tropopause Rossby wave breaking for synoptic-scale buildups in Northern Hemisphere zonal available

potential energy. *Monthly Weather Review*, **147**, 433-455, doi:10.1175/MWR-D-18-0143.1

Bowley, K. A., J. R. Gyakum, and E. H. Atallah, 2019b: A New Perspective toward Cataloging Northern Hemisphere Rossby Wave Breaking on the Dynamic Tropopause. *Monthly Weather Review*, **147**, 409-431, doi:10.1175/MWR-D-18-0131.1.

Cai, W., S. Borlace, M. Lengaigne, P. van Rensch, M. Collins, G. Vecchi, A. Timmermann, A. Santoso, M. J. McPhaden, L. Wu, M. H. England, G. Wang, E. Guilyardi, and F. Jin, 2014: Increasing frequency of extreme El Niño events due to greenhouse warming. *Nature Climate Change*, **4**, 111-116, doi:10.1038/nclimate2100.

Cai, W., G. Wang, B. Dewitte, L. Wu, A. Santoso, K. Takahashi, Y. Yang, A. Carréric, and M. J. McPhaden, 2018: Increased variability of eastern Pacific El Niño under greenhouse warming. *Nature*, **564**, 201-206, doi:10.1038/s41586-018-0776-9.

Capotondi, A., A. T. Wittenberg, M. Newman, E. Di Lorenzo, J. Yu, P. Braconnot, J. Cole, B. Dewitte, B. Giese, E. Guilyardi, F. Jin, K. Karnauskas, B. Kirtman, T. Lee, N. Schneider, Y. Xue, and S. Yeh, 2015: Understanding ENSO diversity: improved determination of ENSO predictability, teleconnections, and impacts requires a better understanding of event-to-event differences in ENSO spatial patterns and evolution. *Bulletin of the American Meteorological Society*, **96**, 921, doi:10.1175/BAMS-D-13-00117.1.

Capotondi, A., A. T. Wittenberg, J.-S. Kug, K. Takahashi, and M.J. McPhaden, 2020a: "ENSO diversity" in *El Niño Southern Oscillation in a changing climate*, 65-86, doi: 10.1002/9781119548164.ch4

Capotondi, A., C. Deser, A. S. Phillips, Y. Okumura, and S. M. Larson, 2020b: ENSO and Pacific Decadal Variability in the Community Earth System Model Version 2. *Journal of*

Advances in Modeling Earth Systems, **12**, e2019MS002022, doi:10.1029/2019MS002022.

Chen, X., D. Luo, 2017: Arctic sea ice decline and continental cold anomalies: Upstream and downstream effects of Greenland blocking. *Geophysical Research Letters*, **44**, 3411-3419, doi:10.1002/2016GL072387.

Cohen, J., X. Zhang, J. Francis, T. Jung, R. Kwok, J. Overland, T. J. Ballinger, U. S. Bhatt, H. W. Chen, D. Coumou, S. Feldstein, H. Gu, D. Handorf, G. Henderson, M. Ionita, M. Kretschmer, F. Laliberte, S. Lee, H. W. Linderholm, W. Maslowski, Y. Peings, K. Pfeiffer, I. Rigor, T. Semmler, J. Stroeve, P. C. Taylor, S. Vavrus, T. Vihma, S. Wang, M. Wendisch, Y. Wu, and J. Yoon, 2020: Divergent consensuses on Arctic amplification influence on midlatitude severe winter weather. *Nature Climate Change*, **10**, 20, doi: 10.1038/s41558-019-0662-y.

Cohen, J., J. A. Screen, J. C. Furtado, M. Barlow, D. Whittleston, D. Coumou, J. Francis, K. Dethloff, D. Entekhabi, J. Overland, and J. Jones, 2014: Recent Arctic amplification and extreme mid-latitude weather. *Nature Geoscience*, **7**, 627-637, doi:10.1038/ngeo2234.

Coumou, D., G. Di Capua, S. Vavrus, L. Wang, and S. Wang, 2018: The influence of Arctic amplification on mid-latitude summer circulation. *Nature Communications*, **9**, 1-12, doi:10.1038/s41467-018-05256-8.

D'Andrea, F., S. Tibaldi, M. Blackburn, G. Boer, M. Déqué, M. R. Dix, B. Dugas, L. Ferranti, T. Iwasaki, A. Kitoh, V. Pope, D. Randall, E. Roeckner, D. Strauss, W. Stern, H. Van den Dool, and D. Williamson, 1998: Northern Hemisphere atmospheric blocking as simulated by 15 atmospheric general circulation models in the period 1979–1988. *Climate Dynamics*, **14**, 385-407, doi:10.1007/s003820050230.

Dai, A., D. Luo, M. Song, and J. Liu, 2019: Arctic amplification is caused by sea-ice loss under increasing CO2. *Nature Communications*, **10**, 121, doi:10.1038/s41467-018-07954-9.

Dai, Y., B. Tan, 2019: Two Types of the Western Pacific Pattern, Their Climate Impacts, and the ENSO Modulations. *Journal of Climate*, **32**, 823-841, doi:10.1175/JCLI-D-17-0618.1.

Davini, P., F. D'Andrea, 2016: Northern Hemisphere Atmospheric Blocking Representation in Global Climate Models. *Journal of Climate*, **29**, 8823-8840, doi:10.1175/JCLI-D-16-0242.1.

Davini, P., F. D'Andrea, 2020: From CMIP3 to CMIP6: Northern Hemisphere Atmospheric Blocking Simulation in Present and Future Climate. *Journal of Climate*, **33**, 10021-10038, doi:10.1175/JCLI-D-19-0862.1.

DeRepentigny, P., A. Jahn, M. M. Holland, and A. Smith, 2020: Arctic Sea Ice in Two Configurations of the CESM2 During the 20th and 21st Centuries. *Journal of Geophysical Research Oceans*, **125**, e2020JC016133, doi:10.1029/2020JC016133.

Deser, C., I. R. Simpson, K. A. McKinnon, and A. S. Phillips, 2017: The Northern Hemisphere Extratropical Atmospheric Circulation Response to ENSO: How Well Do We Know It and How Do We Evaluate Models Accordingly? *Journal of Climate*, **30**, 5059-5082, doi:10.1175/JCLI-D-16-0844.1.

Ding, Q., A. Schweiger, M. L'Heureux, D. Battisti, S. Po-Chedley, N. Johnson, E. Blanchard-Wrigglesworth, K. Harnos, Q. Zhang, R. Eastman, and E. Steig, 2017: Influence of high-latitude atmospheric circulation changes on summertime Arctic sea ice. *Nature Climate Change*, **7**, 289-295, doi:10.1038/nclimate3241.

Ding, Q., J. M. Wallace, D. S. Battisti, E. J. Steig, A. J. E. Gallant, H. Kim, and L. Geng, 2014: Tropical forcing of the recent rapid Arctic warming in northeastern Canada and

Greenland. *Nature,* **509**, 209-212, doi:10.1038/nature13260.

Drouard, M., T. Woollings, D. MH Sexton, and C. F. McSweeney, 2021: Dynamical differences between short and long blocks in the Northern Hemisphere. *Journal of Geophysical Research: Atmospheres*, **126**, e2020JD034082, doi: 10.1029/2020JD034082.

Duan, L., L. Cao, and K. Caldeira, 2019: Estimating Contributions of Sea Ice and Land Snow to Climate Feedback. *Journal of Geophysical Research Atmospheres*, **124**, 199-208, doi:10.1029/2018jd029093.

Dunn-Sigouin, E., S. Son, 2013: Northern Hemisphere blocking frequency and duration in the CMIP5 models. *Journal of Geophysical Research Atmospheres*, **118**, 1179-1188, doi:10.1002/jgrd.50143.

DuVivier, A. K., M. M. Holland, J. E. Kay, S. Tilmes, A. Gettelman, and D. A. Bailey, 2020: Arctic and Antarctic Sea Ice Mean State in the Community Earth System Model Version 2 and the Influence of Atmospheric Chemistry. *Journal of Geophysical Research Oceans,* **125**, e2019JC015934, doi:10.1029/2019JC015934.

Fasullo, J. T., A. S. Phillips, and C. Deser, 2020: Evaluation of Leading Modes of Climate Variability in the CMIP Archives. *Journal of Climate,* **33**, 5527-5545, doi:10.1175/JCLI-D-19-1024.1.

Feldl, N., S. Po-Chedley, H. A. Singh, S. Hay, and P. J. Kushner, 2020: Sea ice and atmospheric circulation shape the high-latitude lapse rate feedback. *NPJ Climate and Atmospheric Science*, **3**, doi:10.1038/s41612-020-00146-7.

Feng, J., W. Chen, and Y. Li, 2017: Asymmetry of the winter extra-tropical teleconnections in the Northern Hemisphere associated with two types of ENSO. *Climate Dynamics*, **48**, 2135-2151, doi:10.1007/s00382-016-3196-2.

Fettweis, X., E. Hanna, C. Lang, A. Belleflamme, M. Erpicum, and H. Gallée, 2013: Brief communication: Important role of the mid-tropospheric atmospheric circulation in the recent surface melt increase over the Greenland ice sheet. *The Cryosphere,* **7**, 241-248, doi:10.5194/tc-7-241-2013.

Francis, J. A., S. J. Vavrus, 2015: Evidence for a wavier jet stream in response to rapid Arctic warming. *Environmental Research Letters*, **10**, 14005, doi:10.1088/1748-9326/10/1/014005.

Franzke, C., S. B. Feldstein, and S. Lee, 2011: Synoptic analysis of the Pacific–North American teleconnection pattern. *Quarterly Journal of the Royal Meteorological Society*, **137**, 329-346, doi:10.1002/qj.768.

Freund, M. B., B. J. Henley, D. J. Karoly, H. V. McGregor, N. J. Abram, and D. Dommenget, 2019: Higher frequency of Central Pacific El Niño events in recent decades relative to past centuries. *Nature Geoscience*, **12**, 450-455, doi:10.1038/s41561-019-0353-3.

Gettelman, A., C. Hannay, J. T. Bacmeister, R. B. Neale, A. G. Pendergrass, G. Danabasoglu, J. F. Lamarque, J. T. Fasullo, D. A. Bailey, D. M. Lawrence, and M. J. Mills, 2019: High climate sensitivity in the Community Earth System Model version 2 (CESM2). *Geophysical Research Letters*, **46**, 8329-8337, doi: 10.1029/2019GL083978.

Hanna, E., X. Fettweis, and R. J. Hall, 2018a: Brief Communication: Recent changes in summer Greenland blocking captured by none of the CMIP5 models. *The Cryosphere*, **12**, 3287-3292, doi:10.5194/tc-2018-91.

Hanna, E., R. J. Hall, T. E. Cropper, T. J. Ballinger, L. Wake, T. Mote, and J. Cappelen, 2018b: Greenland blocking index daily series 1851–2015: Analysis of changes in extremes and links with North Atlantic and UK climate variability and change. *International Journal of*

Climatology, **38**, 3546-3564, doi:10.1002/joc.5516.

Hegyi, B. M., P. C. Taylor, 2018: The Unprecedented 2016–2017 Arctic Sea Ice Growth Season: The Crucial Role of Atmospheric Rivers and Longwave Fluxes. *Geophysical Research Letters*, **45**, 5204-5212, doi:10.1029/2017GL076717.

Hersbach, H., Bell, B., Berrisford, P., Biavati, G., Horányi, A., Muñoz-Sabater, J., et al. (2018). ERA5 hourly data on pressure levels from 1979 to present [Dataset]. Copernicus Climate Change Service (C3S) Climate Data Store (CDS), https://doi.org/10.24381/cds.bd0915c6

Hersbach, H., B. Bell, P. Berrisford, S. Hirahara, A. Horányi, J. Muñoz-Sabater, J. Nicolas, C. Peubey, R. Radu, D. Schepers, A. Simmons, et al., 2020: The ERA5 global reanalysis. *Quarterly Journal of the Royal Meteorological Society*, **146**, 1999-2049.

Henderson, G. R., B. S. Barrett, L. J. Wachowicz, K. S. Mattingly, J. R. Preece, and T. L. Mote, 2021: Local and Remote Atmospheric Circulation Drivers of Arctic Change: A Review. *Frontiers in Earth Science*, **9**, doi:10.3389/feart.2021.709896.

Holland, M. M., L. Landrum, D. Bailey, and S. Vavrus, 2019: Changing Seasonal Predictability of Arctic Summer Sea Ice Area in a Warming Climate. *Journal of Climate*, **32**, 4963-4979, doi:10.1175/JCLI-D-19-0034.1.

Horwath, M., B. D. Gutknecht, A. Cazenave, H. K. Palanisamy, F. Marti, F. Paul, R. Le Bris et al., 2022: Global sea-level budget and ocean-mass budget, with a focus on advanced data products and uncertainty characterisation. *Earth System Science Data*, **14**, 411-447, doi: 10.5194/essd-14-411-2022.

Hoskins, B., T. Woollings, 2015: Persistent Extratropical Regimes and Climate Extremes. *Current Climate Change Reports*, **1**, 115-124, doi:10.1007/s40641-015-0020-8.

Hu, C., S. Yang, Q. Wu, Z. Li, J. Chen, K. Deng, T. Zhang, and C. Zhang, 2016: Shifting El

Nino inhibits summer Arctic warming and Arctic sea-ice melting over the Canada Basin. *Nature Communications*, **7**, 1-9, doi:10.1038/ncomms11721.

Huang, Y., X. Dong, D. A. Bailey, M. M. Holland, B. Xi, A. K. DuVivier, J.E. Kay, L. L. Landrum, and Y. Deng, 2019: Thicker clouds and accelerated Arctic sea ice decline: The atmosphere-sea ice interactions in spring. *Geophysical Research Letters*, **46**, 6980-6989, doi: 10.1029/2019GL082791.

Hwang, J., P. Martineau, S.-W. Son, T. Miyasaka, and H. Nakamura, 2020: The role of transient eddies in North Pacific blocking formation and its seasonality. *Journal of the Atmospheric Sciences*, **77**, 2453-2470, doi: 10.1175/JAS-D-20-0011.1.

Inoue, J., M. E. Hori, 2011: Arctic cyclogenesis at the marginal ice zone: A contributory mechanism for the temperature amplification? *Geophysical Research Letters*, **38**, L12502, doi:10.1029/2011GL047696.

Jiménez-Esteve, B., D. I. V. Domeisen, 2018: The Tropospheric Pathway of the ENSO–North Atlantic Teleconnection. *Journal of Climate*, **31**, 4563-4584, doi:10.1175/JCLI-D-17-0716.1.

Johansson, E., A. Devasthale, M. Tjernström, A. M. L. Ekman, and T. L'Ecuyer, 2017: Response of the lower troposphere to moisture intrusions into the Arctic. *Geophysical Research Letters*, **44**, 2527-2536, doi:10.1002/2017GL072687.

Kapsch, M., R. G. Graversen, and M. Tjernström, 2013: Springtime atmospheric energy transport and the control of Arctic summer sea-ice extent. *Nature Climate Change*, **3**, 744-748, doi:10.1038/nclimate1884.

Kapsch, M., R. G. Graversen, M. Tjernström, and R. Bintanja, 2016: The Effect of Downwelling Longwave and Shortwave Radiation on Arctic Summer Sea Ice. *Journal of Climate*, **29**,

1143-1159, doi:10.1175/JCLI-D-15-0238.1.

Kay, J. E., C. Deser, A. Phillips, A. Mai, C. Hannay, G. Strand, J. M. Arblaster, S. C. Bates, G. Danabasoglu, J. Edwards, M. Holland, P. Kushner, J. -. Lamarque, D. Lawrence, K. Lindsay, A. Middleton, E. Munoz, R. Neale, K. Oleson, L. Polvani, and M. Vertenstein, 2015: THE COMMUNITY EARTH SYSTEM MODEL (CESM) LARGE ENSEMBLE PROJECT. *Bulletin of the American Meteorological Society*, **96**, 1333-1350, doi:10.1175/BAMS-D-13-00255.1.

Kay, J. E., T. L'Ecuyer, A. Gettelman, G. Stephens, and C. O'Dell, 2008: The contribution of cloud and radiation anomalies to the 2007 Arctic sea ice extent minimum. *Geophysical Research Letters*, **35**, L08503, doi:10.1029/2008GL033451.

Kay, J. E., K. Raeder, A. Gettelman, and J. Anderson, 2011: The Boundary Layer Response to Recent Arctic Sea Ice Loss and Implications for High-Latitude Climate Feedbacks. *Journal of Climate*, **24**, 428-447, doi:10.1175/2010JCLI3651.1.

Kay, J. E., T. L'Ecuyer, H. Chepfer, N. Loeb, A. Morrison, and G. Cesana,, 2016: Recent Advances in Arctic Cloud and Climate Research, *Current Climate Change Reports*, **2**, 159–169, doi:10.1007/s40641-016-0051-9.

Kennedy, D., T. Parker, T. Woollings, B. Harvey, and L. Shaffrey, 2016: The response of high-impact blocking weather systems to climate change. *Geophysical Research Letters*, **43**, 7250-7258, doi:10.1002/2016GL069725.

Kim, H., B. Kim, 2017: Relative Contributions of Atmospheric Energy Transport and Sea Ice Loss to the Recent Warm Arctic Winter. *Journal of Climate*, **30**, 7441-7450, doi:10.1175/JCLI-D-17-0157.1.

Kim, J., K. Kim, 2020: Characteristics of stratospheric polar vortex fluctuations associated with

sea ice variability in the Arctic winter. *Climate Dynamics*, **54**, 3599-3611, doi:10.1007/s00382-020-05191-9.

Komatsu, K. K., V. A. Alexeev, I. A. Repina, and Y. Tachibana, 2018: Poleward upgliding Siberian atmospheric rivers over sea ice heat up Arctic upper air. *Scientific Reports*, **8**, 2872-15, doi:10.1038/s41598-018-21159-6.

Kwok, R., 2009: Outflow of Arctic Ocean Sea Ice into the Greenland and Barents Seas:1979-2007. *Journal of Climate*, **22**, 2438-2457, doi:10.1175/2008JCLI2819.1.

Kwon, Y.-O., A. Camacho, C. Martinez, and H. Seo, 2018: North Atlantic winter eddy-driven jet and atmospheric blocking variability in the Community Earth System Model version 1 Large Ensemble simulations. *Climate Dynamics*, **51**, 3275-3289, doi: 10.1007/s00382-018-4078-6.

Landrum, L., M. M. Holland, 2020: Extremes become routine in an emerging new Arctic. *Nature Climate Change*, **10**, 1108-1115, doi:10.1038/s41558-020-0892-z.

Lavers, D. A., F. M. Ralph, D. E. Waliser, A. Gershunov, and M. D. Dettinger, 2015: Climate change intensification of horizontal water vapor transport in CMIP5. *Geophysical Research Letters*, **42**, 5617-5625, doi:10.1002/2015GL064672.

Lee, T., M. J. McPhaden, 2010: Increasing intensity of El Niño in the central-equatorial Pacific. *Geophysical Research Letters*, **37**, doi:10.1029/2010GL044007.

Letterly, A., J. Key, and Y. Liu, 2016: The influence of winter cloud on summer sea ice in the Arctic, 1983-2013. *Journal of Geophysical Research Atmospheres*, **121**, 2178-2187, doi:10.1002/2015JD024316.

Li, Z., W. Zhang, M. F. Stuecker, H. Xu, F. Jin, and C. Liu, 2019: Different Effects of Two ENSO Types on Arctic Surface Temperature in Boreal Winter. *Journal of Climate*, **32**,

4943-4961, doi:10.1175/JCLI-D-18-0761.1.

Lim, Y., R. I. Cullather, S. M. J. Nowicki, and K. Kim, 2019: Inter-relationship between subtropical Pacific sea surface temperature, Arctic sea ice concentration, and North Atlantic Oscillation in recent summers. *Scientific Reports*, **9**, 3481, doi:10.1038/s41598-019-39896-7.

Lindsay, R., A. Schweiger, 2015: Arctic sea ice thickness loss determined using subsurface, aircraft, and satellite observations. *The Cryosphere*, **9**, 269-283, doi:10.5194/tc-9-269-2015.

Liptak, J., C. Strong, 2016: A modeling investigation of the Arctic sea ice-atmosphere feedback. *Climate Dynamics*, **47**, 2471-2480, doi:10.1007/s00382-016-2976-z.

Liu, C., E. A. Barnes, 2015: Extreme moisture transport into the Arctic linked to Rossby wave breaking. *Journal of Geophysical Research: Atmospheres*, **120**, 3774-3788, doi:10.1002/2014JD022796.

Liu, C., X. Ren, and X. Yang, 2014: Mean flow-storm track relationship and Rossby wave breaking in two types of El-Niño. *Advancements in Atmospheric Sciences*, **31**, 197-210, doi:10.1007/s00376-013-2297-7.

Luo, D., X. Chen, A. Dai, and I. Simmonds, 2018: Changes in Atmospheric Blocking Circulations Linked with Winter Arctic Warming: A New Perspective. *Journal of Climate*, **31**, 7661-7678, doi:10.1175/JCLI-D-18-0040.1.

Luo, D., X. Chen, J. Overland, I. Simmonds, Y. Wu, and P. Zhang, 2019: Weakened Potential Vorticity Barrier Linked to Recent Winter Arctic Sea Ice Loss and Midlatitude Cold Extremes. *Journal of Climate*, **32**, 4235-4261, doi:10.1175/JCLI-D-18-0449.1.

Maher, N., D. Matei, S. Milinski, and J. Marotzke, 2018: ENSO Change in Climate Projections:

Forced Response or Internal Variability? *Geophysical Research Letters*, **45**, 11,390-11,398, doi:10.1029/2018gl079764.

Masato, G., B. J. Hoskins, and T. J. Woollings, 2012: Wave-breaking characteristics of midlatitude blocking. *Quarterly Journal of the Royal Meteorological Society*, **138**, 1285-1296, doi:10.1002/qj.990.

Masato, G., B. J. Hoskins, and T. Woollings, 2013a: Wave-Breaking Characteristics of Northern Hemisphere Winter Blocking: A Two-Dimensional Approach. *Journal of Climate*, **26**, 4535-4549, doi:10.1175/JCLI-D-12-00240.1.

Masato, G., B. J. Hoskins, and T. Woollings, 2013b: Winter and Summer Northern Hemisphere Blocking in CMIP5 Models. *Journal of Climate*, **26**, 7044-7059, doi:10.1175/JCLI-D-12-00466.1.

Matsumura, S., Y. Kosaka, 2019: Arctic–Eurasian climate linkage induced by tropical ocean variability. *Nature Communications*, **10**, 1-8, doi:10.1038/s41467-019-11359-7.

Matsumura, S., K. Yamazaki, and K. Suzuki, 2021: Slow-down in summer warming over Greenland in the past decade linked to central Pacific El Niño. Communications Earth & Environment, **2**, 1-8, doi:10.1038/s43247-021-00329-x.

Mattingly, K. S., T. L. Mote, and X. Fettweis, 2018: Atmospheric River Impacts on Greenland Ice Sheet Surface Mass Balance. *Journal of Geophysical Research: Atmospheres*, **123**, 8538-8560, doi:10.1029/2018JD028714.

Mattingly, K. S., C. A. Ramseyer, J. J. Rosen, T. L. Mote, and R. Muthyala, 2016: Increasing water vapor transport to the Greenland Ice Sheet revealed using self-organizing maps. *Geophysical Research Letters*, **43**, 9250-9258, doi:10.1002/2016GL070424.

McIlhattan, E. A., J. E. Kay, and T. S. L'Ecuyer, 2020: Arctic clouds and precipitation in the

Community Earth System Model version 2. *Journal of Geophysical Research: Atmospheres*, **125**, e2020JD032521, doi: 10.1029/2020JD032521.

Michel, C., G. Rivière, 2011: The Link between Rossby Wave Breakings and Weather Regime Transitions. *Journal of the Atmospheric Sciences*, **68**, 1730-1748, doi:10.1175/2011JAS3635.1.

Mioduszewski, J. R., S. Vavrus, M. Wang, M. Holland, and L. Landrum, 2019: Past and future interannual variability in Arctic sea ice in coupled climate models. *The Cryosphere*, **13**, 113-124, doi:10.5194/tc-13-113-2019.

Meredith, M., M. Sommerkorn, S. Cassotta, C. Derksen, A. Ekaykin, A. Hollowed, G. Kofinas et. al., 2019: Polar Regions. Chapter 3, IPCC Special Report on the Ocean and Cryosphere in a Changing Climate.

Moon, T. A., M. L. Druckenmiller, and R. L. Thoman, Eds., 2021: Arctic Report Card 2021, https://doi.org/10.25923/5s0f-5163.

Moore, B. J., D. Keyser, and L. F. Bosart, 2019: Linkages between Extreme Precipitation Events in the Central and Eastern United States and Rossby Wave Breaking. *Monthly Weather Review*, **147**, 3327-3349, doi:10.1175/MWR-D-19-0047.1.

Morrison, A. L., J. E. Kay, W. R. Frey, H. Chepfer, and R. Guzman, 2019: Cloud response to Arctic sea ice loss and implications for future feedback in the CESM1 climate model. *Journal of Geophysical Research: Atmospheres*, **124**, 1003-1020, doi: 10.1029/2018JD029142.

Mortin, J., G. Svensson, R. G. Graversen, M. Kapsch, J. C. Stroeve, and L. N. Boisvert, 2016: Melt onset over Arctic sea ice controlled by atmospheric moisture transport. *Geophysical Research Letters*, **43**, 6636-6642, doi:10.1002/2016GL069330.

Mudryk, L. R., C. Derksen, S. Howell, F. Laliberté, C. Thackeray, R. Sospedra-Alfonso, V. Vionnet, P. J. Kushner, and R. Brown, 2018: Canadian snow and sea ice: historical trends and projections. *The Cryosphere*, **12**, 1157-1176, doi:10.5194/tc-12-1157-2018.

Murto, S., R. Caballero, G. Svensson, and L. Papritz, 2022: Interaction between Atlantic cyclones and Eurasian atmospheric blocking drives wintertime warm extremes in the high Arctic. *Weather and Climate Dynamics*, **3**, 21-44, doi: 10.5194/wcd-3-21-2022 .

Nabizadeh, E., P. Hassanzadeh, D. Yang, and E. A. Barnes, 2019: Size of the Atmospheric Blocking Events: Scaling Law and Response to Climate Change. *Geophysical Research Letters*, **46**, 13488-13499, doi:10.1029/2019gl084863.

Onarheim, I. H., T. Eldevik, L. H. Smedsrud, and J. C. Stroeve, 2018: Seasonal and Regional Manifestation of Arctic Sea Ice Loss. *Journal of Climate*, **31**, 4917-4932, doi:10.1175/jcli-d-17-0427.1.

Papritz, L., 2020: Arctic Lower-Tropospheric Warm and Cold Extremes: Horizontal and Vertical Transport, Diabatic Processes, and Linkage to Synoptic Circulation Features. *Journal of climate*, **33**, 993-1016, doi:10.1175/JCLI-D-19-0638.1.

Papritz, L. and E. Dunn-Sigouin, 2020: What configuration of the atmospheric circulation drives extreme net and total moisture transport into the Arctic? *Geophysical Research Letters*, **47**, 14, doi:10.1029/2020GL089769.

Park, H., S. Lee, S. Son, S. B. Feldstein, and Y. Kosaka, 2015a: The Impact of Poleward Moisture and Sensible Heat Flux on Arctic Winter Sea Ice Variability. *Journal of Climate*, **28**, 5030-5040, doi:10.1175/JCLI-D-15-0074.1.

Park, H., S. Lee, Y. Kosaka, S. Son, and S. Kim, 2015b: The Impact of Arctic Winter Infrared Radiation on Early Summer Sea Ice. *Journal of Climate*, **28**, 6281-6296,

doi:10.1175/JCLI-D-14-00773.1.

Payne, A. E., M.-E.Demory, L. R. Leung, A. M. Ramos, C. A. Shields, J. J. Rutz, N. Siler, G. Villarini, A. Hall, and F. M. Ralph, 2020: Responses and impacts of atmospheric rivers to climate change. *Nature Reviews Earth & Environment*, **1**, 143-157, doi: 10.1038/s43017-020-0030-5.

Pedersen, R. A., J. H. Christensen, 2019: Attributing Greenland Warming Patterns to Regional Arctic Sea Ice Loss. *Geophysical Research Letters*, **46**, 10495-10503, doi:10.1029/2019GL083828.

Peings, Y., J. Cattiaux, S. Vavrus, and G. Magnusdottir, 2017: Late Twenty-First-Century Changes in the Midlatitude Atmospheric Circulation in the CESM Large Ensemble. *Journal of Climate*, **30**, 5943-5960, doi:10.1175/JCLI-D-16-0340.1.

Pelly, J. L., B. J. Hoskins, 2003: A New Perspective on Blocking. *Journal of the Atmospheric Sciences*, **60**, 743-755, doi:ANPOB>2.0.CO;2.

Peng, G., W. N. Meier, 2018: Temporal and regional variability of Arctic sea-ice coverage from satellite data. *Annals of Glaciology*, **59**, 191-200, doi:10.1017/aog.2017.32.

Perovich, D., W. Meier, M. Tschudi, S. Farrell, S. Hendricks, S. Gerland, L. Kaleschke, R. Ricker, X. Tian-Kunze, M. Webster, and K. Wood, 2019: Sea Ice. Arctic Report Card 2019, J. Richter-Menge, M. L. Druckenmiller, and M. Jeffries, Eds., http://www.arctic.noaa.gov/Report-Card.

Pfahl, S., C. Schwierz, M. Croci-Maspoli, C. M. Grams, and H. Wernli, 2015: Importance of latent heat release in ascending air streams for atmospheric blocking. *Nature Geoscience*, **8**, 610-614, doi:10.1038/ngeo2487.

Phillips, A. S., C. Deser, and J. Fasullo, 2014: A New Tool for Evaluating Modes of Variability

in Climate Models. *EOS*, **95**, 453-455, doi: 10.1002/2014EO490002.

Pithan, F., T. Mauritsen, 2014: Arctic amplification dominated by temperature feedbacks in contemporary climate models. *Nature Geoscience*, **7**, 181-184, doi:10.1038/NGEO2071.

Preece, J. R., L. J. Wachowicz, T. L. Mote, M. Tedesco, and X. Fettweis, 2022: Summer Greenland Blocking Diversity and Its Impact on the Surface Mass Balance of the Greenland Ice Sheet. *Journal of Geophysical Research Atmospheres*, **127**, e2021JD035489, doi:10.1029/2021JD035489.

Riboldi, J., F.s Lott, F. d'Andrea, and G. Rivière, 2020: On the linkage between Rossby wave phase speed, atmospheric blocking, and Arctic amplification. *Geophysical Research Letters*, **47**, e2020GL087796, doi:10.1029/2020GL087796

Ronalds, B., E. Barnes, and P. Hassanzadeh, 2018: A barotropic mechanism for the response of jet stream variability to Arctic amplification and sea ice loss. *Journal of Climate*, **31**, 7069-7085, doi: 10.1175/JCLI-D-17-0778.1.

Rydsaa, J. H., R. G. Graversen, T. I. H. Heiskanen, and P. J. Stoll, 2021. Changes in atmospheric latent energy transport into the Arctic: Planetary versus synoptic scales. *Quarterly Journal of the Royal Meteorological Society*, **147**, 2281-2292, doi: 10.1002/qj.4022.

Ryoo, J.-M., Y. Kaspi, D. W. Waugh, G. N. Kiladis, D. E. Waliser, E. J. Fetzer, and J. Kim, 2013: Impact of Rossby Wave Breaking on U.S. West Coast Winter Precipitation during ENSO Events. *Journal of Climate*, **26**, 6360-6382, doi:10.1175/JCLI-D-12-00297.1.

Scaife, A. A., T. Woollings, J. Knight, G. Martin, and T. Hinton, 2010: Atmospheric Blocking and Mean Biases in Climate Models. *Journal of Climate*, **23**, 6143-6152, doi:10.1175/2010JCLI3728.1.

Schiemann, R., P. Athanasiadis, D. Barriopedro, F. Doblas-Reyes, K. Lohmann, M. J. Roberts,

D. V. Sein, C. D. Roberts, L. Terray, and P. L. Vidale, 2020: Northern Hemisphere blocking simulation in current climate models: evaluating progress from the Climate Model Intercomparison Project Phase 5 to 6 and sensitivity to resolution. *Weather and Climate Dynamics*, **1**, 277, doi: 10.5194/wcd-1-277-2020.

Schiemann, R., M. Demory, L. C. Shaffrey, J. Strachan, P. L. Vidale, M. S. Mizielinski, M. J. Roberts, M. Matsueda, M. F. Wehner, and T. Jung, 2017: The Resolution Sensitivity of Northern Hemisphere Blocking in Four 25-km Atmospheric Global Circulation Models. *Journal of Climate*, **30**, 337-358, doi:10.1175/jcli-d-16-0100.1.

Screen, J., T. Bracegirdle, and I. Simmonds, 2018: Polar Climate Change as Manifest in Atmospheric Circulation. *Current Climate Change Reports*, **4**, 383-395, doi:10.1007/s40641-018-0111-4.

Serreze, M., J. Francis, 2006: The Arctic Amplification Debate. *Climatic Change*, **76**, 241-264, doi:10.1007/s10584-005-9017-y.

Sheridan, S., C. C. Lee, 2012: Synoptic climatology and the analysis of atmospheric teleconnections. *Progress in Physical Geography*, **36**, 548-557, doi:10.1177/0309133312447935.

Simpson, I. R., J. Bacmeister, R. B. Neale, C. Hannay, A. Gettelman, R. R. Garcia, P. H. Lauritzen, D. R. Marsh, M. J. Mills, B. Medeiros, and J. H. Richter, 2020: An Evaluation of the Large-Scale Atmospheric Circulation and Its Variability in CESM2 and Other CMIP Models. *Journal of Geophysical Research Atmospheres*, **125**, e2020JD032835, doi:10.1029/2020JD032835.

Smedsrud, L. H., M. H. Halvorsen, J. C. Stroeve, R. Zhang, and K. Kloster, 2016: Fram Strait sea ice export variability and September Arctic sea ice extent over the last 80 years. *The*

Cryosphere, **11**, 65-79, doi:10.5194/tc-2016-79.

Smith, K. L., L. M. Polvani, and L. B. Tremblay, 2018: The Impact of Stratospheric Circulation Extremes on Minimum Arctic Sea Ice Extent. *Journal of Climate*, **31**, 7169-7183, doi:10.1175/JCLI-D-17-0495.1.

Steinfeld, D., S. Pfahl, 2019: The role of latent heating in atmospheric blocking dynamics: a global climatology. *Climate Dynamics*, **53**, 6159-6180, doi:10.1007/s00382-019-04919-6.

Stroeve, J. C., J. R. Mioduszewski, A. Rennermalm, L. N. Boisvert, M. Tedesco, and D. Robinson, 2017: Investigating the local-scale influence of sea ice on Greenland surface melt. *The Cryosphere*, **11**, 2363-2381, doi:10.5194/tc-11-2363-2017.

Stroeve, J., D. Notz, 2018: Changing state of Arctic sea ice across all seasons. *Environmental Research Letters*, **13**, 103001, doi:10.1088/1748-9326/aade56.

Strong, C., G. Magnusdottir, 2008: Tropospheric Rossby Wave Breaking and the NAO/NAM. *Journal of the Atmospheric Sciences*, **65**, 2861-2876, doi:10.1175/2008JAS2632.1.

Sun, L., C. Deser, and R. A. Tomas, 2015: Mechanisms of Stratospheric and Tropospheric Circulation Response to Projected Arctic Sea Ice Loss. *Journal of Climate*, **28**, 7824-7845, doi:10.1175/JCLI-D-15-0169.1.

Sussman, H. S., A. Raghavendra, P. E. Roundy, and A. Dai, 2020: Trends in northern midlatitude atmospheric wave power from 1950 to 2099. *Climate Dynamics*, **54**, 2903-2918.

Swenson, E. T., D. M. Straus, 2017: Rossby Wave Breaking and Transient Eddy Forcing during Euro-Atlantic Circulation Regimes. *Journal of the Atmospheric Sciences*, **74**, 1735-1755, doi:10.1175/JAS-D-16-0263.1.

Tachibana, Y., K. K. Komatsu, V. A. Alexeev, L. Cai, and Y. Ando, 2019: Warm hole in Pacific

Arctic sea ice cover forced mid-latitude Northern Hemisphere cooling during winter 2017-18. *Scientific Reports*, **9**, 5567-12, doi:10.1038/s41598-019-41682-4.

Taylor, P., B. Hegyi, R. Boeke, and L. Boisvert, 2018: On the Increasing Importance of Air-Sea Exchanges in a Thawing Arctic: A Review. *Atmosphere*, **9**, 41, doi:10.3390/atmos9020041.

Thackeray, C. W., A. Hall, 2019: An emergent constraint on future Arctic sea-ice albedo feedback. *Nature Climate Change*, **9**, 972-978, doi:10.1038/s41558-019-0619-1.

Topál, D., Q. Ding, J. Mitchell, I. Baxter, M. Herein, T. Haszpra, R. Luo, and Q. Li, 2020: An internal atmospheric process determining summertime Arctic sea ice melting in the next three decades: lessons learned from five large ensembles and multiple CMIP5 climate simulations. *Journal of Climate*, **33**, 7431-7454, doi: 10.1175/JCLI-D-19-0803.1.

Trenberth, K. E., 1997: The Definition of El Nino. *Bulletin of the American Meteorological Society*, **78**, 2771-2778, doi: 10.1175/1520-0477(1997)078%3C2771:TDOENO%3E2.0.CO;2.

Trusel, L. D., S. B. Das, M. B. Osman, M. J. Evans, B. E. Smith, X. Fettweis, J. R. McConnell, B. P. Y. Noel, and van den Broeke, Michiel R, 2018: Nonlinear rise in Greenland runoff in response to post-industrial Arctic warming. *Nature*, **564**, 104-108, doi:10.1038/s41586-018-0752-4.

Van Den Broeke, M. R., E. M. Enderlin, I. M. Howat, P. Kuipers Munneke, B. P. Y. Noël, Jan Van De Berg, W, E. Van Meijgaard, and B. Wouters, 2016: On the recent contribution of the Greenland ice sheet to sea level change. *The Cryosphere*, **10**, 1933-1946, doi:10.5194/tc-10-1933-2016.

Vavrus, S. J., F. Wang, J. E. Martin, J. A. Francis, Y. Peings, and J. Cattiaux, 2017: Changes in

North American Atmospheric Circulation and Extreme Weather. *Journal of Climate*, **30**, 4317-4333, doi:10.1175/JCLI-D-16-0762.1.

Wachowicz, L. J., J. R. Preece, T. L. Mote, B. S. Barrett, and G. R. Henderson, 2021: Historical trends of seasonal Greenland blocking under different blocking metrics. *International Journal of Climatology*, **41**, E3263-E3278, doi:10.1002/joc.6923.

Walsh, J. E., W. L. Chapman, F. Fetterer, and J. S. Stewart. 2019. Gridded Monthly Sea Ice Extent and Concentration, 1850 Onward, Version 2. [Indicate subset used]. Boulder, Colorado USA. NSIDC: National Snow and Ice Data Center. doi:10.7265/jj4s-tq79. [10 October 2020].

Wang, L., Z. Kuang, 2019: Evidence against a general positive eddy feedback in atmospheric blocking. arXiv preprint arXiv:1907.00999, doi:10.31223/OSF.IO/KMGQV.

Wernli, H., L. Papritz, 2018: Role of polar anticyclones and mid-latitude cyclones for Arctic summertime sea-ice melting. *Nature Geoscience*, **11**, 108-113, doi:10.1038/s41561-017-0041-0.

Wirth, V., M. Riemer, E. K. M. Chang, and O. Martius, 2018: Rossby wave packets on the midlatitude waveguide—A review. *Monthly Weather Review*, **146**, 1965-2001, doi: 10.1175/MWR-D-16-0483.1.

Woods, C., R. Caballero, 2016: The Role of Moist Intrusions in Winter Arctic Warming and Sea Ice Decline. *Journal of Climate*, **29**, 4473-4485, doi:10.1175/JCLI-D-15-0773.1.

Woods, C., R. Caballero, and G. Svensson, 2013: Large-scale circulation associated with moisture intrusions into the Arctic during winter. *Geophysical Research Letters*, **40**, 4717-4721, doi:10.1002/grl.50912.

Woods, C., R. Caballero, and G. Svensson, 2017: Representation of Arctic Moist Intrusions in

CMIP5 Models and Implications for Winter Climate Biases. *Journal of Climate*, **30**, 4083-4102, doi:10.1175/JCLI-D-16-0710.1.

Woollings, T., B. Hoskins, M. Blackburn, and P. Berrisford, 2008: A New Rossby Wave–Breaking Interpretation of the North Atlantic Oscillation. *Journal of the Atmospheric Sciences*, **65**, 609-626, doi:10.1175/2007JAS2347.1.

Woollings, T., E. Barnes, B. Hoskins, Y. Kwon, R. W. Lee, C. Li, E. Madonna, M. McGraw, T. Parker, R. Rodrigues, C. Spensberger, and K. Williams, 2018a: Daily to Decadal Modulation of Jet Variability. *Journal of Climate*, **31**, 1297-1314, doi:10.1175/JCLI-D-17-0286.1.

Woollings, T., D. Barriopedro, J. Methven, S. Son, O. Martius, B. Harvey, J. Sillmann, A. Lupo, and S. Seneviratne, 2018b: Blocking and its Response to Climate Change. *Current Climate Change Reports*, **4**, 287-300, doi:10.1007/s40641-018-0108-z.

Yang, M., D. Luo, W. Shi, Y. Yao, X. Li, and X. Chen,2021: Contrasting interannual impacts of European and Greenland blockings on the winter North Atlantic storm track. *Environmental Research Letters*, **16**, 104036, doi: 10.1088/1748-9326/ac2934.

Yang, W., G. Magnusdottir, 2017: Springtime extreme moisture transport into the Arctic and its impact on sea ice concentration. *Journal of Geophysical Research: Atmospheres*, **122**, 5316-5329, doi:10.1002/2016JD026324.

Yang, W., G. Magnusdottir, 2018: Year-to-year Variability in Arctic Minimum Sea Ice Extent and its Preconditions in Observations and the CESM Large Ensemble Simulations. *Scientific Reports*, **8**, 9070-7, doi:10.1038/s41598-018-27149-y.

Ye, K. and T. Jung, 2019: How Strong Is Influence of the Tropics and Midlatitudes on the Arctic Atmospheric Circulation and Climate Change? *Geophysical Research Letters*, **46**, 4942-

4952, doi:10.1029/2019GL082391.

Yeh, S., J. Kug, B. Dewitte, M. Kwon, B. P. Kirtman, and F. Jin, 2009: El Niño in a changing climate. *Nature*, **461**, 511-514, doi:10.1038/nature08316.

You, C., M. Tjernström, A. Devasthale, and D. Steinfeld, 2022: The Role of Atmospheric Blocking in Regulating Arctic Warming. *Geophysical Research Letters*, **49**, doi:10.1029/2022gl097899.

Yuan, X., M. R. Kaplan, and M. A. Cane, 2018: The Interconnected Global Climate System—A Review of Tropical–Polar Teleconnections. *Journal of Climate*, **31**, 5765-5792, doi:10.1175/JCLI-D-16-0637.1.

Zappa, G., L. C. Shaffrey, and K. I. Hodges, 2013: The Ability of CMIP5 Models to Simulate North Atlantic Extratropical Cyclones. *Journal of Climate*, **26**, 5379-5396, doi:10.1175/JCLI-D-12-00501.1.

Zhang, G., Z. Wang, 2018: North Atlantic Extratropical Rossby Wave Breaking during the Warm Season: Wave Life Cycle and Role of Diabatic Heating. *Monthly Weather Review*, **146**, 695-712, doi:10.1175/MWR-D-17-0204.1.

Zhang, W., Z. Wang, M. Stuecker, A. Turner, F. Jin, and X. Geng, 2019: Impact of ENSO longitudinal position on teleconnections to the NAO. *Climate Dynamics*, **52**, 257-274, doi:10.1007/s00382-018-4135-1.

Zhang, J., R. Lindsay, M. Steele, and A. Schweiger, 2008: What drove the dramatic retreat of arctic sea ice during summer 2007? *Geophysical Research Letters*, **35**, L11505, doi:10.1029/2008GL034005.

Zheng, X., C. Hui, and S. Yeh, 2017: Response of ENSO amplitude to global warming in CESM large ensemble: uncertainty due to internal variability. *Climate Dynamics*, **50**, 4019-4035,

doi:10.1007/s00382-017-3859-7.

APPENDIX A

SUPPLEMENTARY FIGURES FOR CHAPTER 3

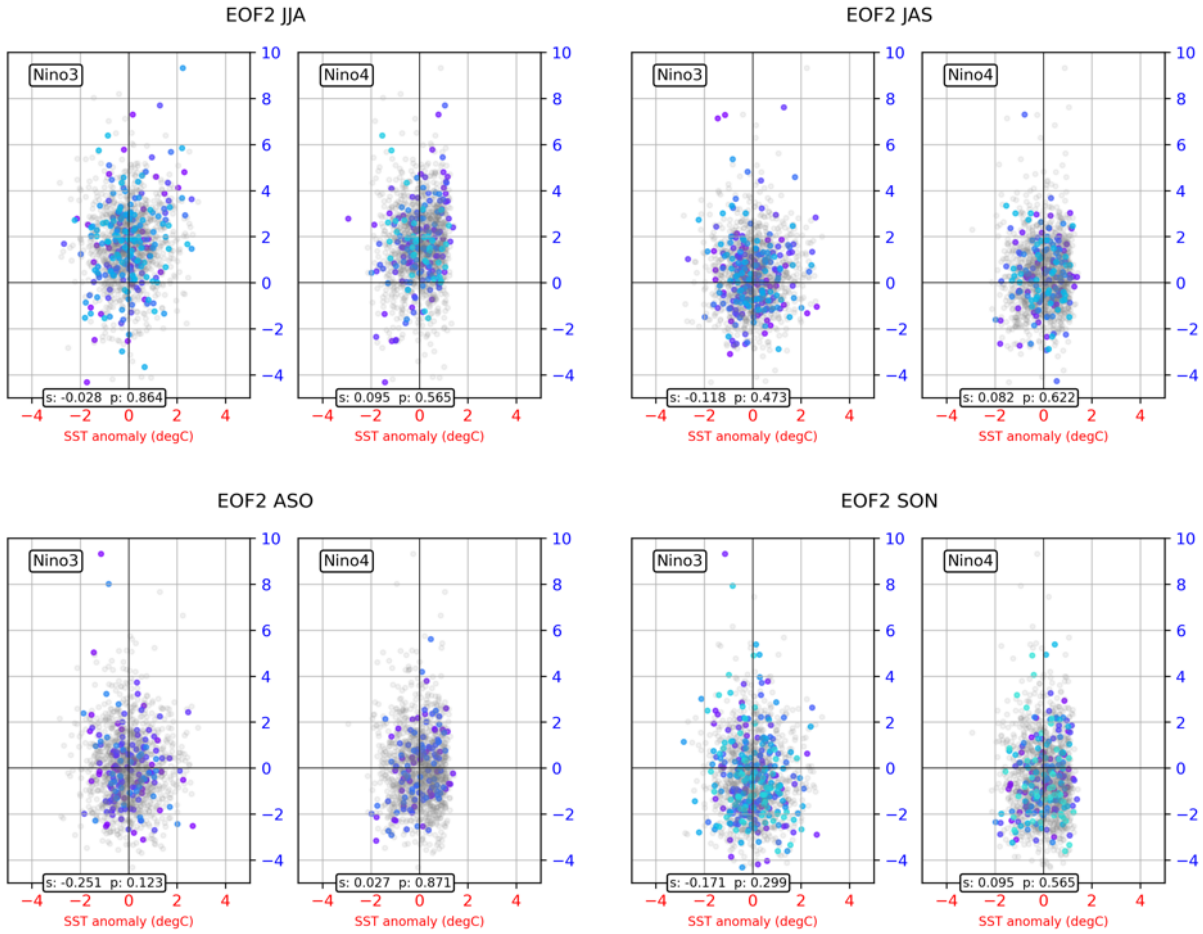

Figure A1. Scatterplots of seasonal sea ice EOF2 and SSTs in Nino3 and Nino4 regions for all ensembles. Single ensemble members with statistically significant correlation ($p < 0.1$) are colored; non-significant correlations are displayed in gray. Correlations (s) and p-values (p) across all ensembles are included.

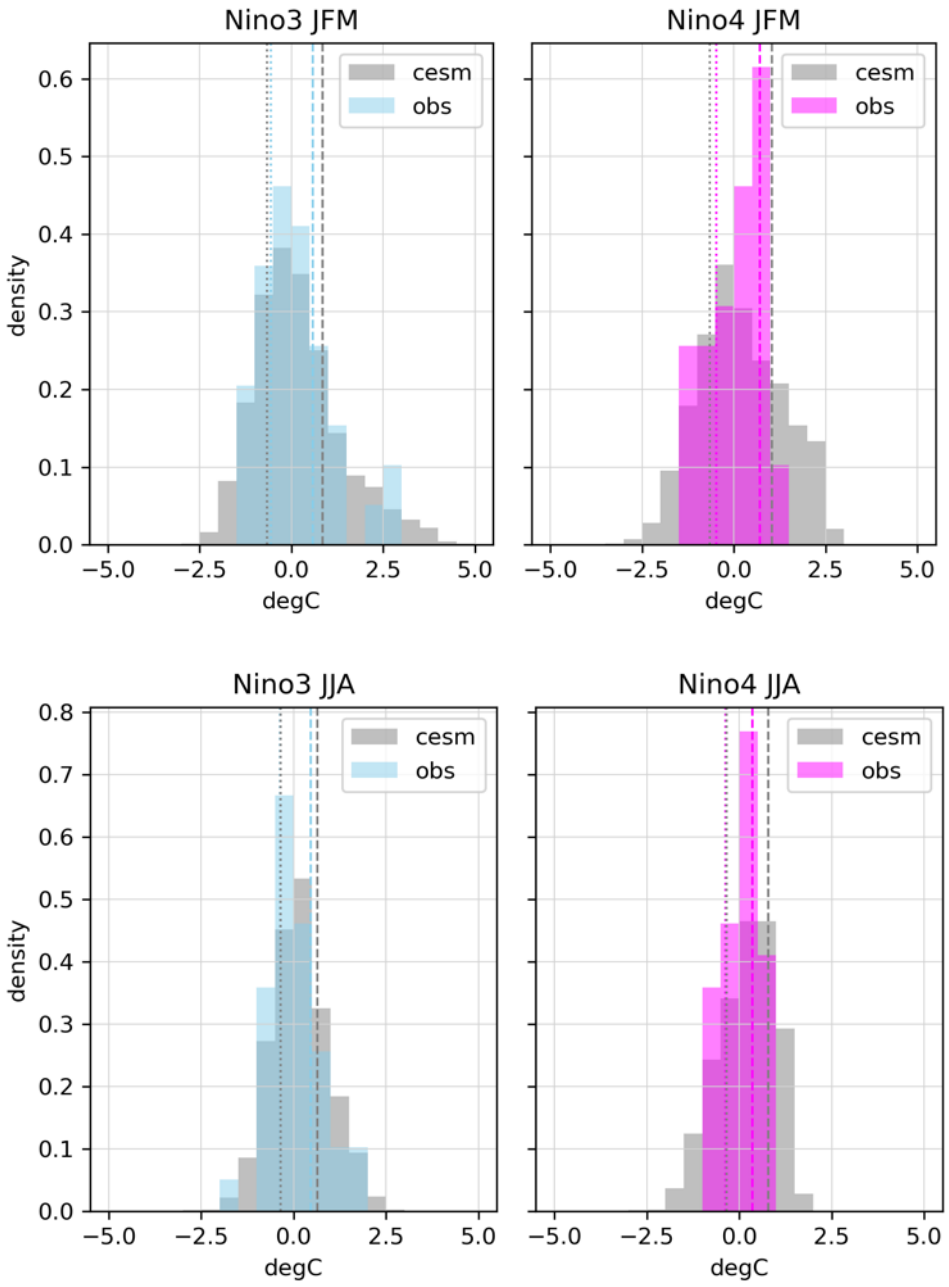

Figure A2. Both observation and CESM LE seasonal SST averages for 1920-2018 from the CVDP SST calculations. Distributions include only seasonal averages from 1979-2017. The 25th percentile value is denoted by the dotted lines; the 75th percentile is denoted by the dashed lines. Note, the percentiles are shown for considering all CESM seasons to compare to observations, and not by individual ensemble season (as used to composite).

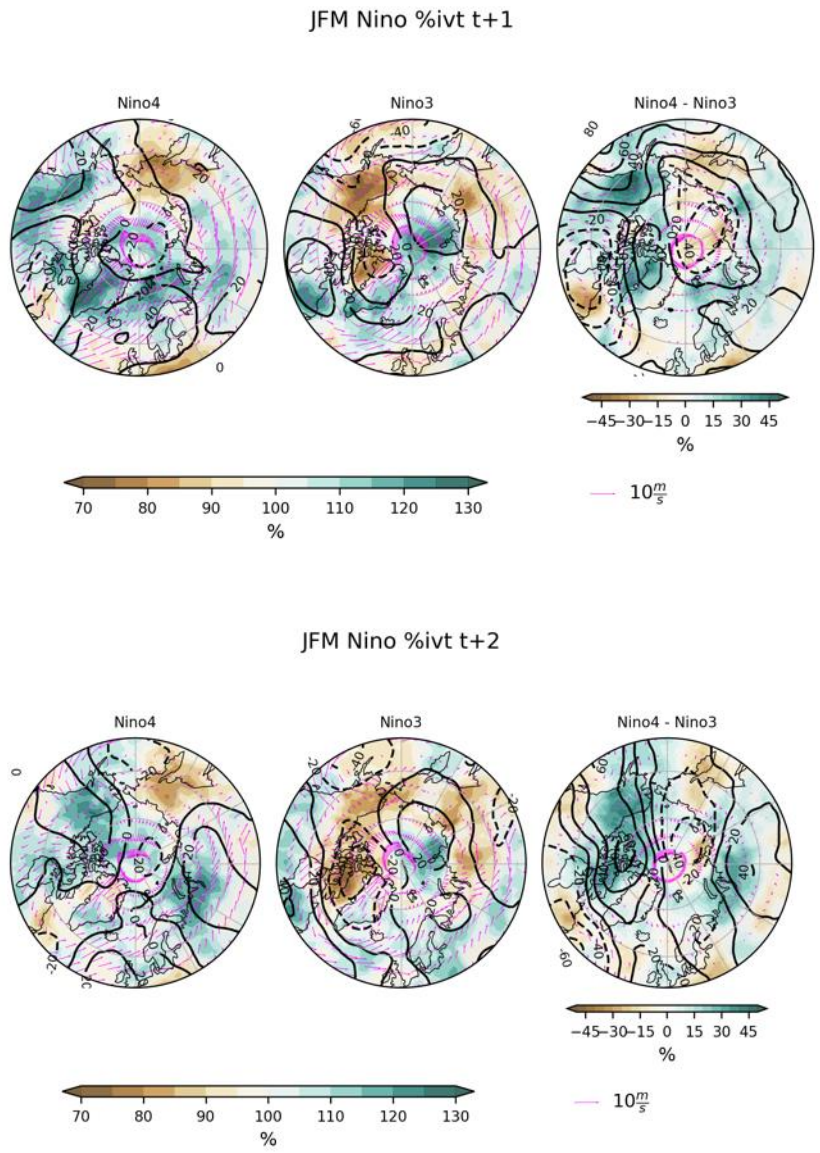

Figure A3. Lagged composites of the atmosphere for JFM Niño conditions only for FMA (top) and MAM (bottom), similar to Figure 3.11.

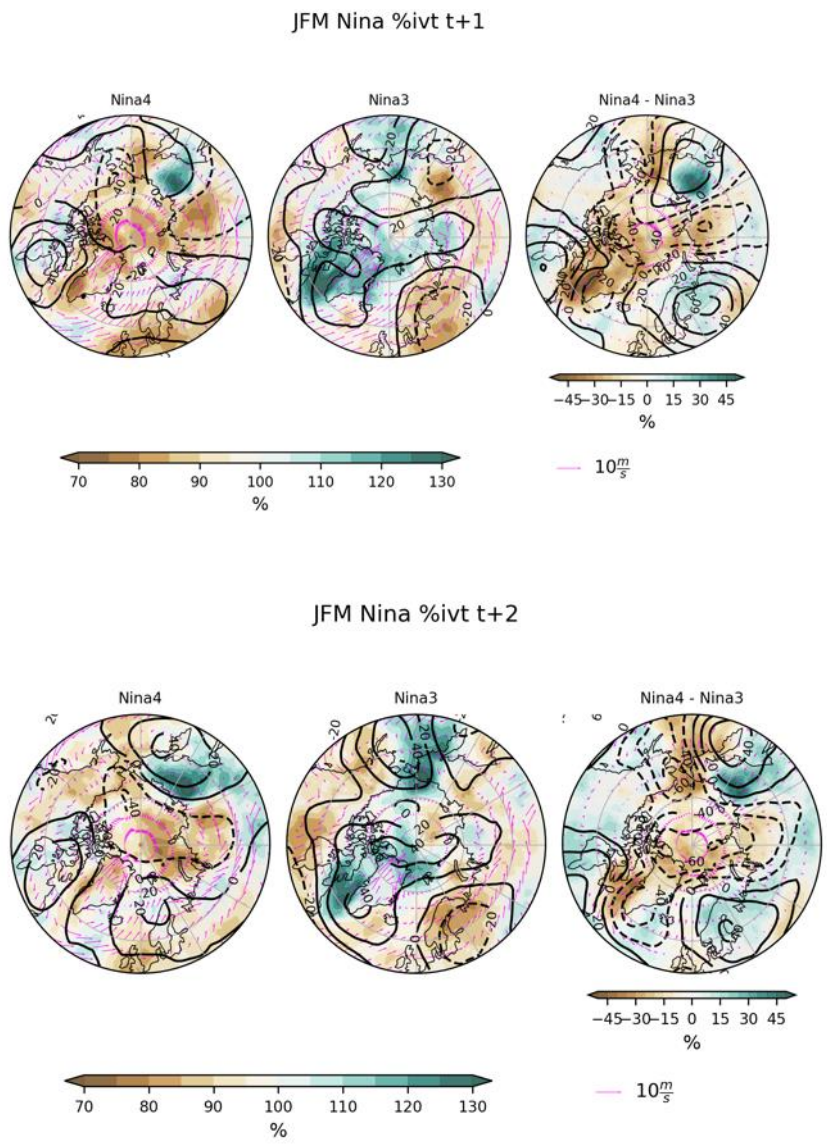

Figure A4. Same as Figure A3, but for Niña conditions.

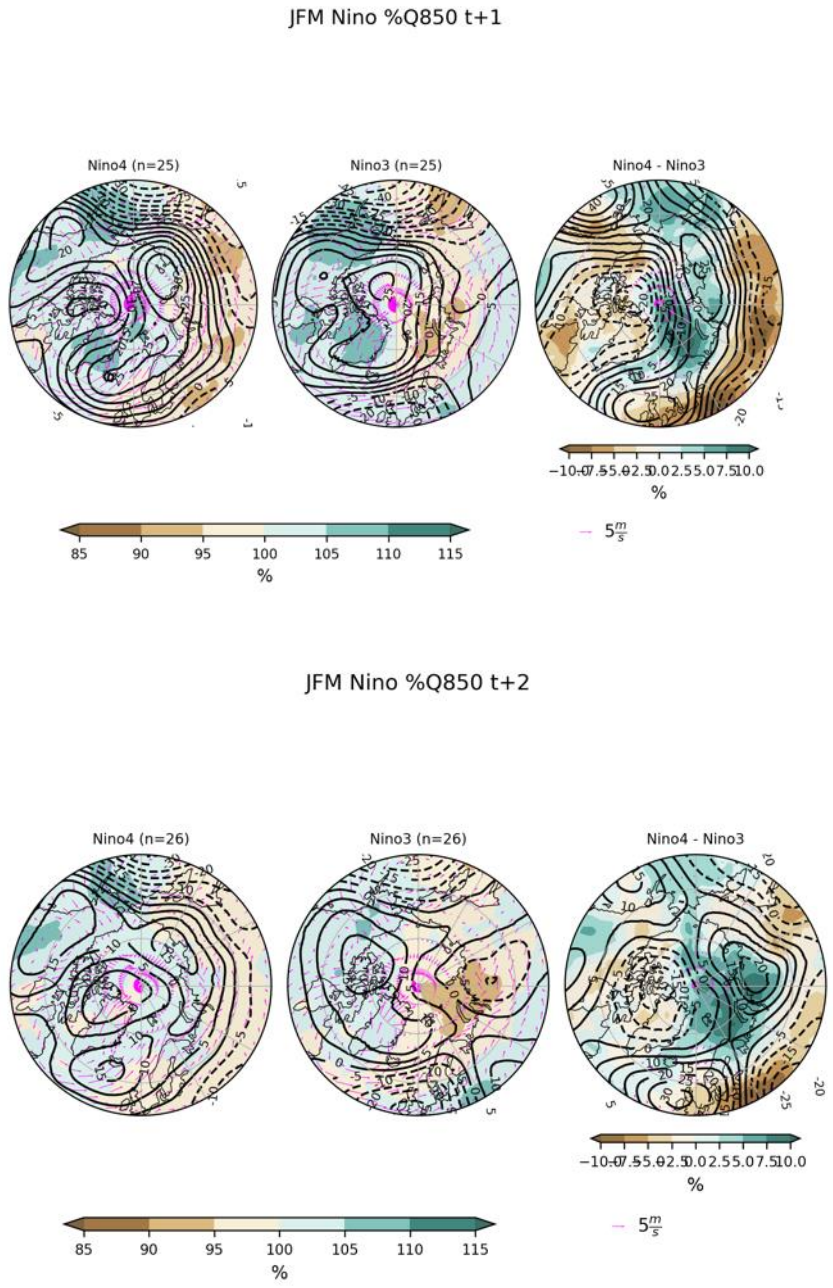

Figure A5. Lagged circulation anomalies following JFM Niño SST anomalies in CESM for FMA (top) and MAM (bottom).

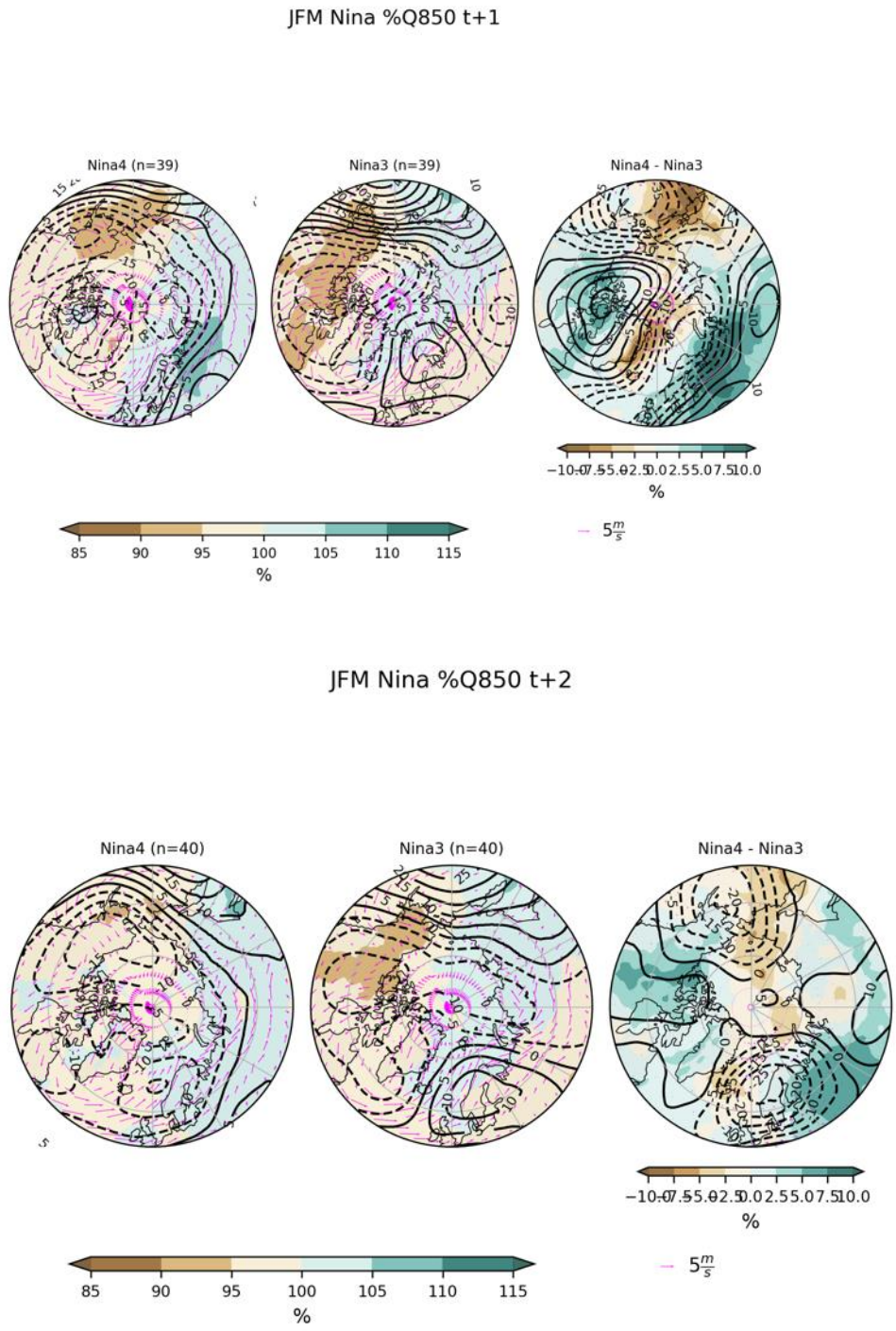

Figure A6. Lagged composites following JFM Niña anomalies only in CESM, similar to Figure A5.

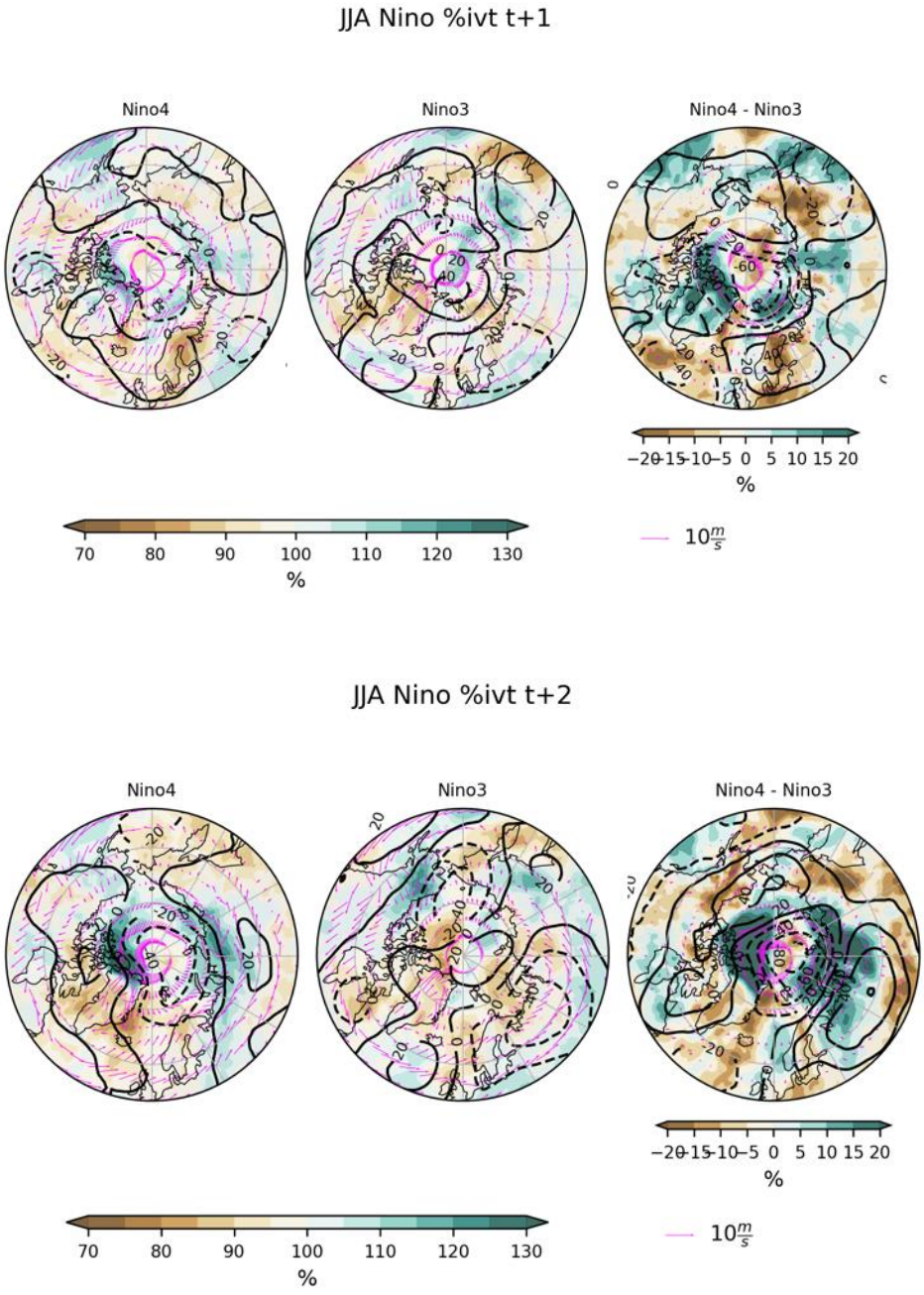

Figure A7. Lagged composites for JJA SST anomalies associated with Niño using ERA5, similar to Figure A3.

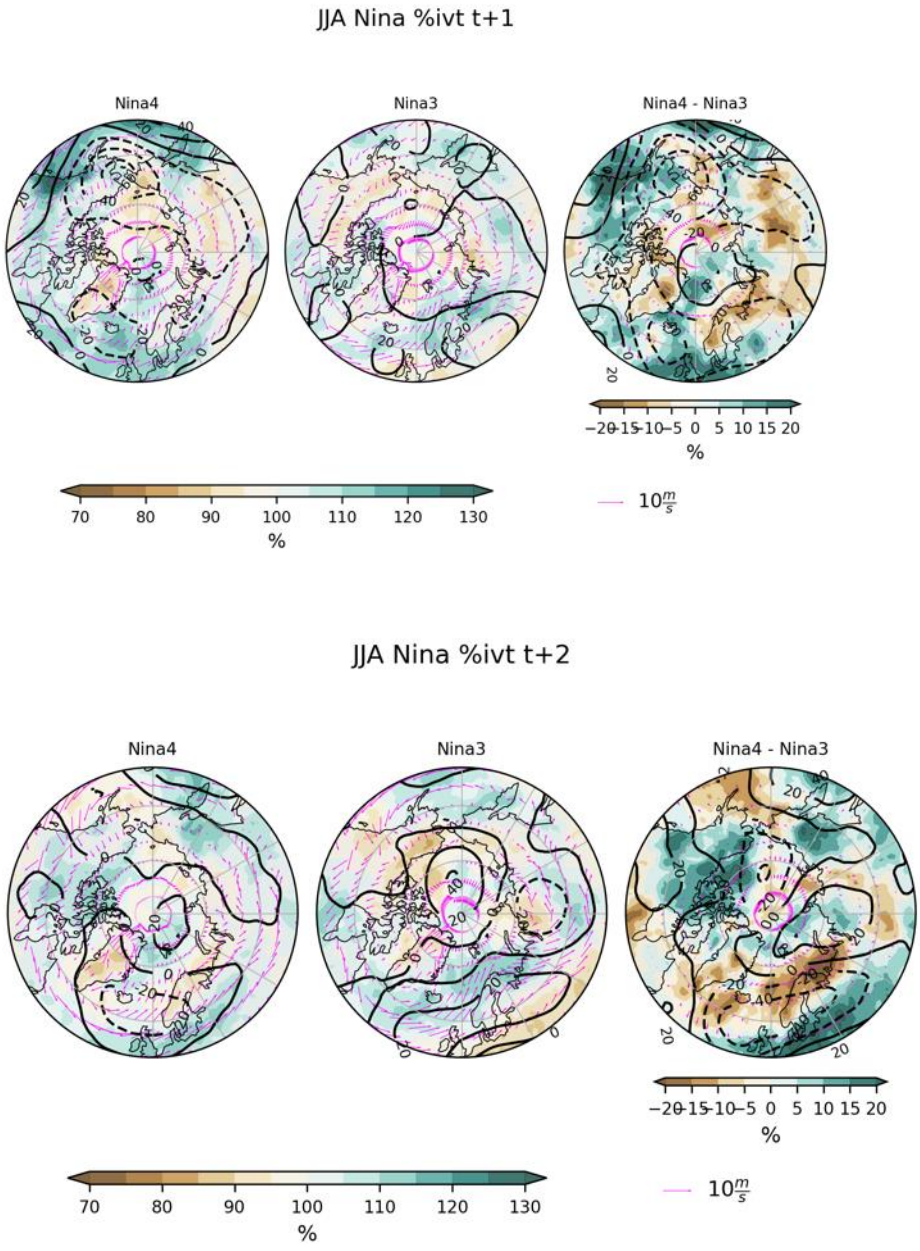

Figure A8. Similar to Figure A7, but for Niña conditions only.

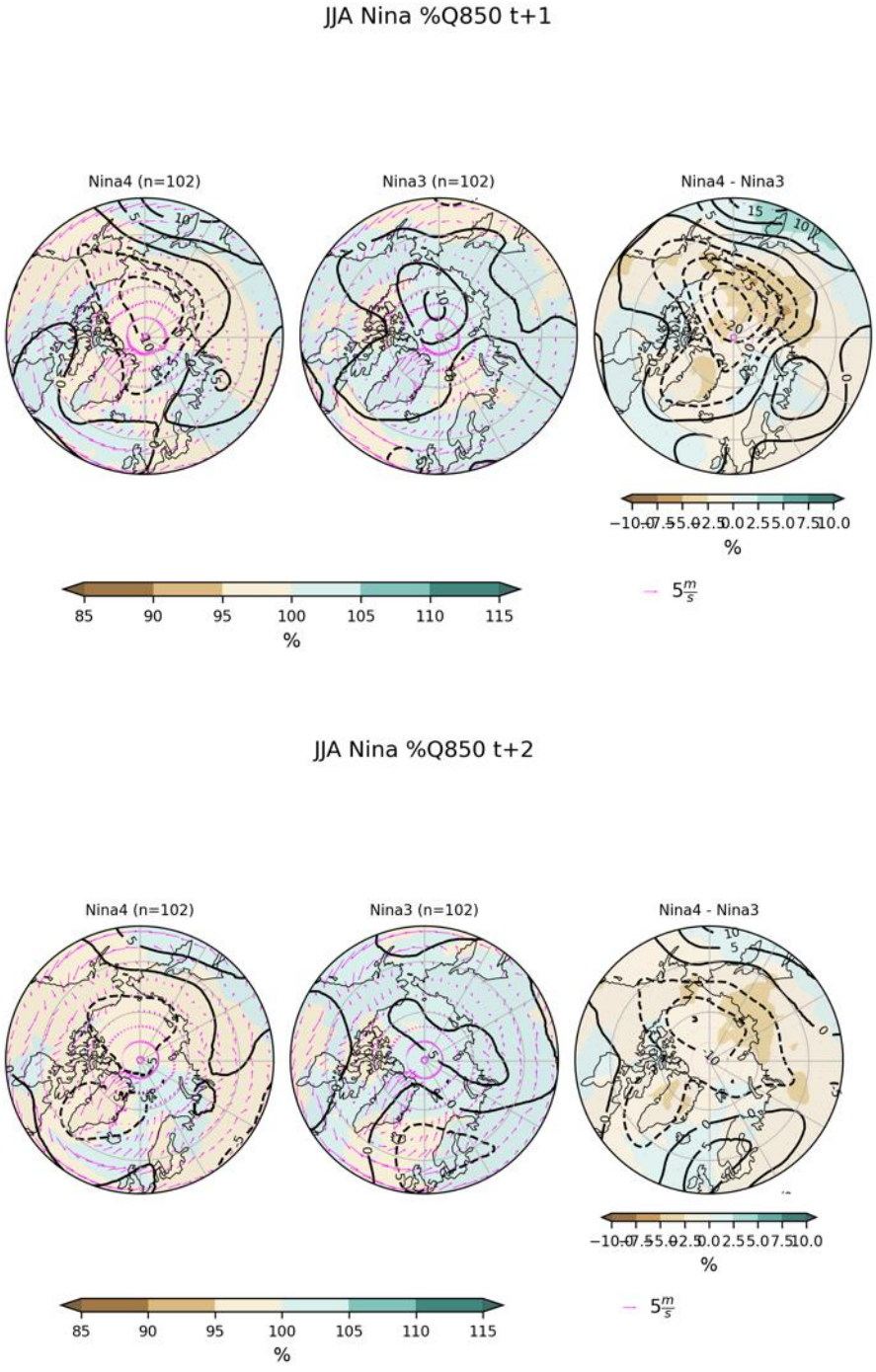

Figure A9. Same as Figure A6, but for JJA SST Niña anomalies in CESM for JAS (top) and ASO (bottom) atmospheric circulation.

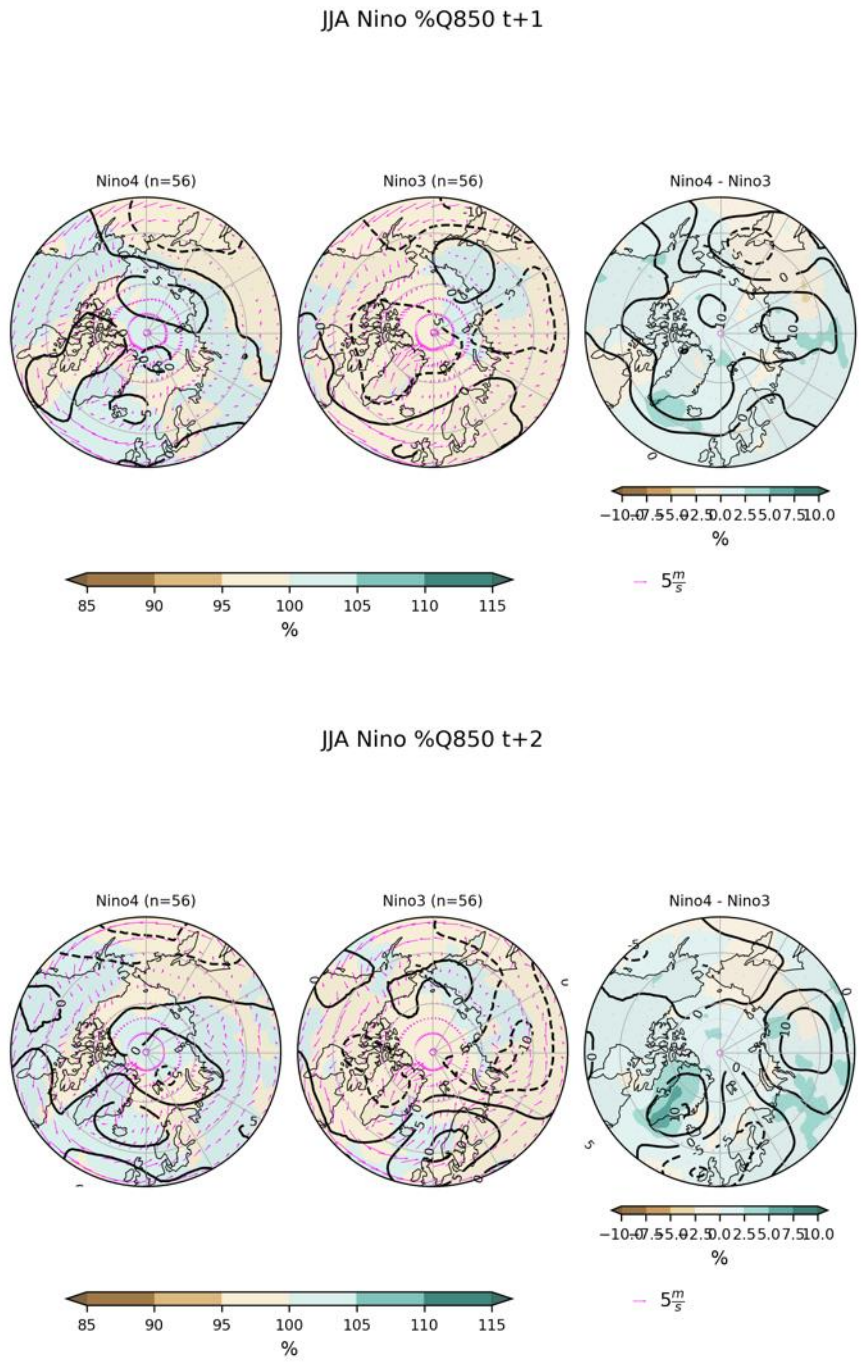

Figure A10. Similar to Figure A9, but for Niño conditions.